

# Andreev bound states in semiconducting double nanowires

**Inauguraldissertation**

zur  
Erlangung der Würde eines Doktors der Philosophie  
vorgelegt der  
Philosophisch-Naturwissenschaftlichen Fakultät  
der Universität Basel

von

**Olivier Faist**

Basel, 2024

Genehmigt von der Philosophisch-Naturwissenschaftlichen Fakultät  
auf Antrag von

Prof. Dr. Christian Schönenberger  
*Erstbetreuer*

Prof. Dr. Christoph Bruder  
*Zweitbetreuer*

Prof. Dr. Kasper Grove-Rasmussen  
*Externer Experte*

Prof. Dr. Szabolcs Csonka  
*Externer Experte*

Basel, den 13. Dezember 2022

Prof. Dr. Marcel Mayor  
Dekan

for Kostas and André



# Contents

<b>1</b>	<b>Introduction</b>	<b>1</b>
<b>2</b>	<b>Theoretical background</b>	<b>5</b>
2.1	Transport in low-dimensional semiconductors . . . . .	6
2.1.1	Semiconductors . . . . .	6
2.1.2	Transport in a 1D conductor . . . . .	6
2.1.3	Ballistic transport . . . . .	7
2.1.4	Quantum dots . . . . .	7
2.1.5	Coupled quantum dots in double semiconducting nanowires . . . . .	9
2.2	Superconductivity . . . . .	12
2.2.1	Quasiparticles . . . . .	12
2.3	Transport in semiconductor-superconductor hybrids . . . . .	13
2.3.1	Andreev reflection and transport in an N-S device . . . . .	14
2.3.2	A quantum dot coupled to a superconductor . . . . .	15
2.3.3	Andreev bound states . . . . .	15
2.4	Josephson effect . . . . .	16
2.4.1	Multiple Andreev reflections . . . . .	19
<b>3</b>	<b>Experimental Methods and devices fabricaion</b>	<b>21</b>
3.1	Introduction . . . . .	22
3.2	InAs semiconductor nanowires . . . . .	22
3.2.1	Nanowire growth . . . . .	23
3.2.2	Double nanowire growth . . . . .	23
3.2.3	Electronic properties of InAs Nanowires . . . . .	25
3.3	The fabrication workflow . . . . .	25
3.3.1	Base structures . . . . .	25
3.3.2	Wire deposition . . . . .	27
3.3.3	Readout of the nanowire position and design of the devices . . . . .	27
3.3.4	Nanowire contacting . . . . .	27
3.3.5	Required accuracy . . . . .	28
3.3.6	Bonding and building in the Cryostat . . . . .	28
3.3.7	Process optimizations . . . . .	29
3.4	Measuring . . . . .	29
3.4.1	Dilution refrigerator . . . . .	29
3.4.2	Electric setup . . . . .	30

<b>4</b>	<b>Andreev bound states in a double nanowire NS Junction</b>	<b>33</b>
4.1	Introduction . . . . .	34
4.2	Fabrication and geometry . . . . .	34
4.3	Transport in the normal state . . . . .	36
4.3.1	Sample characterisation at $T = 4\text{K}$ . . . . .	37
4.3.2	Double wire transport with contacts in the normal state . . . . .	38
4.4	Spectroscopy of the superconducting junction . . . . .	40
4.4.1	Superconducting gap . . . . .	41
4.4.2	Conductance in the superconducting state . . . . .	42
4.5	Single wire Andreev bound states . . . . .	43
4.5.1	Magnetic field dependence . . . . .	43
4.6	Spurious dots . . . . .	45
4.7	Overlapping single-wire Andreev bound states . . . . .	46
4.8	Gap size artefact . . . . .	48
4.9	Coherently coupled dot Andreev bound states in an N-S double junction . . . . .	51
4.10	Discussion . . . . .	52
<b>5</b>	<b>Double nanowire Josephson junction</b>	<b>53</b>
5.1	Device and characterisations . . . . .	54
5.1.1	Transport in the normal state . . . . .	54
5.2	A double InAs nanowire Josephson junction . . . . .	55
5.2.1	Magnetic field dependence . . . . .	56
5.2.2	Comparing conductance in the N and S states . . . . .	58
5.3	Supercurrents . . . . .	58
5.3.1	Discussion . . . . .	59
<b>6</b>	<b>Quasiparticle trapping in a S-N-S junction</b>	<b>61</b>
6.1	Introduction . . . . .	62
6.2	Device . . . . .	62
6.3	Normal state characterization . . . . .	63
6.4	Josephson physics . . . . .	64
6.5	Andreev bound states in the junction . . . . .	66
6.6	Mapping the critical current . . . . .	68
6.7	Quasiparticle trapping . . . . .	69
6.8	Discussion . . . . .	75
<b>7</b>	<b>Conclusion</b>	<b>77</b>
	<b>Bibliography</b>	<b>81</b>
	<b>Curriculum Vitae</b>	<b>99</b>

**Acknowledgements**

**101**



# 1 Introduction

---

*Do you wish me a good morning, or mean that it is a good morning  
whether I want it or not; or that you feel good this morning or that  
it is a morning to be good on?*

- J.R.R. Tolkien

The science of physics has always consisted in a symbiosis between theory and experiment, feeding off each other to improve our understanding of phenomena describing the world we live in. Sometimes a new effect, be it intentionally discovered or the result of a happy accident, will spur on theoretical work scrambling to provide an understanding of the underlying physics. On the other hand, occasionally theoretical understanding of a phenomenon will make a prediction, which will drive improved or novel experiments to be designed until being able to confirm or deny the prediction, thus validating the theoretical model in the former case or proving the limits of our understanding in the latter. The Higgs boson is one of the best-known examples of such an experimental validation of a long-formulated prediction.

In the field of transport — the study of electrical currents and their carriers — the discovery of new phenomena and the development of new technologies is always dictated by advances in material quality and processing capabilities.

Initially focused on the study of bulk materials, the advent of semiconductors spurred a revolution in the study of carrier transport: a new level of control over experiments could be achieved through doping and gating, which modified the device's carrier density and therefore its electric properties.

These newfound technologies enabled the fabrication of novel devices, including the transistor in 1947 and the MOSFET in 1958. The latter was a crucial ingredient for the development of integrated circuits which would end up changing the world.

The ensuing race for faster and smaller circuits, predicted by Gordon Moore's visionary paper in 1965 [1], leveraged drastic improvements in fabrication technologies. Such technologies include first optical and later electron-beam lithography, the latter enabling the writing of structures at the nanoscale.

This miniaturisation led to quantum effects being observable in transport experiments. Selectively depleting a high-mobility 2-dimensional electron gas to form a narrow constriction perpendicular to the flow of current effectively forces electron transport through a single channel. The quantum nature of ballistic transport, predicted by Landauer in 1957, was demonstrated in this way in 1988 [2, 3].

Arranging two such quantum point contacts in series allows for the confining of an electron in all three dimensions, creating an “artificial atom”, also called *quantum dot*. Electrons can be injected onto the dot or extracted from the dot via electrically controlled gates [4, 5].

All the work described so far employs a *top-down* approach: bulk material is etched, doped or gated in the fabrication and measurement processes in order to achieve the desired confinement. An alternative is the so-called *bottom-up* approach, where a nanostructure is synthesised already presenting the sought confinement properties.

Semiconductor nanowires, monocrystalline structures, a few microns long and tens of nanometers wide, are typically grown in a bottom-up manner. These nanowires are a technology with a wide range of applications [6] due to their transport characteristics and wide range of possible materials which enable the fabrication of various device types. Examples include field effect transistors with high mobility using silicium nanowires [7], or ZnO nanowires for light emitting diodes [8], silicium top-down fabricated nanowires for solar cells [9] and InAs nanowires used in gas [10] or infrared [11] sensors.

Nanowires are foremost a prime platform for a host of transport experiments, InAs being especially interesting [12] owing to its high spin-orbit coupling [13], low effective mass, and growth techniques yielding high mobility devices that are almost devoid of impurities [14, 15].

While the miniaturization of elementary logic gates revolutionized the development of applications relying on classical computing, the seeds of a radically different type of computer were being sown. Feynman suggested in 1982 that the peculiar laws of quantum mechanics could be leveraged for simulating the properties of quantum systems [16], thereby proposing the idea of a quantum computer. A major breakthrough was achieved by Peter Shor in 1994: he discovered an efficient quantum algorithm for factoring large numbers, a problem widely believed to be hard on a classical computer [17, 18]. A rapid growth of the emergent field of quantum computing followed, further fueled by advances in the theory of quantum computing and information and by early experiments demonstrating the control of individual qubits [18]. More recently, an increasing cohort of major industrial players and start-ups are leading the effort [19], further supported by massive public initiatives [20, 21], to build a future fault-tolerant quantum computer.

The development of a quantum computer powerful enough to solve meaningful tasks (such as using Shor’s algorithm to factor large numbers [17, 18]) faces

---

the formidable challenge of engineering many qubits that have exceptionally low levels of noise. A promising approach to reduce the noise in a computation is to use *quantum error correction* to protect the information being processed from the noise that the physical qubits are inevitably exposed to [18, 22, 23]. An alternative approach is to design quantum hardware that natively stores quantum information in a protected form — effectively implementing quantum error correction at the hardware level.

A scheme implementing this hardware level protection was proposed by Kitaev in 2000 [24, 25], whereby braiding anyons — i.e. simply moving them around each other on a topological path — is used as a building block for quantum operations. Their nature is fault-tolerant, being protected from the environment by a topological gap. Furthermore, Kitaev suggested that semiconductor nanowires proximitized by a superconductor with a p-wave symmetry could host unpaired Majorana quasiparticles. These particles, first theorized by their namesake Ettore Majorana [26], are identical to their own anti-particle and are thus massless, chargeless and spinless.

InAs nanowires are a notable candidate for hosting these novel topological states. Alicea [27] theorised that proximitizing a nanowire with strong spin-orbit interaction under the influence of a magnetic field would generate the p-wave superconductivity required for the hosting of Majoranas. The prospect of a naturally fault-tolerant quantum computer spurred a large research effort aimed at realizing these proposals, finally yielding the observation of a 0-bias peak attributed to a Majorana bound state [28]. Two important properties that are intrinsic to a Majorana mode remained elusive: the quantisation to  $e^2/h$  of the 0-bias anomaly and demonstration of the pickup of a phase under a braiding operation of two Majorana modes.

Building on the original observation of the Majorana mode, a further theoretical proposal [29] suggests a scheme in which a double nanowire coupled to a superconductor could host parafermions. The latter, which can be intuitively seen as fractional Majoranas, offers the advantage of a wider universal set of operations when braided. In order for these parafermions to arise, the proposal determined a set of conditions, most of which directly translate into technological challenges. These requirements include different spin-orbit coupling in the individual wires, individual contacting of the wires, and a high-quality superconductor-semiconductor interface leading to a delocalisation of the wavefunction, all of which require beyond state of the art nanoscale device fabrication.

At the same time, doubts about the nature of the 0-bias anomaly attributed to a Majorana mode grew in the community. Only two years after the original Majorana finding, a report attributed multiple peaks at 0 bias to Andreev bound states, thus providing an alternate topologically trivial explanation for the observed phenomenology [30]. Unfortunately, no significant progress was achieved towards proving the missing properties, in particular the missing

1

quantisation of the 0 bias peak. Indeed, a work from the Leo Kouwenhoven reporting the quantization of the 0-bias anomaly was retracted [31]. Similarly, a report from the Marcus group of a 0-bias anomaly in a full-shell nanowire, attributing the topological phase transition to a flux quanta of field through the nanowire shell, [32] is now prefaced by an editorial expression of concern [33]. In another experiment, 0-bias states were shown to be present in a wide parameter range, making their topological nature unlikely [34].

The unravelling of the Majorana interpretation underlines the need for a better understanding of the physical phenomena at play, be it spin-orbit interaction, the microscopic consequences of the proximitisation of a semiconductor nanowire by a superconductor, or the phenomenology of Andreev bound states. Those issues are at the core of the work presented here.

In this thesis, we thus laid the focus on improving the fabrication process in order to reliably individually contacted the wires, as well as understanding the individual phenomena involved in generating the conditions required for the observation of the Majorana modes. We first present a summary presentation of the key theoretical concepts used in this thesis, followed by a chapter where the experimental techniques required for the fabrication and measurement of our devices are introduced. Then we present the core of this work, consisting of the results of three series of experiments. In the first, we design a double wire N-S junction, enabling straightforward access to the properties of our device which allows us to demonstrate the excellent quality of the wire to superconductor interface. In the second experimental chapter, we focus on the Josephson effect, analysing a double nanowire Josephson junction, characterising its  $R_N I_C$  product. In the last chapter we design and report on a quasiparticle trap, which dramatically enhances the critical current of a Josephson junction. We tentatively attribute this effect to the superconducting shell of the wire transitioning to a mixed state, trapping quasiparticles in normal regions close to the Josephson junction.

## 2 Theoretical background

---

*Sans technique, un don n'est rien qu'une sale manie.*

- Georges Brassens

In this chapter, we provide the reader with an overview of the relevant theoretical concepts required for understanding our experimental results. We focus on providing an intuitive understanding of the matter when possible, and refer to references [35] and [36] for an in-depth, exhaustive presentation of the topics at hand.

## 2.1 Transport in low-dimensional semiconductors

### 2.1.1 Semiconductors

Unlike metals, where a sea of free-moving electrons enable transport of current, or insulators, where a lack of unbound electrons forbids the flow of current, semi-conductors have transport properties that can be controlled by doping and gating.

In a crystal where the atoms are arranged in a periodic lattice, one solves the Schrödinger equation using the *Ansatz* of Bloch. It expresses the fact that solutions can be written as the product of a function that possesses the lattice periodicity and a plane wave. The solution exhibits dispersion relation between the electron's energy and its crystal momentum, the band structure, which is the basis for the computation of the carrier transport. The latter may be either excess electrons or *holes*, which are missing electrons in an otherwise fully occupied band. These are in fact quasi-particles, a collective motion of the crystal lattice electron and atoms which behave like a single particle. Thus, they are also described by an effective mass which differs from the mass of an electron in vacuum.

#### Gating and doping

At temperatures  $kT < E_{\text{gap}}$ , semiconductors are isolating, since the Fermi distribution of electrons in energy requires the valence band to be full and the conductance band to be empty, leaving no free charge carriers to transport current. There are two main mechanisms for tuning the charge carrier density in a semiconductor: gating and doping. Doping refers to artificially introducing charge carriers into a semiconductor, for instance by introducing atoms in the lattice that have either an additional electron or an electron deficit. These additional charge carriers result in quasi-electron collective excitations, which we call electrons for the sake of clarity, and which obey the dispersion relation of the band they occupy and can carry current. The semiconductor thus becomes conducting. Alternatively, one can capacitively gate the semiconductor by bringing a conductor with a potential difference in close proximity. The ensuing electrostatic charges become available charge carriers able to transport current. Controlling the semiconductor's ability to transport current in this way is the working principle of a field-effect transistor; it is also the principle used for tuning charge carrier density throughout the experiments presented in this thesis.

### 2.1.2 Transport in a 1D conductor

In quasi-1D conductors, the width  $d$  of the conductance channel is narrow enough such that the modes lateral to the transport direction are quantized,

i.e. the Fermi wavelength satisfies  $\lambda_F \sim d$ . This can be achieved on multiple platforms, like carbon nanotubes [37], gated 2D electron gases [3], or semiconductor nanowires, which will be described in more detail in the next chapter.

### 2.1.3 Ballistic transport

Laterally confined charge carriers are distributed on one-dimensional modes with energy levels corresponding to the lateral confinement energy. In a semiconductor 1D channel, these modes can be populated by tuning the chemical potential, either by capacitive gating or chemical doping. If the mean free path  $\xi$  of the charge carriers is shorter than the junction, then the charge carrier will undergo multiple scattering events before reaching the other electrode and the transport is diffusive. If on the other hand, the channel is free of defects, such that  $l > \xi$ , the electrons can ballistically travel the length of the junction [2, 3, 38]. The conductance as a function of voltage then takes the form  $G_{\text{ball}} = 2e^2/h \cdot N$ , with  $n$  the amount of channels carrying electrons. The factor of 2 comes from accounting for the spin degree of freedom of the charge carrier.

### 2.1.4 Quantum dots

Also referred to as “artificial atoms”, quantum dots (QD) are quasi-0D traps where charge carriers are confined in all three dimensions in a region small enough to allow only few charge carriers, effectively quantizing the trapped particles’ energy spectrum [42]. A quantum dot can be engineered in a 1D conductor by additionally confining the charge carriers along the direction of the conductor. Such a confinement can be achieved by two nearby short regions of the 1D channel with a higher chemical potential, creating sequential potential barriers. Owing to its small scale, the capacitance of the dot is small; adding a charge carrier thus comes at a large energy cost [43]. This *Coulomb blockade* effect is a defining effect of a quantum dot, the latter having been engineered in graphene [44], in 2 dimensional electron gases [45], in carbon nanotubes [46] and in semiconducting nanowires [47].

The energy level spacing of a quantum dot is given by two energies: the confinement energy and the Coulomb repulsion energy [40]. The confinement energy for charge carriers obeying a quadratic dispersion relation, similarly to the “particle in a box” model, relates to the size of the dot  $L$  following a  $\delta E \propto 1/L^2$  relation. [48]. The energy spacing between two dot levels is given by [39, 40]:

$$E_{\text{add}} = \mu(N + 1) - \mu(N) = \frac{e^2}{C} + \delta E , \quad (2.1)$$

with the charging energy  $E_C = \frac{e^2}{C}$  and quantum confinement energy  $\delta E$ . Spin degeneracy and Pauli’s exclusion principle also influence the level filling of the

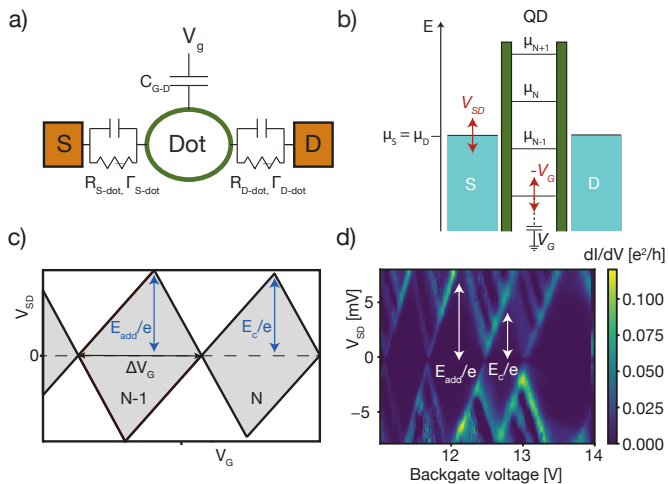


**Figure 2.1 Quantum dot.** a) Simple electric model b) Energy representation of a) c)  $dI/dV$  as a function of bias and plunger gate, expected Coulomb diamonds sketched. d) Example of Coulomb diamonds measured in an InAs nanowire. Schematics adapted from references [39, 40, 41]

dot [49].

We assume negligible electron-electron interaction and constant quantum dot self capacitance, a setting also referred to as the constant interaction model [42, 49]. Fig. 2.1 a) shows a quantum dot in a standard transport setting, connected to two electrodes, source S and drain D, and capacitively coupled to a plunger gate  $V_g$ . Applying a voltage bias  $V_{BG}$  between source and drain and a plunger gate voltage  $V_G$  allows for the probing of the discrete energy levels: the effect in energy is sketched in Fig. 2.1 b).  $V_{SD}$  changes the chemical potential of the source and drain contacts by  $\Delta\mu_S = e \times V_{SD}$ , assuming the drain is grounded, whereas the plunger gate changes the dot chemical potential through an imperfect capacitive coupling  $\Delta\mu_{\text{dot level}} = \alpha V_G$ , where  $\alpha [eV/\Delta V]$  is the *lever arm* [50]. The conductance of the dot peaks when the levels are on resonance, i.e.  $\mu_D = \mu_N = \mu_S$ , and conductance is suppressed otherwise, corresponding to the aforementioned *Coulomb blockade*. This effect results in the *Coulomb diamond* pattern sketched in Fig. 2.1 c), with an experimental example from our data in Fig. 2.1 d). This intuitive picture of the Coulomb diamonds, in which tunneling is either on or off, needs to be refined to quantify the rates at which electrons can tunnel to or from the dot. We define two tunnelling rates  $\Gamma_S, \Gamma_D$  to the source and drain contacts. Consequently, the charge carrier has a finite lifetime, and, per Heisenberg, is broadened in energy. At low temperature  $kT \ll \Gamma = \Gamma_S + \Gamma_D$ , and for weak coupling strengths  $\Gamma \ll \delta S, E_C$ , which we call the *dot regime*, the conductance of a singleresonance is given by [51]:

$$G_N(\epsilon) = \frac{2e^2}{h} \frac{\Gamma_S \Gamma_D}{\epsilon^2 + (\Gamma_S + \Gamma_D)^2/4}. \quad (2.2)$$

This conductance gets broadened at higher temperature, changing the lineshape of the resonance [52, 53]. This relation allows us to extract information on *both*  $\Gamma_S$  and  $\Gamma_D$  from the lineshape. Experimentally extracting exact values for  $\Gamma_S, \Gamma_D$  requires determining the lever arm  $\epsilon = \alpha V_{BG}$ , which yields the required relation between an applied gate voltage and the variation in chemical potential. However the ratio  $\Gamma_S/\Gamma_D$  can be determined by the fitting a resonance lineshape without exact knowledge of the energy scale [49, 51]. In any two-terminal transport measurement there remains an ambiguity in determining  $\Gamma_S$  and  $\Gamma_D$ , associated with interchanging the values of  $\Gamma_S$  and  $\Gamma_D$ .

### 2.1.5 Coupled quantum dots in double semiconducting nanowires

Nanowire pairs are at the core of the experiments reported in this thesis. Although we also observe evidence of ballistic transport, when the plunger gates are set at low voltage values, depleting the wire segments and the coupling of the source and drain contacts, we observe the formation of quantum dots

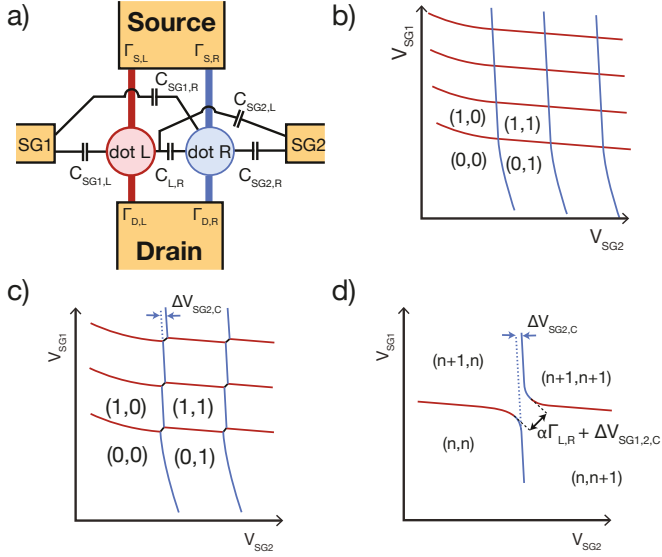


**Figure 2.2** Coupled dots in parallel double nanowires **a)** Simple model. Capacitive couplings to source and drain, as well as other elements omitted for clarity. **b)** Conductance as a function of plunger sidegates in the dot regime  $\Gamma_{S/D,L/R} \ll E_{add}$ , and  $C_{L,R} = 0$  occupation numbers of the dots are provided in (right,left) form. **c)** Same as b) for a finite  $C_{L,R}$  **d)** Detail of the crossing between two resonances for a finite coherent coupling  $\Gamma_{L,R}$ .

in parallel nanowire segments. A brief overview of the consequences of two quantum dots in close proximity will thus be provided here, focussing on the consequence of capacitive coupling and hybridisation of the dot states.

If the dots are electrically isolated, the electrostatic field emanating from the charge state in the first dot acts in a similar way to the plunger gates, changing the chemical potential of the neighbouring dot. This is the working principle employed in charge sensing schemes, where transport measurements of a dot is employed to non-invasively measure the occupation of a nearby capacitatively coupled quantum dot [54, 55, 56]. If they are not electrically isolated, the wave function of the charge states of the dots might overlap. Electrons can then tunnel from one dot to the other, keeping coherence and leading to a hybridisation of the charge states [57], an effect which we attribute to anti-crossings of the dot resonances in section 4.9.

The consequences of this coupling manifests itself in transport measurements. The expected differential conductance as a function of plunger sidegates for different scenarios is plotted in fig. 2.2 b)-d), with an overview of the relevant capacitances provided in a). It is assumed that both wire segments are in the quantum dot regime, i.e.  $\Gamma_{S/D,L/R} \ll E_{\text{add}}$ , the energy spacing between two dot states. In the simplest case, when  $C_{L,R} = 0$ , we see two sets of dot resonances with different slopes. In the ideal case of no capacitive cross-coupling of the sidegates  $C_{SG2,L} = C_{SG1,R} = 0$ , the lines would be perfectly vertical and horizontal, the wire segments being exclusively gated by the corresponding sidegate. In the presence of this cross-capacitance, the resonances take a slope related to the cross-capacitance ratio,  $-C_{SG1,R}/C_{SG2,R}$  for the blue case, which is also equivalent to the ratio of the lever arms of the dot to the 2 sidegates. The upwards bending of resonances of the right dot (blue) when the left dot (red) is depleted is a consequence of the absence of screening of sidegate 1 by the wavefunction of the left dot's charge state. The suppressed screening thus increases  $C_{SG1,R}$  and changes the slope, an effect which is observed in the data from chapter 5. In c), the capacitive cross coupling is turned on, which has the effect of electrons in one wire slightly gating the other, resulting in a shift  $\Delta V = eC_{L,R}$ , and a general honeycomb pattern. In d) the dots charge states are coherently coupled, resulting in the crossing of the resonances becoming a hybridised state, with a gradual transition between the additional +1 electron's wavefunction being located in the left to the right dot when transitioning from the  $(n+1,n)$  to the  $(n,n+1)$  region. The differential conductance of both wires is sketched as follows: if the wires are individually contacted the sketches separate in the red and blue parts; both are accordingly measured in the individual junctions.

## 2.2 Superconductivity

We now introduce the elementary principles of superconductivity, which plays an essential role in this work. We provide an overview of the relevant concepts, and refer the reader to references [36, 58, 49, 41] for a in-depth presentation of the theory of superconductivity.

It was first discovered in 1911 that some metals, including mercury, aluminum, niobium and lead, exhibit remarkable properties when cooled down below a critical temperature  $T_C$  [59]. The most distinctive property of a superconductor is a resistivity so small that it cannot be measured. Further properties include the Meissner effect [60], wherein a magnetic field is expelled from the superconductor and cannot penetrate a superconductor beyond a skin depth  $\delta$ . The current in the superconductor required by Maxwell's law to repulse the field lines also implies the existence of a critical field  $B_C$ , above which the energetic cost of this current is too large leading to the superconductivity breaking down. It was also found that a superconductor has a peculiar specific heat  $\sim \exp(\frac{T_0}{T})$ . These phenomenological characteristics of this macroscopic phase of matter were first given a microscopic explanation by Bardeen, Cooper and Schrieffer [61], nowadays known as the *BCS theory* of superconductivity. This theory predicts the pairing up of electrons via phonon-mediated interactions when the difference of energy  $\Delta\varepsilon$  between the electrons satisfies  $\Delta\varepsilon < \hbar\omega$ , even though electrons repulse each other by Coulomb interaction. This phonon-mediated attraction can be intuitively understood as follows: a first electron slightly displaces ion lattice elements by Coulomb force, thus creating a shadow positive charge that stays in place long enough for a second electron to be attracted by it. Electrons being fermions and obeying the exclusion principle leads them to form Cooper pairs — pairs of electrons with opposite spin. Cooper pairs are composite bosons: they obey bosonic statistics allowing an arbitrary number of them to condense in a lower-energy collective ground state  $\psi(r) = \sqrt{N(r)}e^{i\Phi(r)}$ , with  $N(r)$  the Cooper pair density and  $\Phi(r)$  a collective macroscopic phase [36].

### 2.2.1 Quasiparticles

Excitations of the superconductor, which we refer to as quasiparticles, require the breaking of a Cooper pair. They are both of hole and electron nature, thus this breaking requires an energy of twice the energy gap  $\Delta$ . This behaviour contrasts with the analogous process in a semiconductor, where the gap energy suffices to create an electron-like quasiparticle.

The BCS model thus predicts a gap  $\Delta$  in the energy spectrum where no quasiparticles can be found. Electron-like quasiparticles (respectively hole-like quasiparticles) can be found above (respectively below) this gap, and they obey the dispersion relation  $E(k) = \sqrt{\epsilon(k)^2 + \Delta^2}$ . The superconducting transition

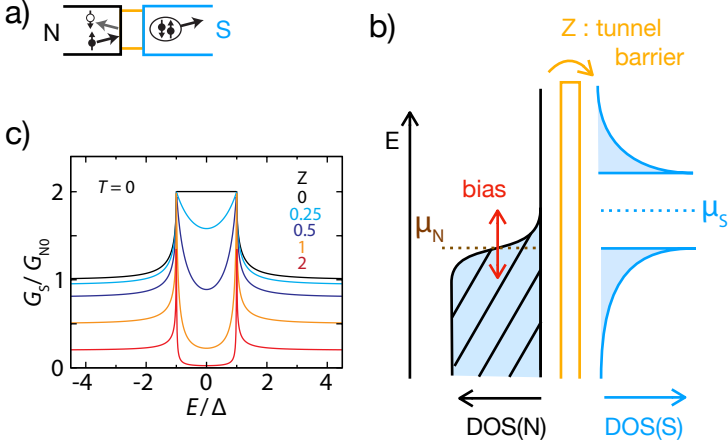


**Figure 2.3** a) Andreev reflection on an interface. b) Process visualized in energy. c) Normalised conductance as a function of  $\epsilon$  predicted by the BTK model for various  $Z$  values, adapted from [49]

conserves the number of particles, allowing the derivation a density of states under the condition  $D_N(\epsilon)d\epsilon = D_S(E)dE$ ,

$$\text{DOS}(E) = \frac{d\epsilon}{dE} = \begin{cases} 0 & (E < \Delta) \\ D_N(\epsilon) \frac{E}{\sqrt{E^2 + \Delta^2}} & (E > \Delta) \end{cases} \quad (2.3)$$

The density of states in the normal phase  $D_N(\epsilon)$  can usually be approximated as being constant in a short range around the Fermi energy in most transport experiments. In this case, the density of states  $\text{DOS}(E) \rightarrow D_N$  for large energies while the density of states diverges for energies  $|E| \rightarrow \Delta$  [36].

## 2.3 Transport in semiconductor-superconductor hybrids

We now consider a system in which a superconductor and a semiconductor are connected by a tunnel barrier. We discuss the transport mechanisms enabling current to flow from the semiconductor, where quasi-electrons are bound to the band structure, to the superconductor, where Cooper pairs of electrons in a macroscopic wavefunction enable the flow of a dissipationless current.

### 2.3.1 Andreev reflection and transport in an N-S device

An electron with energy  $\varepsilon = E_e - E_F < \Delta$  cannot inelastically enter the superconductor, since there is an absence of a corresponding state in the superconducting gap. An electron at that energy can nevertheless interact with the superconductor through a second-order process (Fig. 2.3 a): the electron is annihilated, a hole with opposite energy  $E_h - E_F = E_F - E_e$  and momentum  $k_h = -k_e$  is created in the normal lead, and a Cooper pair with the same momentum is created in the superconductor. This process, known as an Andreev reflection, conserves charge, energy and momentum [62].

The retro-reflected hole in an Andreev reflection retraces the path of the incoming electron, and accumulates a phase  $\phi_{e-h}$  given by momentum conservation  $k_e - k_h = k_{e-h} = 2\varepsilon/\hbar v_F$ ,  $v_F$  being the Fermi velocity of the initial electron. The electron and hole remain coherent over a distance  $\xi$ , called the *phase coherence length*, that satisfies the condition  $k_{e-h} \cdot \xi < \pi$ . As a result, we have

$$\xi = \frac{\pi\hbar}{2} \cdot \frac{v_F}{\Delta}. \quad (2.4)$$

However, this expression does not account for the scattering of the electron and hole and therefore holds in the limit of a ballistic junction. In the case of a diffusive junction, the relation becomes:

$$\xi_{\text{diffusive}} = \sqrt{\xi_{\text{ballistic}} \times l_e} \quad (2.5)$$

where  $l_e$  is the mean free path of the charge carriers in the diffusive junction. Thus, in order to optimize the phase coherence length, a material with low  $v_F/\Delta$  is desirable [36].

The transport characteristics of a normal-superconductor junction is theoretically described by the Blonder, Tinkham and Klapwijk (BTK) model [63]. The tunnel barrier is modeled by a repulsive Dirac potential  $H\delta(x)$ , whose strength is characterised by a dimensionless quantity  $Z$  satisfying  $Z = H/v_F$ . The expected conductance  $G(E)$  is derived by applying the correct boundary conditions to the Bogoliubov-de-Gennes equations (Fig. 2.3 c). In the  $Z = 0$  case, which corresponds to a perfectly transparent junction, we observe a doubling of the conductance. This doubling can be intuitively understood as the perfect Andreev reflection of every electron in a Cooper pair, carrying double the current. In the other extreme of an interface with low transparency, the transport conductance resembles the density of state of the superconductor. This can be understood by considering the conductance of a single mode with transmission probability  $T$ .

In the normal case, the Landauer expression for a normal interface is  $G_N = 2e^2T/h$ . In contrast, the conductance is given in the superconducting state

by:

$$G_{\text{N-S}} = \frac{4e^2}{h} \frac{T^2}{(2-T)^2}. \quad (2.6)$$

The  $\sim T^2$  dependence of Andreev reflection conductance compared to the  $\sim T$  dependence of the direct tunnelling reflects the fact that when the transparency is low, direct electron tunneling dominates transport and the resulting conductance is effectively a tunnel spectroscopy measurement of the density of states of the superconductor.

### 2.3.2 A quantum dot coupled to a superconductor

Coupling a quantum dot instead of a simple tunnel barrier to a superconductor, forming a N-Dot-S device leads to a more elaborate junction. Instead of the continuum of available states offered by a normal state lead, the discrete energy levels of the dot further constrain available transport mechanisms.

In a groundbreaking work [51], C. Beenakker predicted transport at zero source drain bias in multiple configuration starting from the Landauer and BTK predictions. In a quantum point contact, the doubling of the conductance known from the BTK theory applies to plateaus, the step between which occur at slightly higher energy values than twice the classical conductance. In quantum dots, the expression for N-Dot-S conductance is given by:

$$G_{\text{NS}}(\varepsilon) = \frac{4e^2}{h} \left( \frac{2\Gamma_S\Gamma_D}{4\varepsilon^2 + \Gamma_S^2 + \Gamma_D^2} \right)^2, \quad (2.7)$$

recalling the expression from equation 2.2 for the normal state:

$$G_{\text{N}}(\varepsilon) = \frac{2e^2}{h} \frac{\Gamma_S\Gamma_D}{\varepsilon^2 + (\Gamma_S + \Gamma_D)^2/4}$$

We note the  $G_{\text{NS}}(\varepsilon) \propto 1/\varepsilon^4$  contrasting to the  $G_{\text{N}}(\varepsilon) \propto 1/\varepsilon^2$ , which is confirmed by a sharpening of features in the superconducting state observed in the chapters 4 - 6.

### 2.3.3 Andreev bound states

The consequences of coupling a superconductor to a quantum dot go further than changing the lineshape of the 0-bias conductance. If we consider a quantum dot strongly coupled to a superconductor, such that  $\Gamma_N \ll \Gamma_S \sim \Delta < \delta E < E_C$ , the energy of the quantum dot states are strongly affected by the coupling. Indeed the interplay between Andreev reflections and dot states yield a steady-state solution, and represent one of the possible manifestations of an *Andreev bound state* [64]. These states are at the core of the proposed Andreev qubit [65, 66], and have been the focus of a host of theoretical [67,

68, 69] and experimental [70, 71, 64, 72, 73, 74, 75] reports [49]. These bound states can be directly observed in tunnel transport spectroscopy by coupling a metal through a strong tunnel barrier[71, 64]. Recently, Andreev bound states hosted on coupled quantum dots, forming an Andreev molecule, have been reported [76, 77, 78]. Following references [68, 49], we will now present these states in more detail.

Considering the system in the second quantisation, it can be described by a Hamiltonian  $H = H_{\text{QD}} + H_S + H_T$ , where:

$$H_{\text{QD}} = \varepsilon_0(n_\uparrow + n_\downarrow) + U n_\uparrow n_\downarrow \quad (2.8)$$

is, ignoring spin, the energy of a quantum dot with electron occupation numbers  $n_{\uparrow/\downarrow} = a^\dagger a$ , and  $U$  the Coulomb interaction. The  $H_S$  and  $H_T$  Hamiltonians are issued of a mean field treatment of the BCS theory and account for the coupling to the superconducting and normal leads:

$$H_S = \sum_{k,\sigma} \xi_k c_{k,\sigma}^\dagger c_{k,\sigma} - \sum_k (\Delta c_{k,\uparrow}^\dagger c_{-k,\downarrow}^\dagger + \text{h.c.}) \quad (2.9)$$

$$H_T = \sum_{k,\sigma} (V_k c_{k,\sigma}^\dagger a_\sigma + \text{h.c.}) \quad (2.10)$$

In these relations  $\Delta$  is the superconducting order parameter,  $c_{k,\sigma}^\dagger$  is the creation operator of an electron of wavevector  $k$  and spin  $\sigma$  at an energy  $\xi_k$  above the chemical energy and  $a, a^\dagger$  are the dot state electron. The coupling strength is given by  $\Gamma_S = 2\pi|V|^2 D_N(0)$ , with  $D_N$  being the normal density of states, assumed to be constant around the Fermi energy; the coupling  $V_k \sim V$  is equally assumed to be constant[79, 80, 81, 79, 30].

In the absence of a full analytical solution, we will instead present qualitative results from numerical approximations using renormalisation group calculations [68, 49], shown in fig. 2.4. The subgap Andreev bound states  $\zeta_\pm$  stay near the gap  $\Delta$  unless the normal state dot is near resonance. For a junction in the weak dot regime, the spin parity of the electrons in quantum dot gives the parity of the ground state of the system, which switches when an additional dot state is occupied, where Andreev bound states cross 0 bias. If the dot is strongly coupled to the superconductor, i.e.  $\Gamma_S/U$  increases beyond a given threshold, superconducting pairing is stronger than Coulomb interaction and the dot ground state is permanently a singlet.

## 2.4 Josephson effect

We now consider two superconductors connected by a *weak link* of normal conducting material, in our case a nanowire segment, forming a S-N-S junction. The two superconductors S1 and S2 have a macroscopic phase  $\varphi_1$  and  $\varphi_2$ .

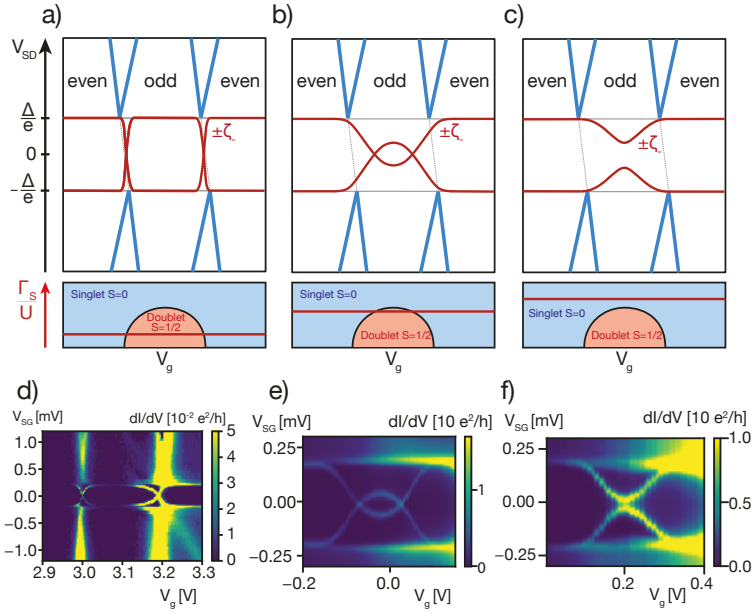


**Figure 2.4 Andreev bound states a-c)** Qualitative results from RNG calculations for increasing coupling to the superconductor. The conductance vs gate and bias is sketched in the top panels. The Andreev bound states are shown in red, the normal state Coulomb resonances in blue. In the bottom panels, the quantum dot ground state is sketched for varying backgate. Adapted from [49, 82]. **d-f)** Data from the experiments reported in chapter 4 fitting the qualitative predictions.

Andreev reflections on both interfaces transport current by the simultaneous creation of an electron and a hole with opposite momenta, which are annihilated at the opposing interface, thereby transferring a charge of  $2e$  through the junction. This process, called the supercurrent, conserves charge and energy and is phase-coherent.

The supercurrent was first predicted by Josephson for an S-insulator-S interface [83] but found to hold in the more general case of metallic or semiconducting weak links [84]. Josephson realized that the continuity of the phase of the macroscopic wavefunction of the superconductor over the weak link results in a Cooper pair current that depends on the phase difference between the superconductors. Surprisingly, this current flows even in the absence of a driving external electromagnetic field. This effect can be summarized mathematically by the Josephson relations:

$$\begin{aligned} I(t) &= I_c \sin(\varphi(t)) \\ \frac{\partial \varphi}{\partial t} &= \frac{2eV(t)}{\hbar}, \end{aligned} \quad (2.11)$$

introducing the *critical current*  $I_C$  as the maximal value of the supercurrent as well as the phase difference  $\varphi = \varphi_2 - \varphi_1$  between the superconductors. The *first relation* expresses the current through the weak link as a function of the relative phase, whereas the *second relation* implies an oscillation of phase difference under the application of a fixed voltage bias.

A number of experiments in this thesis are performed on nanowires with two superconducting contacts. Additionally, these S-Nanowire-S junctions are sufficiently short that the phase coherence condition is satisfied, as evidenced by observation of a Josephson supercurrent. In order to characterize the quality of this junction, we measure the critical current  $I_C$  and compare it with the theoretical value predicted by Ambegaokar and Baratoff [85]. They predict the following relation in the case of a perfectly ballistic junction:

$$I_C = \frac{\pi \Delta}{2eR_N}. \quad (2.12)$$

In our samples, we do not expect perfect ballistic transport. Accounting for scattering in the weak link but still in the short junction limit ( $L \ll \xi$ , when the phase picked up by the electron and hole can be neglected), the relation becomes [86]  $e \cdot R_N \cdot I_C \simeq 1.326\pi\Delta/2 \simeq 2.07\Delta$ . In the long junction limit, we have  $e \cdot R_N \cdot I_C \simeq 3.2\Delta_g$  [87], where  $\Delta_g = 3.1E_{\text{Th}}$  is the gap energy of the proximitized weak link. We can thus determine whether or not the junction is in the short limit with the help of the ratio

$$\eta = \frac{R_N I_C}{\Delta/e}, \quad (2.13)$$

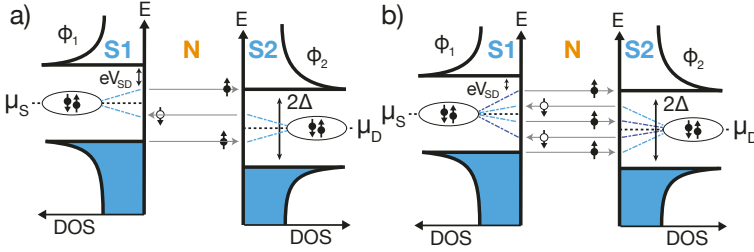


**Figure 2.5 Multiple Andreev reflections at an S-N-S interface.** a) Multiple Andreev reflection for  $V_{SG} = 2\Delta/3$ , involving two Andreev reflections. b) Multiple Andreev reflection for  $V_{SG} = 2\Delta/5$ , involving four Andreev reflections. Figure adapted from [41].

where  $\eta \rightarrow 2.05$  for a perfect interface and  $\eta \rightarrow 10.38E_{th}/\Delta$  for the ballistic long junction [86, 88]. Experimental reports in graphene show  $\eta$  to plateau at 0.55 [87] for a short junction and  $\eta \rightarrow 0.34E_{th}/\Delta$  for a long junction, the Thouless energy being determined by the temperature dependence of the critical current.

### 2.4.1 Multiple Andreev reflections

Suppose the chemical energy difference of both superconductors is less than  $2\Delta$ . A quasiparticle cannot tunnel directly, as is the case in the N-S junction, because there are no available states according to BCS theory for  $\varepsilon < \Delta$ . As discussed above, the supercurrent can carry Cooper pairs elastically across the junction through simultaneous Andreev reflections. Another possible elastic transport process involves multiple Andreev reflections when the source-drain bias satisfies  $V_{SG} = 2\Delta/n$ , as illustrated in Fig. 2.5: a quasiparticle undergoes an Andreev reflection, retro-reflecting a quasiparticle at energy  $\varepsilon = 2V_{SD}$ , which in turn reflects at the original interface, generating a retroreflected quasiparticle; this process is repeated  $n$  times, until  $neV_{SD} = 2\Delta$ , where the final reflection creates a particle which tunnels in the right-hand superconductor. A more detailed analysis [89, 90, 91, 92] finds that the effect of multiple Andreev reflections depend on the transparency of the conduction channels: for transparent junctions, multiple Andreev reflections manifest as *dips* in an enhanced conductance in the  $\pm 2\Delta$  region. Also important to note is that an  $n$ th-order Andreev reflection requires  $n$  separate conductance channels to be available.

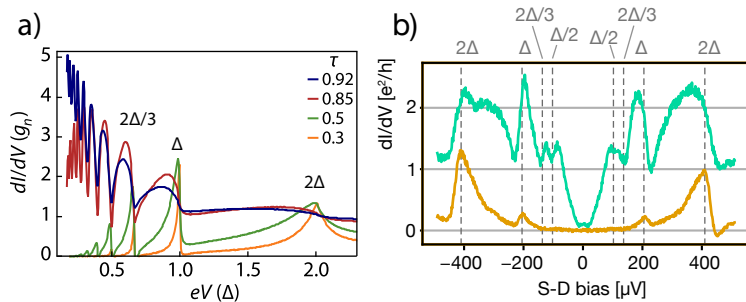


**Figure 2.6 Differential conductance resulting from Multiple Andreev reflections.** **a)** Theoretical prediction of differential conductance of multiple Andreev reflections. Figure adapted from [92]. **b)** Data from chapter 6 showing multiple Andreev reflections for low plunger gate voltage (yellow) and higher voltage (turquoise).

# 3 Device Fabrication and Experimental Methods

---

*Ce café tombe dans votre estomac (...) Dès lors, tout s'agite: les idées s'ébranlent comme les bataillons de la grande armée sur le terrain d'une bataille, et la bataille a lieu. Les souvenirs arrivent au pas de charge, enseignes déployées; la cavalerie légère des comparaisons se développe par un magnifique galop; l'artillerie de la logique accourt avec son train et ses gargousses; les traits d'esprit arrivent en tirailleurs; les figures se dressent; le papier se couvre d'encre, car la veille commence et finit par des torrents d'eau noire, comme la bataille par sa poudre noire.<sup>1</sup>*

Honoré de Balzac

In this chapter, we present the experimental methods employed in order to obtain the samples whose measurements are presented in the following chapters. We will first review the basics of the semiconductor nanowire growth done by our collaborators in Copenhagen and Pisa, then discuss the process of designing and fabricating devices around these nanowires, before finally briefly introducing the standard measurement setup.

---

<sup>1</sup>The coffee falls in your stomach (...) then, everything sets in motion: ideas set forth like the battalions of a great army on the battlefield, and the battle takes place. Memories come, charging, with deployed banners; the light cavalry of comparisons rides, galloping; the artillery of logic rushes up with its baggage train and shells; wit arrives, skirmishing, figures are created; the paper is covered in ink, the night starting and finishing with a torrent of this black water, like the battle with its black powder.

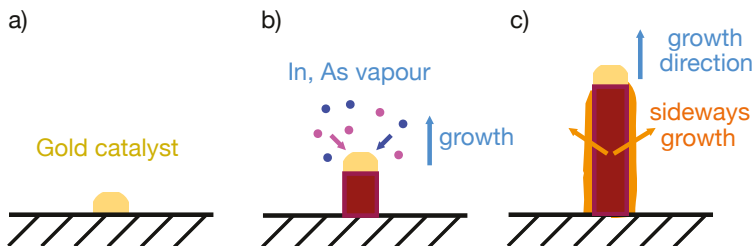


**Figure 3.1** Vapour-liquid-solid nanowire growth. a) a gold droplet is deposited on the substrate. b) In and arsenide vapor are introduced into the growth chamber, which leads to the wire growing from the catalyst (c)

### 3.1 Introduction

The experimental work presented in this thesis is the result of two phases: fabrication of devices and their measurement. In the former, we fabricate a device around nanowires provided from collaborators yielding a sample which is then probed in the latter. In this chapter, we will present fabrication, covering all the required steps until the sample can be measured, and then quickly present standard measurement techniques. The results from these experiments will then be presented and discussed in the following chapters.

### 3.2 InAs semiconductor nanowires

Semiconductor nanowires are single crystal quasi 1-dimensional structures with diameters in the range of a few tens of nanometers and lengths in the micron scale. A wide range of semiconductors can be used to synthesize them: the binary group III-V (GaAs, GaP, InAs and InP), the ternary III-V materials (GaAs/P, InAs/P), or binary II-VI compounds, as is summarised in [93]. In this thesis, we will exclusively use semiconductor nanowires made of indium arsenide, InAs, which presents the advantage of a strong Rashba spin-orbit interaction [94], low effective mass and high electron mobility [14, 39]. We will now provide an overview of wire growth as well as the nanowire electronic properties, following refs. [43, 50, 39].

### 3.2.1 Nanowire growth

Most semiconductor components or circuits are fabricated using a *top-down* process: a bulk crystal is selectively doped, etched or generally processed, the resulting individual components being then a processed part of the bulk. Most nanowires, however, are synthesised using a *bottom-up* process: the nanowire is grown on top of the substrate. A widely used method for nanowire growth is the vapour-liquid-solid (VLS) method [95], whose working principle is sketched in fig. 3.1 a): a catalyst metal particle, gold in the growth of our collaborators, is deposited on the growth substrate. These gold particles are either randomly distributed or patterned to be at a precise location. In a second step, the growth semiconductor materials are vaporised in the growth chamber in vacuum. The evaporated materials diffuse into the catalyst particle, eventually saturating it and forming into a crystalline structure, as shown in fig. 3.1 b-c). The growth rate of the wire depends on the size of the catalyst, with smaller gold catalyst particles producing faster-growing and thinner nanowires.

The growth of defect-free semiconductor nanowires requires such equipment and know-how, that only a handful of research groups in the world dedicate their efforts to it. As such, the research presented here uses out-of-house grown nanowires from the Sorba group in Pisa and the Nygard group in Copenhagen.

The environmental parameters of the growth influence not only the growth rate but also the crystal phase in which the wire grows, which can either be zincblende, the phase of bulk InAs, or wurtzite[39]. Left unchecked, the mixing of the crystal phases has an effect on the transport properties of the wire due to a mismatch in band gaps [96]. However, this difference in electrical properties can be exploited by engineering the crystal phase, or alternatively changing the semiconductor compound during wire growth. This can be used to introduce a potential barrier in the wire, which can then be used to define a quantum dot [97, 98, 99, 53, 100, 39].

A significant technological advance was achieved with the evaporation of epitaxially matched superconductors in the growth chamber of the nanowire, before the surface is exposed to oxygen and oxydises, as reported in [101, 102], with transverse electron microscope images confirming the atomic quality of the defect-free interface. Aluminum is particularly well suited to being evaporated on InAs, the lattice size matching within 0.3%, making large domains of epitaxially matched InAs - Al interface possible [101]. This method is referred to as *in-situ* Aluminum shell growth.

### 3.2.2 Double nanowire growth

Designing double nanowire devices initially was achieved by post-selecting randomly deposited nanowires, some of which would stick in pairs [103, 104], a method that forbids the deposition of an *in-situ* shell. By placing the catalyst

particles in close proximity, it is possible to grow two nanowires next to each other, which then join, forming an Eiffel-tower-like shape. Using this method, a superconducting shell can be deposited with the wire pair still in the growth chamber. This was achieved by the Nygard group, which generously supplied us with the double nanowires used in this thesis [105].

However, the shell has to be removed in order to contact the wires that are short-circuited by the omnipresent Aluminum. This step requires etching, which then creates impurities. An elegant solution was found by the Nygard group: growing wires in the path of the aluminum evaporation whose only purpose is to shadow part of the wire pair during evaporation [105]. The shadow wires are kept shorter than the wire pair by depositing a larger catalyst, which makes them grow at a slower rate.

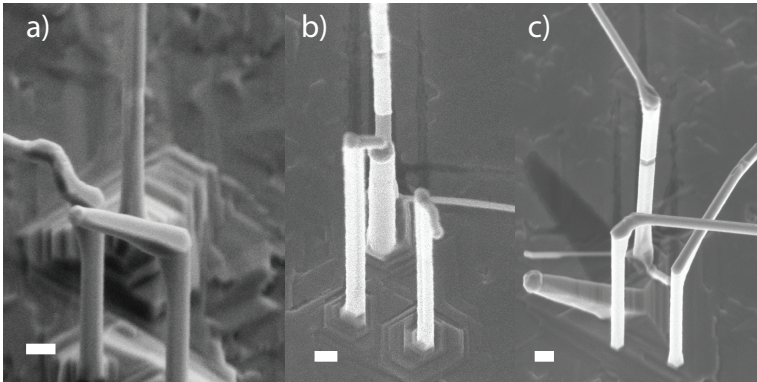


**Figure 3.2 Shadowed double nanowires.** The scales bar represents 200 nm **a)** Slit shadow, providing an *in-situ* S-Wire-S device. **b)** Slit and shadow wire, providing an *in-situ* Coulomb island with both a Wire-S and S-Wire-S interface. **c)** Unsuccessful shadow wire growth, but the slit still provides for an *in-situ* Josephson junction.

Further, more elaborate schemes were even implemented, wherein the shadow wire was grown with a bend, by changing the growth parameters. This makes the shadow take the form of a slit, and allows for a purely in-situ evaporated double nanowire Josephson junction. An electron micrograph of such a wire pair, imaged still on the growth chip, is shown in fig. 3.2. We note the tendency of slit shadow wires to bend outwards, not shadowing the wire pair, leading to a low success rate overall, estimated at 10-20 for a 50x50 matrix.

### 3.2.3 Electronic properties of InAs Nanowires

We will now briefly present the most relevant electronic properties of the nanowires, following references [43, 50, 39]. InAs is a III-V semiconductor arranged in a zincblende crystal phase, with a bandgap of 0.42 eV and a  $g$  factor of  $g = -14.9$  [106], the wurtzite crystal phases having a slightly larger bandgap (0.52-0.54 eV)[99]. Zincblende InAs has the peculiar property that charges accumulate on the surface, pinning the Fermi energy in the conduction band [107], making quality ohmic contacts and requiring negative gate voltages to deplete the wire [39], which is consistent with the experimental data acquired in this thesis.

In InAs nanowires, confinement in two dimensions forms transverse modes, leading to a sub-band structure  $E_n(k_x) = E_n + (\hbar^2 k_x^2)/(2m^*)$ , with  $E_n$  the energy of the  $n$ th quantised mode. In the case of ballistic transport, as reported for InAs nanowires in [108, 109, 110], the current  $I$  is given by  $I = (e^2)/hN\Delta\mu$ , where  $N$  denotes the amount of occupied modes [50]. This leads to a step-wise increase in conductance each time a channel is occupied. All our experiments use large diameter wires ( $\geq 70$ nm), except for the reports in chapter 5, which use 40nm InAs wires. It is worth noting that similar wires have exhibited electron mobilities up to  $6600 \text{ cm}^2/(\text{Vs})$  [14]. Electron mobility has been found to decrease significantly for diameters  $\leq 40$ nm, probably due to scattering from surface defects [111].

## 3.3 The fabrication workflow

In order to probe the physical phenomena studied in this thesis, a device is designed and fabricated starting from semiconducting nanowires, which are obtained on the growth wafer from the groups of Lucia Sorba and Jesper Nygard. These devices then require cooling down to cryogenic temperatures to suppress thermal excitations, and electrical source and drain connections to amplifying and measurement equipment. Additionally, gates and other electrodes are required to control the device. This process - colloquially named *fabrication* - starts with a bare wafer and ends with a sample in a cryostat, which is connected to a break-out box, where the measuring equipment can be connected.

### 3.3.1 Base structures

The *base structures*, shown in figure 3.3, are the basis of the fabrication process: a square-shaped cleaved piece of silicon wafer with an evaporated gold structure. Contact lines serve as intermediates between the device fabricated and the bond wires, contacted on the inner side by evaporation of the source

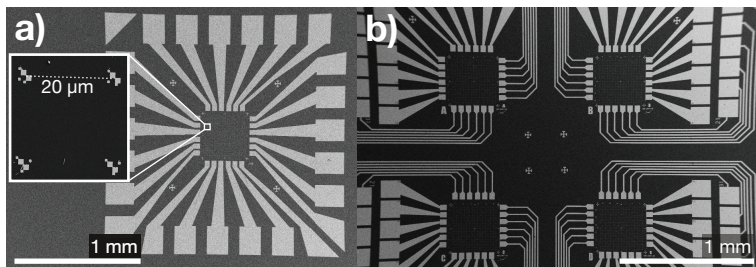


**Figure 3.3 Simple and quadruple base structure** a) The original design of the base structure provides 24 contacting lines, detail of the marker matrix shown inset, with a marker to marker pitch of 20  $\mu\text{m}$ . b) The lines are quadrupled with the improved design, with the matrix pitch reduced to 10  $\mu\text{m}$ .

and drain contacts, and connected on the outside by bonding to the chip carrier which plugs into a connector in the cryostat.

In order to fabricate double nanowire devices, situating them with sub-10 nm precision is required. Wires are thus deposited on the inner part of the base structure, where a matrix of markers with a 10  $\mu\text{m}$  pitch, down from an original design pitch of 10  $\mu\text{m}$ . Square designations on the markers designate the (x,y) coordinates of the marker, making the location of the imaged nanowire possible.

The individual contacting of double nanowires required in this project is at the limit of the precision of the electron-beam lithography, which is a repurposed 25keV imaging scanning electron microscope. Thus, a low yield of  $\sim 25\%$  at best is to be expected, the misaligned contacts rendering the remaining devices unusable. The advantage in quadrupling the amount of contact lines is the possibility of fabricating the quadruple amount of devices, then selecting the successfully fabricated devices for wire bonding and cooling down the sample. Although it was already possible to fabricate multiple base structures in the same fabrication run, simultaneous cooldown of successfully fabricated double nanowire devices on different marker matrices was impossible.

These base structures were fabricated in-house. Starting with a p-doped silicium wafer topped by a 400nm silicium oxide at the surface, the base structure was patterned by electron beam lithography, depositing a 5/55 nm Ti/Au layer. Another improvement during the work of this thesis was to standardise the base structure size to 4.2mm, thus simplifying handling during the remainder of the fabrication.

### 3.3.2 Wire deposition

The molecular beam epitaxy-grown nanowires are delivered on the original growth wafer. The wires are then transferred to our base structure for device fabrication. There are two methods for transferring the nanowires from the growth chip to the base structure. The simplest option, referred to as "dry deposition", consists in swabbing a piece of regular lab wipe on a corner of the growth chip and then depositing wires on the base structure. This transfer method is satisfactory when there are a large number of wires on the growth chip. Once the wires are deposited, scanning electron micrograph imaging allows for the post-selection of adequate wire pairs, ideally isolated from neighbouring wire bunches and sticking together by Van-der-Waals attraction.

This dry deposition of nanowires and post-selection of nanowire pairs requires a large number of available wires, since the yield, although we didn't quantify it, is estimated to be in the 1% range. This may not be an issue for growth chips having densely packed wires, but it becomes problematic in the case of 50x50 matrices of grown double wires, where only a few pairs show the desired shadowing and defect-free growth.

For the shadowed double nanowires, a micromanipulator was used. An optical microscope allows for the selection of the desired wire, which, having a thickness of  $\sim 100$  nm, is at the limit of the resolution of the optical microscope. The needle probe of the micromanipulator is introduced between the shadowing wire and the wire pair in order to avoid picking the unwanted shadowing wire, which can then stick to the desired wire pair. We obtain a transfer yield estimated at 20%, being mostly limited by the random orientation of the deposited wires.

### 3.3.3 Readout of the nanowire position and design of the devices

After the deposition of the wires, an array of scanning electron micrograph images are taken in order to locate and select the nanowires adequate for device fabrication. In order to accelerate this process, a python program was written: INEPT (the Incredible Nanowire Exact Placement Tool). Using the PyQt graphical user interface environment, the program loads the scanning electron micrographs, registers the user's location of the marker coordinates, marker position, and nanowire position, then exports the located nanowires in DXF format. The devices are then designed, placing source and drain contacts as well as plunger sidegates, using the computer-assisted design program associated with the electron microscope, Elphy.

### 3.3.4 Nanowire contacting

A challenging aspect of nanowire fabrication is achieving reliable electrical contact to the nanowires. The InAs nanowire surface gets oxidised when it

comes in contact with air, creating a 2 to 3 nm oxide shell. The latter is an insulator and needs to be removed before deposition of the contact metal. The quality of the resulting contact influences the coupling strength of the nanowire segment to the source and drain, as well as the local doping of the nanowire, and has important consequences on the measurements of the device.

### 3.3.5 Required accuracy

In order to individually contact single 40nm nanowires, a design accuracy of about 20nm is required, which is at the limit of the precision of the electron microscope used for lithography. The following steps were undertaken to optimize the accuracy of the fabrication:

- The marker matrix size on the base structure was reduced from 20 to 10  $\mu\text{m}$ .
- The highest magnification of the electron microscope was used, reducing the possible writefield to a 50  $\mu\text{m}$  square.
- The development of the exposed PMMA was done at colder temperatures ( $-20^\circ\text{C}$ ), reducing the sensitivity of the resist and increasing the electron dose required for lithography.

### 3.3.6 Bonding and building in the Cryostat

Once the device is fabricated, the quality of the contacts is measured at room temperature employing a needle probe. It is then glued using silver paste into a chip carrier, which fits into a 20-pin socket in the cryostat. Each pin of the socket is connected to a line with incorporated filters in the cryostat, leading to high temperatures at the points where a break-out box connects each line to a standard Bayonet Neill–Concelman connector. These 20 possible contacts allow a maximum of three 6-terminal devices to be measured in the same cooldown. The chip carrier provides access to these lines in the form of gold pads. A single gold pad is connected with silver paste to the back plane of the wafer piece on which the sample lies, to be used as a backgate, while the remaining ones are wire-bonded to the bondpads of the base structure. Since bonded samples are extremely sensitive to electrostatic discharges, it is imperative to stay electrically grounded when building in the sample into the cryostat. This is achieved by the means of grounding bracelets, shoes, and an ionizing fan providing a background of conductance to the air. Although these steps do not represent a technological challenge, they are statistically the steps where devices are most likely to be inadvertently destroyed, mostly by electrostatic discharge. The average survival rate for wires confirmed to have been successfully contacted by needle probing built into the cryostat is approximately 2/3.

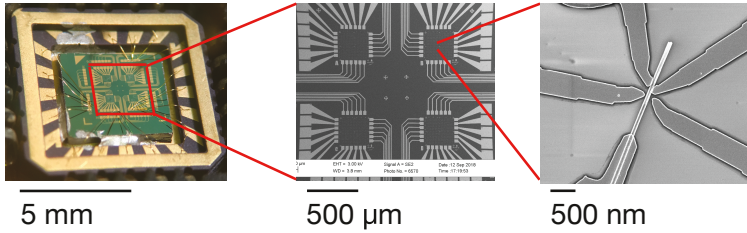


**Figure 3.4** Overview of the length scales, from the  $\sim 8$  mm wide sample holder to the mesoscale devices.

### 3.3.7 Process optimizations

Although nanowire fabrication was a well-mastered process in our group, multiple aspects were optimised for the needs of this work: INEPT, the wire location tool, was written, the base structures were quadrupled in contact numbers with a matrix pitch halved, cold resist development was used, and thermal contact in the evaporator was greatly improved by introducing a soft thin indium layer between the sample holder and the sample. Indeed, when clamping the crystal sample to the hard metal sample holder (which is out of copper and coated by whatever metal was previously evaporated), the actual contact surface at the back side of the unpolished sample and at the holder itself is rough and very small. This improvement was the result of the observation that it was impossible to evaporate a 20 nm Aluminum layer without the layer spontaneously forming droplets. Such behavior was not anymore observed with in the new sample holder designed for better thermal contact.

## 3.4 Measuring

This section presents a brief overview of the various methods we used to measure the fabricated devices. All the described methods are standard in the field of transport.

### 3.4.1 Dilution refrigerator

Low temperatures are crucial to the investigation of quantum mechanical effects and superconductivity, since the former involves small energy scales, and the latter is an effect observed under the critical temperature of 1.2 K in the case of aluminum. Observing physical effects on a small energy scale, of typically  $10 \mu\text{eV}$ , requires the suppression of thermal excitations which have an energy  $\sim kT$ . Thus, if one wants to resolve a feature in the  $20 \mu\text{eV}$  range,

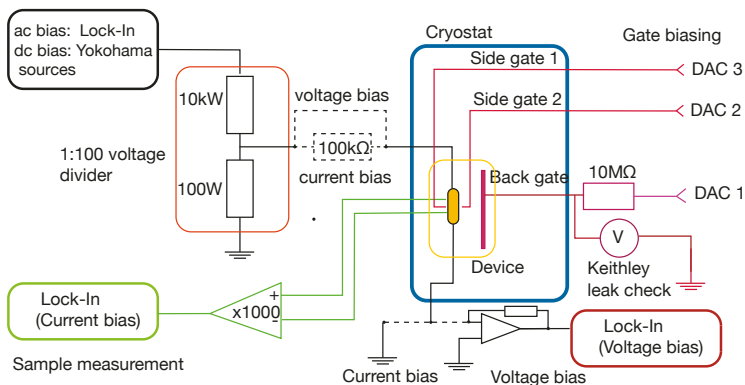


**Figure 3.5** Sample electrical connections in the cryostat. Both voltage and current biasing schemes are shown, as indicated. The DAC are the output of the digital to analog card used to drive the gates. The cold filters of the cryostat are not shown.

one needs to cool the electron at  $20 \mu\text{eV}/k \simeq 230 \text{ mK}$ . Cooling a sample down to  $4.2 \text{ K}$  is straightforward: it is the temperature of a liquid helium bath at atmospheric pressure, in which dipping a sample would suffice. A further reduction of temperature can be achieved by pumping on a helium bath, creating a vacuum which reduces the equilibrium temperature to  $\sim 1.4 \text{ K}$ . However, cooling to lower temperatures requires a more sophisticated technology, the dilution refrigerator, in which the endothermal process of mixing the  $^3\text{He}$  and  $^4\text{He}$  isotopes is exploited: below  $830 \text{ mK}$ , a  $^3\text{He}$ - $^4\text{He}$  mixture separates into a  $^3\text{He}$ -rich phase and a  $^3\text{He}$ -poor phase. In the  $^3\text{He}$ -poor phase,  $^4\text{He}$  is a superfluid whereas  $^3\text{He}$  a Fermi liquid. The superfluid behaviour can be used to isolate the  $^3\text{He}$  for circulation. The latter is heated, evaporating and thus circulating the separated  $^3\text{He}$ , which is pumped by a pump at room temperature, allowing the system to reach a base temperature  $\sim 25 \text{ mK}$ . The electron temperature in our setups is in the order of  $\sim 100 \text{ mK}$ , as was characterized in [53].

### 3.4.2 Electric setup

As already mentioned, 20 lines come up from the sample holder out of the cryostat into a cable bundle, which is connected to a break-out box where the lines can be individually connected using BNC connectors. DC gate lines are connected through a bandpass pi filter to a voltage source. For the source and drain, two alternative setups are used, configured to either voltage bias or

current bias the sample, depending on whether we desire a constant voltage from the source to the drain or a constant current through the sample.

### Voltage biased setup

In order to inspect the electric transport properties of the sample, a mixture of a DC and small AC (177 Hz) voltage is applied (fig. 3.5 ). The current flowing through the sample is measured by an I/V converter with a  $10^7 V/A$  amplification. A lock-in amplifier separates the AC component of the measured current, effectively filtering the signal for a single frequency. The DC component of the signal can also be measured by connecting the I/V converter output to both the lock-in and a voltage meter through a T piece.

The lock-in output is linearly related to the differential conductance of the device, whereas the DC output of the I/V converter gives DC current through the sample. Integrating the lock-in output from 0 bias voltage to a given value should result in the current recorded by the DC component of the I/V converter output.

### Current biased setup

For super-conductors, where the resistance is negligible over a given parameter range, it is sometimes beneficial to current bias the sample, effectively connecting a current source and measuring the voltage drop over the sample (fig. 3.5 ). The current source is simply done by applying a voltage through a large resistor in series with the measured sample  $R_{\text{bias}} \ll R_{\text{sample}}$  effectively applying a current  $V/R_{\text{bias}}$  through the sample . This current biasing is important for the super-current measurements, where analysing the current-biased I/V sample characteristic enables measuring the critical current  $I_C$ .

### Instrumentation control

The experiments were controlled using Qcodes libraries in a jupyter python notebook.



## 4 Andreev bound states in a double nanowire NS Junction

---

*N'imitiez rien ni personne. Un lion qui imite un lion n'est qu'un singe<sup>1</sup>.*

- Victor Hugo

We investigate double-nanowire N-S junctions, in order to gain an insight into the behaviour of charge carrying states in parallel wire segments coupled to a common superconductor.

We will first discuss the general characterisation of the devices, then look at bound states on individual wires. We will then bring both wire segments on resonance, and analyse the behaviour of the Andreev bound states in two experimental setups: one with uncoupled wire segments, and one with coherently coupled dots. We aim to characterize crossed Andreev pairing, which we find, in our samples, to be vanishingly small.

---

<sup>1</sup>Do not imitate anything, or anyone. A lion who imitates a lion is but a monkey

## 4.1 Introduction

A theoretical proposal [29] suggests a scheme in which a double nanowire coupled to a superconductor could host parafermions. The latter, which can be intuitively seen as fractional Majoranas, offer the advantage of a wider universal set of operations when braided [29]. A number of characteristics are required for these exotic topological modes to be hosted in such a device. Being coupled to four quantum dots to allow the full spectroscopy of the device, the wires must exhibit different Rashba spin-orbit interactions. The superconductor must have a pristine interface to both nanowires. In addition, the pairing potential of two electrons in the quantum dots coupled to the superconductor must be dominated by crossed Andreev pairing [29], which is equivalent to a three terminal Cooper pair splitting efficiency of  $> 50\%$  on each side of the superconducting island, in other words we require a dominating non-local transport of Cooper pairs. Further requirements are control of the chemical potential and a strong electron-to-electron interaction.

First experiments in a three-terminal N-Wire-S device demonstrated Cooper pair splitting with an efficiency of 30% [104], with evaporated Aluminum as the superconductor. Progress in nanowire growth techniques allows for a shadowed Aluminum shell to be evaporated *in-situ* [105], eliminating the need for removal by etching of the nanowire shell, as this step is known to introduce defects. Therefore, it is expected that the better interface would improve this Cooper pair splitter efficiency.

In order to probe the properties of these new wires, we fabricated a set of devices. The latter have common source and drain contacts, which allows fabrication with a much higher sample yield, and offer much lower contact resistance than individually contacting the nanowires.

## 4.2 Fabrication and geometry

Figure 4.1 describes the device discussed in this chapter. As presented in more detail in Chapter 3 and shown schematically in fig. 4.1 a), the samples are based on an epitaxially grown double InAs nanowire, followed by a shadowed *in-situ* aluminum evaporation. Wires are transferred onto a base structure using a micro-manipulator. Side gates and source and drain contacts, consisting of a  $\sim 100$  nm thick Pd normal metal are evaporated in UHV with a residual pressure of approximately  $5 \times 10^{-9}$  mbar, after removal of the native oxide by argon milling both on the nanowire and the aluminum shell. As a result, we note that the only superconductor in this device is the aluminum superconducting *in-situ* deposited shell (growth discussed in Chapter 3). A scanning electron micrograph of such a fabricated device (referred to as device E in the text) is shown in 4.1 d). The two sidegates capacitatively couple to both wire segments and allow us to control the chemical potential of each wire segment.

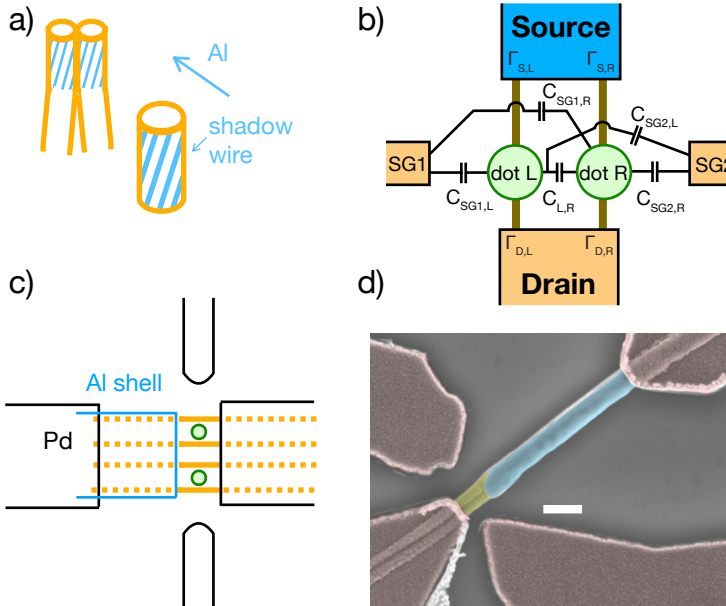


**Figure 4.1** Device fabrication: **a)** Schematic representation of shadowed double nanowire growth. **b)** Electrical model showing the relevant capacitances, source and drain capacitive couplings omitted for clarity **c)** Device layout **d)** False-color scanning electron micrograph of device E, with the shell in blue, nanowire segments in yellow, and 110 nm evaporated Pd in red.

sample	$l_j$	$E_C$	2 SG	AC	$\Gamma_S, \Gamma_N$
A	$\sim 300$ nm	$\sim 0.2$ mV	NO	YES	0.1, 0.01 mV
B	$\sim 150$ nm	$\sim 1.5$ mV	NO	YES	1.45, 0.6 mV
C	$\sim 150$ nm	$\sim 1.5$ mV	YES	YES	1.95, 0.45 mV
D	$\sim 80$ nm	$\sim 2$ mV	NO	NO	1.8, 0.3 mV
E	$\sim 80$ nm	$\sim 3$ mV	YES	NO	1.91, 0.62 mV

**Table 4.1 Main characteristics of the measured devices.**  $l_j$ , the junction length, is estimated from electron micrographs. The charging energy  $E_C$  is estimated from the size of coulomb diamonds. 2 SG denotes full gate control. Anti-crossings (AC) are the presence of resonances with slopes attributed to different wires anti-crossing in gate-gate conduction maps.  $\Gamma_S, N$  are extracted from fits of the expressions in [51] on our data.

As shown schematically in figure 4.1 b) and c), both sidegates couple to the individual wire segments with capacitances  $C_{L/R,SG1/SG2}$ . As discussed in chapter 2, the ratio of  $C_{L,SG1}/C_{R,SG1}$  determines the slope of a single resonance in a gate-gate conductance map. A common backgate  $V_{BG}$ , omitted from the sketch for clarity, couples capacitively to both wires with  $C_{L/R,BG}$ .

We consider five devices labeled here A – E, with general characteristics summarized in table 4.1. We note that only devices C and E have both sidegates operational, devices A,B,D can only be controlled by the backgate and a single sidegate, with the drawback that the backgate has a lower lever arm. Indeed, having full control of all gates enables us with a finer selection of transport channels, as it will be shown later. The junction length was varied between devices, from long ( $\sim 300$  nm) to short ( $\sim 80$  nm). We find that reducing the junction length in subsequent fabrication runs led to more distinct conductance features.

All measurements were done in a cryostat at a base temperature of 27 mK using the standard Lock-in amplifier measurement techniques described in Chapter 3. A 3-axis magnet enables magnetic fields of arbitrary direction and of strength up to one Tesla. Samples B & C as well as D & E were fabricated and measured simultaneously, and thus fabrication parameters are identical in both cases.

### 4.3 Transport in the normal state

We first investigate the quality of the contacts to the wires. In order to remove the influence of superconductivity, we both measure at a temperature above the superconducting transition of aluminum  $T > 1.2$  K, and under the application of a magnetic field greater than the critical field of the aluminum superconducting shell ( $> 150$  mT). The wire segment is then effectively contacted

by two metals, and we investigate both the formation of dot-like resonances and conductance plateaus depending on the experimental parameters.

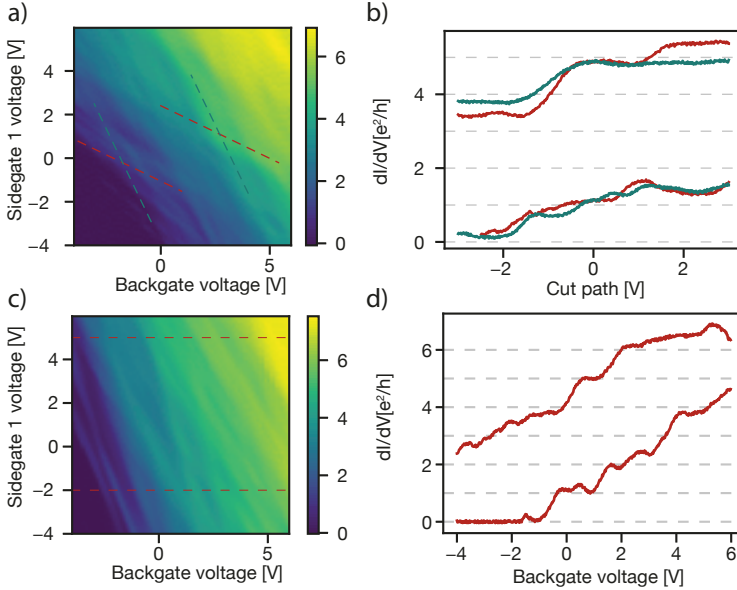


**Figure 4.2 Conductance plateaus** in sample B and C at 4K. **a), c)** Differential conductance as a function of both plunger gates of samples B and C, respectively. **b), d)** Selected cross-sections of a) and c) demonstrating conductance steps and plateaus.

### 4.3.1 Sample characterisation at $T = 4$ K

We first consider the conductance of our double wire junction at  $T = 4$  K. Shown in fig. 4.2 a) and c) is the differential conductance plotted as a function of both plunger gate voltages in samples B&C. Since a sidegate on sample D is inoperative, we use the remaining sidegate and the backgate to control the device. On the bottom left, both gate voltages are negative, depleting the wire segments and suppressing conductance. Then, as we progressively increase the voltage on the sidegate, effectively moving right, the chemical potential is gradually increased in the wire closer to the sidegate, thus enabling and increasing conductance, as already introduced in chapter 2. In contrast to the sketched resonances in fig. 2.2, we observe a steady increase in conductance,

which indicates that the junction is not in the dot regime.

Shown in fig. 4.2 b) and d) are cuts at selected gate values. We note the presence of conductance plateaus, especially evident in sample C, at integer multiples of  $e^2/h$ , indicative of the ballistic nature of the electron transport through our device, i.e. indicating an electron mean free path in the nanowire  $\xi > l_J$ , the junction length. In addition, the fact that the quantisation occurs at  $e^2/h$  suggest the current-carrying channels are spin-resolved, even at 0 magnetic field. The cross-sections in b) also demonstrate that the quality of the coupling itself depends on the gate voltages. The cross-sections taken at higher gate voltage values demonstrate a clear  $\sim 1e^2/h$  (green line) step in conductance, whereas at lower gate voltage values the step size is smaller and less distinct, which we interpret as the plunger gates gating not only the chemical potential of the wire segments, but also the strength of the coupling to the source and drain contacts. In the case of the backgate, the microscopic process of this change in coupling strength can be explained by the center of mass of the electron wave function being pushed towards the screening metal of the contact. The phenomenology of this change will be further investigated in section 4.3.2. The excellent transport properties, comparable to other reports of ballistic transport in InSb and InAs wires [112, 113], indicate the excellent quality of the epitaxial growth and of the nanowire junction contacts.

### 4.3.2 Double wire transport with contacts in the normal state

We now consider similar measurements at the base temperature of 30 mK. An out of plane magnetic field of 200 mT ensures that the superconducting aluminum is quenched in the normal state. Figure 4.3 shows the differential conductance plotted as a function of both gate voltages for samples A,C,D,E. We recall that samples D & E have the shortest junctions with  $\sim 80$  nm, then sample C with  $\sim 150$  nm, the longest junction being that of sample A with  $\sim 300$  nm.

Chapter 2 discusses expected resonances and features for a double nanowire device in the dot regime. As expected, two sets of features with different slopes are attributed to the two wires. The ratio of these slopes is given by the ratio of capacitance e.g.  $C_{SG1-L}/C_{SG2,L}$ , which reflects the difference of lever arm to the different plunger gates and thus their lateral position in the junction. We note the absence of Coulomb interaction between the dot states in the shortest junctions (sample D and E), which we attribute to the proximity of metallic contacts screening the electric fields.

As reflected by the values extracted from Coulomb resonances and summarized in table 4.1, the level spacing of the dot states increases with shorter junctions. It is to be remarked that the confinement energy is the one of a particular dot state. The wire segments are multimodal, hosting multiple dot states with different confinement energies and self-capacitance, which depend

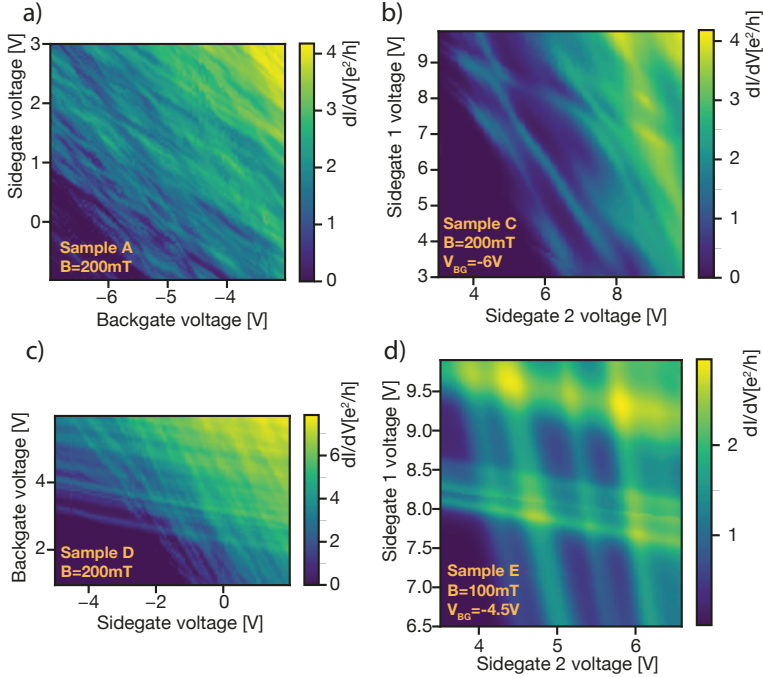


**Figure 4.3 Normal state conductance at base temperature.** a-d) Differential conductance plotted as a function of 2 plunger gates for samples A,C,D,E at 0 source-drain bias.

on plunger gate settings as well. However, the dot resonances used to evaluate the confinement energy were selected to be roughly similar, i.e. a resonance near onset of background conductance, and thus the extracted values reflect the energy increase with the smaller confinement size.

Coupling rates were extracted by fitting the lineshape of the resonances with the predictions of Beenakker [51] presented in section 2.1.4, which will be discussed in section 4.4.2.

The difference between our experimental results and reports using wires from the same origin [78] which exhibit lower conductance and typical Coulomb diamond behaviour is attributed to the larger transparency of our contacts.

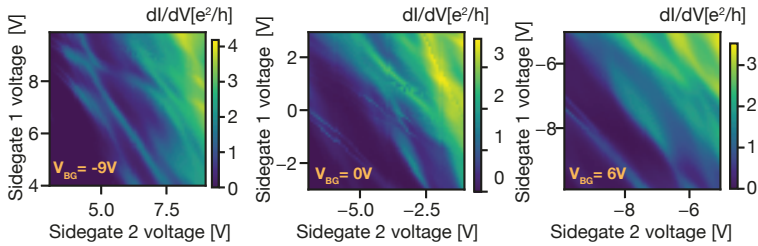


**Figure 4.4** Sidegate-sidegate conductance maps of samples E for different backgate voltage values of -9, 0, and 6 volts. In both cases, we notice sharper features for lower backgates.

### Full gate control

The Samples C and E can be controlled by both sidegates and the backgate. The backgate and sidegates couple differently to the wires and contacts. While the backgate changes the chemical potential of the wire segment and the contact barriers to a similar extent, the sidegates will primarily affect the chemical potential of the wire segments, the contact barriers being partially screened by the backgate and drain contact. Figure 4.4 shows the differential conductance measured on sample E plotted as a function of the two plunger sidegate voltages at backgate voltages of 6, 0, -9 V respectively. In order to span a similar range of chemical potentials in the wire, the sidegate voltage ranges were adjusted so as to explore the onset of conductance. As expected, we observe a sharpening of the resonances as we lower the backgate voltage from 5 to -9 V, which we attribute to the contact barriers being less transparent with negative backgate voltage.

## 4.4 Spectroscopy of the superconducting junction

The interface quality in a superconductor-semiconductor hybrid junction is critical for the observation of phenomena requiring the preservation of Cooper pair coherence [114] inside the semiconductor. It was also hypothesised as a critical condition for the observation of exotic topological states [115], sparking a strong material research effort [101] that yielded advances such as the *in-situ* aluminum deposition technique used in this work [116][117].

A key characterisation technique is transport spectroscopy of hybrid junctions. In the latter, the differential conductance of a semiconductor-superconductor tunnel junction is measured as a function of the applied bias voltage. In the weak tunnelling limit (transparency  $\tau \ll 1 \equiv \Gamma_{SD} \ll E_C$ ), a clean interface is characterized by the suppression of conductance when the Fermi level of the

semiconductor is within the gap ( $\pm\Delta$ ) of the superconductor. A finite conductance within the gap indicates the presence of quasiparticles, provided the junction is in the dot regime and within the short junction limit, i.e.  $l_j \ll \xi$ .

Hard proximity gaps have been reported for junctions that use *in-situ* evaporated Aluminum on InAs and InSb nanowires [118] [119]. In a recent work, junctions exhibiting a hard gap were realized by *ex-situ* evaporation after an oxide-removing cleaning step using atomic hydrogen [120].

#### 4.4.1 Superconducting gap

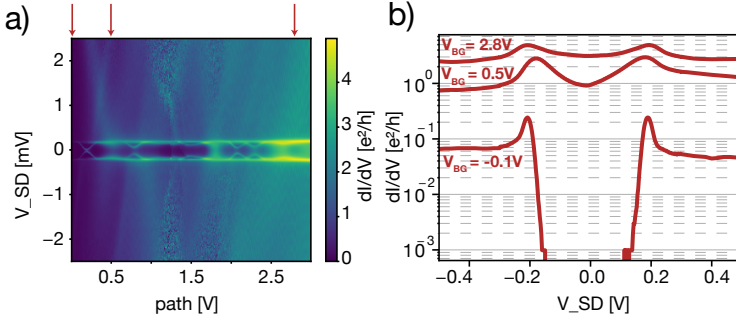


**Figure 4.5** a) Superconducting gap as function of sidegate, as measured on sample C b) Cuts at sidegate voltage values of  $-0.1$  V,  $0.5$  V and  $2.8$  V demonstrating hard gap near wire pinch-off and a in-gap conductance enhancement when the normal state conductance is at  $2 e^2/h$ . Normalisation, which is equivalent to moving the curves up or down in the log scale, was omitted to provide separation between the traces.

Figure 4.5 a) shows the conductance as a function of bias for a N-S tunnel junction as predicted by the BTK model. The dimensionless parameter  $Z$  characterises the transparency of the junction. Gap *hardness* is defined as the ratio  $G_N/G_S$  between normal state conductance, measured by applying a bias  $> 2 \times \Delta/e$ , and in-gap conductance.

In order to do spectroscopy of this gap, we set the junction up in the dot regime by applying  $-4$  V to the sidegate and then recording conductance as a function of both source-drain bias and gate voltage (both swept at the same rate), shown in fig. 4.5. Cross-sections at constant plunger gate voltage in fig. 4.5 b) demonstrate a hard gap  $G_N/G_S > 100$  at a mixed gate voltage  $0.5$  V. Under higher applied plunger gate voltages, when the junction becomes more transparent, we expect enhanced conductance within the  $\pm\Delta$  bias range, as

predicted by the BTK model [63]. The third cross-section of fig. 4.5, at 2.8 Volts shows the latter, and we estimate a Z factor of 0.45, an exact fit being hindered by the simplicity of the gap model, which assumes zero temperature and a perfect ballistic junction.

#### 4.4.2 Conductance in the superconducting state

Using the equation 2.7 from section 2.3.2, we can fit the resonances seen in the normal and superconducting conductance versus gate maps. The result of this fit is shown in figure 4.6. Fitting the functions reported in [51] delivers satisfying results, which is evidenced by a consistency check, shown in 4.6 b): for the first peak at  $-2.3$  V, plotting the  $G_N$  function with the  $\Gamma_{1,2}$  obtained by fitting the resonance in the superconducting state yields a good fit to the normal data (turquoise line) and, vice versa, the pink line shows the superconducting data fit in the normal state. The values extracted are summarized in table 4.1, where we assume the stronger  $\Gamma_S > \Gamma_N$ .

The obtained coupling rates  $\Gamma_{1,2}$  show that the junction is not in the dot regime, since  $\Gamma_S \sim EC$ . We assume the larger coupling to be that to the superconductor, the in-situ shell being expected to yield a better coupling. The results show an asymmetry of 1:3-1:10 between the coupling  $\Gamma_{S,D}$ .

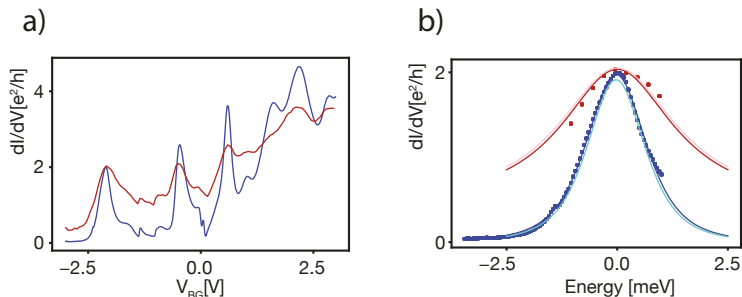


**Figure 4.6 Fitting the resonance lineshapes** a) Conductance as a function of backgate at 0 sidegate for sample C in the normal (red,  $B = 200$  mT) and superconducting state (blue). b) Results of fits on the first peak, with a background of conductance being subtracted from the normal state conductance. The red dots are normal state data, red line is the fit. Blue dots are the superconducting state data, with the fit plotted as a line. The pink line is the  $\Gamma_{S,D}$  resulting from the superconducting fit in the normal state function, and the turquoise the opposite.

## 4.5 Single wire Andreev bound states

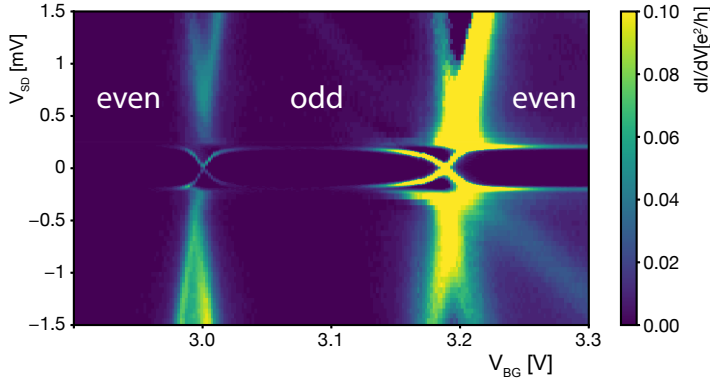


**Figure 4.7 Andreev bound states on a single wire on sample A** Single-wire Andreev bound state on a single junction, with the other junction depleted by the application of  $-9$  V on the Sidegate, demonstrating a clear even-odd pattern.

By depleting one junction with a sidegate and tuning the other to the onset of conductance, we can probe single-wire junctions in our double wire system. We then see clear odd-even state alternating bound states (data for device A in fig. 4.7). The qualitative shape of the Andreev bound state is consistent with a junction with weak  $\Gamma/U$  coupling to the superconductor, which is also consistent with the coupling rates summarised in table 4.1. This explains why this pattern of ABS was primarily observed in device A, which has the weakest coupling to the source and drain of all the devices measured in this chapter.

### 4.5.1 Magnetic field dependence

We now look at the magnetic field dependence of the Andreev bound states. Figure 4.8 a) shows a bias-gate conductance scan of a strongly coupled Andreev bound states. Applying a magnetic field parallel to the wires in b), we observe the Zeeman-like splitting with a  $g$  factor of approximately  $10 \pm 1$  by visually adjusting a guide to the eye line to the data in fig. 4.8. The observed value is lower than the measured bulk value of  $14.5$  [106]. The superconducting gap closes for a field strength above  $\sim 350$  mT, which is lower than what has been reported in nanowire heterostructures [31], or even for the device measured in chapter 6, which quenches at  $> 600$  mT grown shells. As shown in fig. 4.8

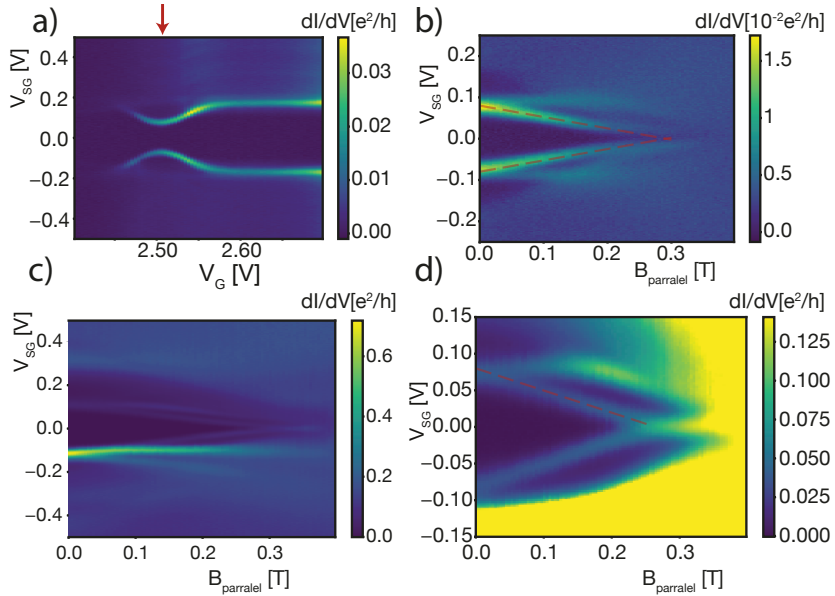


**Figure 4.8 Magnetic splitting of the Andreev bound states on sample D** **a)** Differential conductance as a function of bias and gate, with a cross-section displayed in **b)**, where the magnetic field parallel to the wire is swept. The red line indicates a  $g$  factor of 9.5. **c-d)** Two measurements taken at identical gate values, with **d)** at higher resolution. The dotted line indicates a  $g$  factor of 10.4.

c) and d), at a (backgate,sidegate) setting of (-1.1,1.1), sample D also shows split Andreev bound states joining at 0 bias.

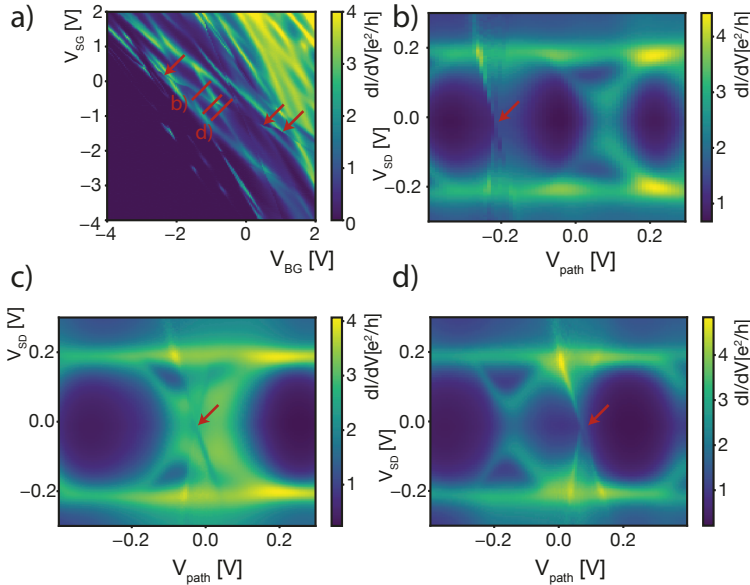


**Figure 4.9 Spurious dot** in sample B. **a)** Gate-gate differential conductance map at 0 magnetic field. **b-d)** Cross-sections (along the lines shown in a.) additionally scanning source-drain bias. The arrow highlights the sharp change in conductance.

## 4.6 Spurious dots

As it can be seen in the gate-gate map in fig. 4.9 a), the arrows point to a sharp feature in transport. In fig. 4.9 b) one sees a cross in the bias, reminiscent of a Coulomb diamond, but not appearing as a resonance but as a gate jump: the feature gates the junction measured in transport, acting as an uncontrolled gate. This could be interpreted as dots which are only coupled to the normal part of the wire but not the region proximitized by superconductivity: they ignore the gap, but when their occupation number changes, the presence of an additional electron capacitatively gates the channels that contribute to transport. Furthermore, in devices with both sidegates and the backgate, pushing the backgate to negative voltage while compensating with

the sidegates removes these features, hinting at a location of these spurious dots on the lower part of the device.

## 4.7 Overlapping single-wire Andreev bound states

We now investigate the behaviour of the Andreev bound states when both junctions are brought to resonance. A requirement for the hypothesised fractional topological states - whose quest was at the origin of this project - in double wire hybrids is a stronger crossed Andreev reflection transport process as compared to the co-tunneling of Cooper pairs. This can be probed in a Cooper pair splitter setup as reported in [104]. However, such an experiment requires individual contacting of the two wires, which our samples do not allow. Another signature of strong crossed Andreev reflexion is the Andreev molecular state [121, 77, 78]. As the latter is a coherent state spanning both wire segments and is coupled through the superconductor, its presence is revealed by a characteristic anti-crossings of the single-wire ABS [78]. To investigate the presence of these anti-crossings, we scan a region in which identified resonances of both wires are made to cross by tuning the plunger gates.

Figures 4.10 and 4.11 show the result of this effort: we explore the differential conductance  $dI/dV$  of the junction as a function of plunger gates and source-drain bias. In a) of both figures, we find overview conductance maps plot  $dI/dV$  as a function of plunger gates. In numbered cross section plots, plunger gates are varied along paths shown in the overview plot, and the source-drain bias is additionally swept. In fig. 4.10, the cuts are chosen so that each cut varies the chemical potential on both wires equally, while the chemical potential difference between the wires is altered for each cut. We see Andreev bound states overlapping, seemingly uncoupled to each other, their shape remaining identical, unperturbed by the Andreev bound states associated with the other wire. This superposition is well shown by the Andreev bound states highlighted by the yellow and white arrow. In fig. 4.11, the cuts are chosen so that the chemical potential is kept constant on one wire while scanned on the other. To help the reader orient himself, the star follows a single Andreev bound state crossing in all cuts. The slope of this particular bound state in cut 5 is due to the misalignment between the resonance and the cross section path which was chosen.

Surprisingly, neither sample D nor E, despite demonstrating good transport properties evidenced by large coupling rates  $\Gamma \sim E_{\text{add}}$  and a clean superconductor-semiconductor interface evidenced by a gap of hardness  $G_N/G_S > 100$ , exhibit such anti-crossings. As we will show in the next section, such anti-crossing was indeed observed in sample E, but did not disappear when the superconductor was made normal.

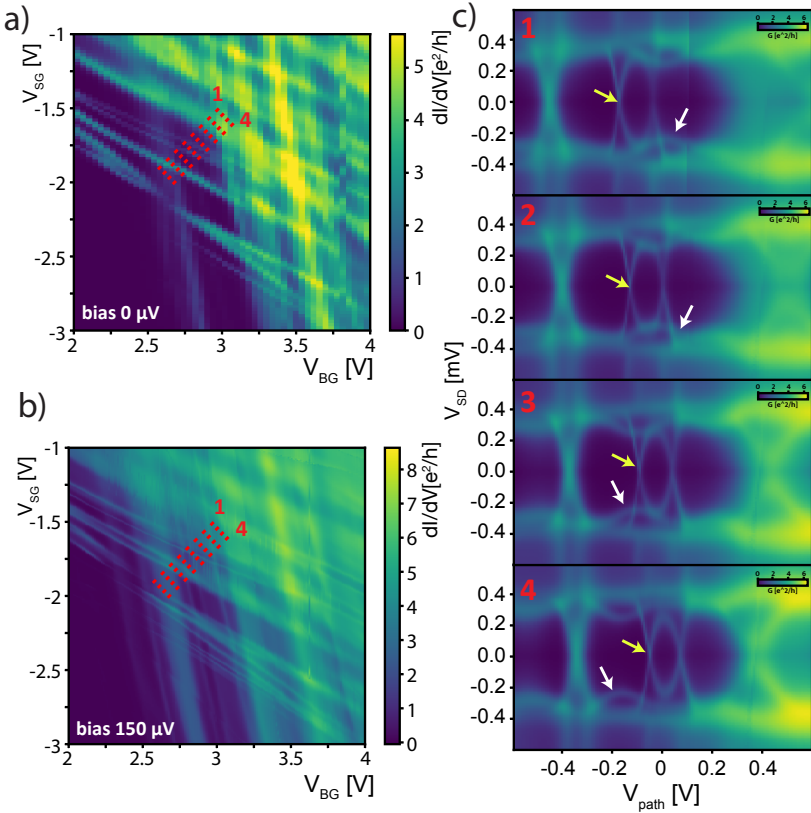


**Figure 4.10 Overlapping Andreev bound states** a), b) Gate-gate maps of  $dV/dI$  at fixed bias 0 and 150  $\mu V$  c) Bias/Gate maps along the red dashed lines in a) and c). We see multiple bound state spectra crossing without showing any anti-crossings or expected evidence of interacting, as reported e.g. in [78].

**Figure 4.11 Overlapping Andreev bound states** a), c) Gate-gate maps of  $dV/dI$  at fixed  $V_{SD}$  0 and 120  $\mu V$  b) Bias/Gate maps along the red dashed lines in a) and c). Taking perpendicular cuts allows for a more complete picture.  $\star$  Follows the bound state of a dot resonance through the maps and cuts.

## 4.8 Gap size artefact

Two features are present in the data presented in this chapter, the  $1-\Delta$  coherence peaks of the superconducting gap seemingly grow when both dots are on resonance, a possible signature of an additional coupling energy, and a region of inhibited conductance near 0 bias, evidenced e.g. by a horizontal dark line in the cuts of figure 4.11. Furthermore, the gap enlargement effect persists when voltage is measured in a pseudo-4-terminal setup, confirming that the applied bias truly corresponds to the voltage drop between the source and drain contacts.

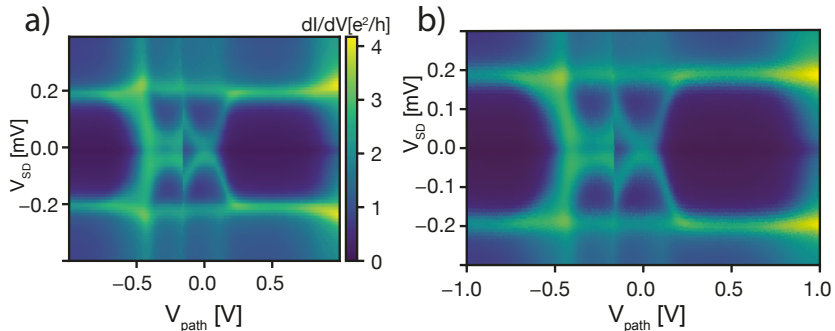


**Figure 4.12 Resistor in series** in sample E. **a)** Measured conductance plotted as a function of applied source-drain voltage bias and path mixing sidegate and backgate. **b)** Conductance as a function of actual junction voltage bias, assuming the source-drain voltage occurs over the junction *and* a  $3\text{ k}\Omega$  resistor in series.

However, accounting for a resistance in series to the N-S junction removes this effect, as shown fig. 4.12 which depicts the raw data on the left and the adjusted data on the right for a series resistance of  $2\text{ k}\Omega$ . Since both the DC and the AC components of the current through the sample are monitored, the voltage  $V_{\text{Series}} = I_{\text{Sample}} \cdot R_{\text{Series}}$  can be subtracted from the applied bias to yield the bare junction voltage drop. This suggests that this voltage drop is not part of the N-S junction but still occurs between the source and drain contacts of the device.

As a result, we find it extremely unlikely that this effect is the signature of a larger  $\Delta$  or has a relation to the N-S physics under study.

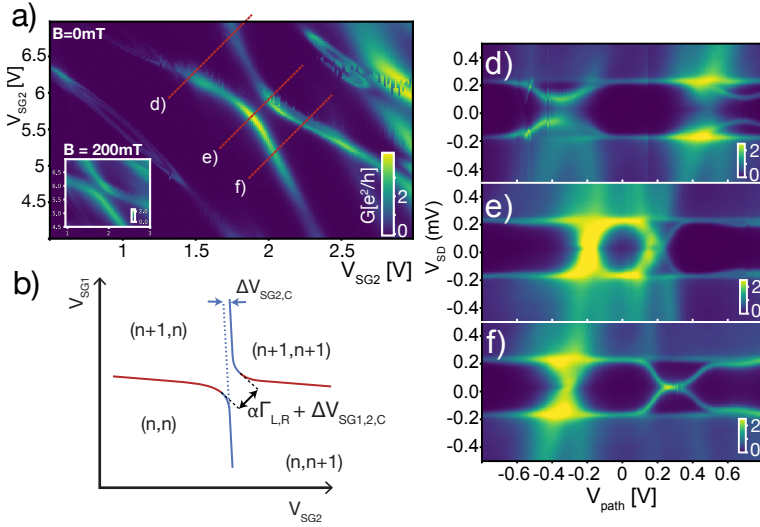


**Figure 4.13** a) Conductance at 0 bias in the superconducting state, with the normal state of  $B=200mT$  inset b) sketch of the expected conductance map for a coherently coupled double dot. d-f) Selected cross-sections of a) sweeping additionally bias.

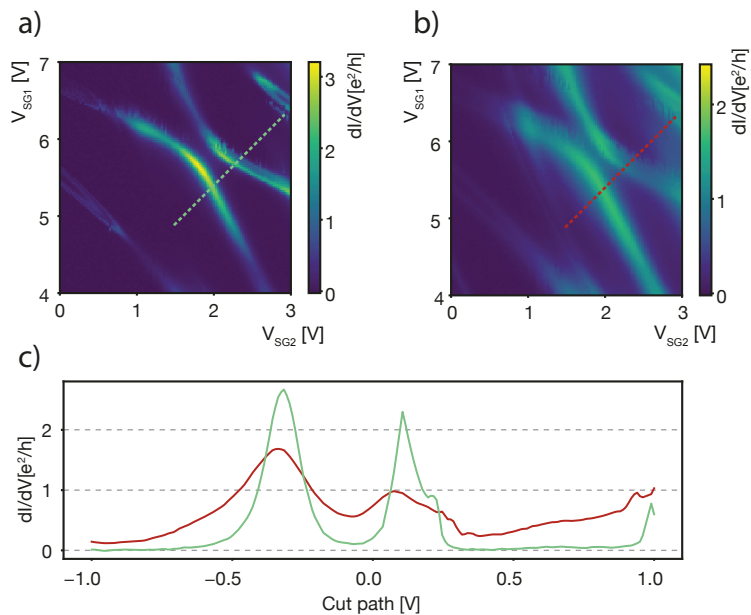


**Figure 4.14** Coherently coupled double dot in sample C. a), b) Differential conductance mapped as a function of plunger sidegates in the superconducting (left) and normal state (right,  $B = 200$  mT) Cross-sections in the normal and superconducting state shown in c).

## 4.9 Coherently coupled dot Andreev bound states in an N-S double junction

Recent work [78], [122] reports the coupling between Andreev bound states through the superconductor. In [122], the evidence relies on tuning the phase difference of one junction using a flux loop and observing the corresponding current-phase relation oscillations on the other. In [78], anti-crossing of Andreev bound states attributed to the individual junctions are observed.

In the lower left quadrant of Fig 4.13, a gate-gate map measured on sample E shows a clear anti-crossing of two bound states. Cuts of the states, while varying the bias are shown on the right hand side. Inset in the conductance map is the same parameter region mapped with the superconductor quenched to the normal state. Coherent coupling is evidenced by the anti-crossing of dot resonances attributed to separate wires. However, the anti-crossing persists in the normal state, when a magnetic field of 200 mT is applied out-of-plane, thus exceeding the critical field of the superconducting shell. This indicates a coupling mechanism independent of superconductivity.

Since the double wires join within the growth chamber, before the oxide shell is formed, it is not guaranteed that direct inter-wire tunnelling is forbidden. A contact between the wires could lead to dot states hybridising, and explain the observed feature. In the region of the anti-crossing, the single electron wavefunction would thus spread over both wires.

Although we do not see the expected disappearance of the anti-crossing under the magnetic field, we inspect the gate plots in the normal and superconducting states in order to quantify the strength of the coupling mechanism originating from the superconducting state. The distance between the resonances is the sum of two contributions: on one hand, capacitive cross-talk of the dot states shifts the resonances when an electron is added, a contribution we denote by  $\Delta V_C$ . The tunnel coupling between the dot states is denoted by  $\Gamma_{L,R}$ . Thus, the distance in a gate-gate map between the peaks is given by  $\alpha\Gamma + e\Delta V_C$ . The lever arm  $\alpha$  provides the conversion between the gate voltage applied and the energy scale. The top panels of fig. 4.14 compare the gate-gate conductance maps in the superconducting state (left) and the normal state (right), while the lower panel shows side selected cuts around the anti-crossing region of interest, with the two cuts representing  $dI/dV$  in units of  $e^2/h$  (red and green). We observe an increase in peak-to-peak distance no greater than  $\Gamma + e\Delta V_C/\alpha = 0.3 \mu\text{eV}$ , the convoluted nature of the right peak making exact fitting impractical. This value is the maximum of the coupling between the dot states associated with the resonances, which is influenced by the superconductor. Being an order of magnitude smaller than the other relevant energy scales of the system (dot level spacing, source and drain coupling strengths) would make an interaction of this strength challenging to observe.

## 4.10 Discussion

In conclusion, we demonstrated that the samples that we investigated exhibited excellent contacting properties with evidence of ballistic transport, hard gaps and transport in the superconducting state following the BTK model. Furthermore, on some devices we show precise control of the barriers, enabling the transition from a dot regime to a more ballistic regime of transport.

As expected, 70 nm junctions exhibit larger Coulomb charging energies, and therefore cleaner features. However, in these short junctions, no evidence of anti-crossings between Andreev bound states attributed to separate wires was observed. In the 120 nm junction, a clear signature of the anti-crossing of two Andreev bound states is observed. Furthermore, we could show that the coupling energy increases by no more than  $0.3 \mu\text{eV}$ . This value is half an order of magnitude below the thermal energy of the electrons in our setup, which makes a direct observation extremely challenging.

Another puzzle is the absence of Cooper pair splitting, which was observed in functionally similar double nanowire devices, reported in [104, 123]. Although these reports use a 3 terminal setup, our use of common source and drain contacts should not inhibit the Cooper pair splitting, which should show a conductance enhancement when both wires are on resonance, with  $G_{res} = G_{local} + G_{nonlocal}$ , i.e. the conductance of a crossing of two resonances should be greater than the sum of the conductance of the individual resonances. A clear difference between our device and the ones from the two reports is a higher value of the conductance peak height of resonances, indicating stronger coupling to the source and drain contacts. Ironically, the need for an epitaxial pristine interface might also be detrimental: the junction then cannot be in the dot regime, since  $\Gamma_S \sim E_{(n+1)-n}$ . As a direct consequence, the electrons' lifetime in the dot state is short, broadening the resonances and possibly weakening interaction effects.

# 5 Double nanowire Josephson junction

---

*All that is gold does not glitter, not all who wander are lost.*

- J.R.R. Tolkien

We now turn our attention to a double nanowire Josephson junction. The comparison of a double wire junction to a single wire Josephson junction, whose characteristics are well understood [124] [125], should yield an insight into the nature of non-local transport processes, specifically the identification of crossed Andreev pairing of the quantum states in both wires through the superconductor. In this chapter, we will first present the devices, characterise them in the normal state, and investigate the behaviour of the Josephson physics. Although work on similar platforms finds evidence for crossed Andreev pairing by probing a Cooper pair splitter [104], or observing non-local Josephson effect [122], correlation in the superconducting currents were not observed in this experiment, which we attribute to electron decoherence in the 230 nm long nanowire segments.

## 5.1 Device and characterisations

The samples are fabricated using post-selected wire pairs after dry deposition of 40nm InAs nanowires that were epitaxially grown by the Sorba group in NEST Pisa (see chapter 3 for fabrication details). Common aluminum source-drain contacts and a pair of sidegates were evaporated in a single step following native oxide removal by sulfur passivation, as shown schematically in fig. 5.1 a). A false-color electron micrograph of the device is displayed in fig. 5.1 b). The junction length was measured using the electron micrograph to be 230 nm. Two nominally identical devices were measured in a single cooldown, labeled A and B.

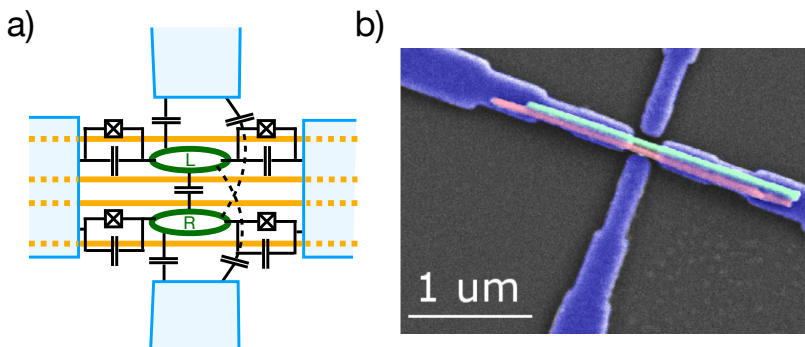


**Figure 5.1 Double nanowire Josephson junction** a) Electrical model b) False-color electron micrograph of the device

### 5.1.1 Transport in the normal state

We first focus on the characterisation of electron transport in the normal state. Figure 5.2 shows, in a), the differential conductance as a function of both plunger gates, and in b), selected cuts chosen so as to keep the chemical potential constant in one of the wires.

The characteristic crossing patterns are similar to the ones observed in the previous chapter, with the difference that the lever arm ratio between the sidegates is larger: we have a 15:1 ratio on one wire and 5.5:1 on the other. The asymmetry stems from the visible difference in the sidegate-to-wire distances between the two wires and leads to a better individual control of the chemical potential in the wire segments. Weak conductance plateaus above 5 Volts are observed, e.g. upper cuts in fig. 5.2 b). Thus, we conclude that the

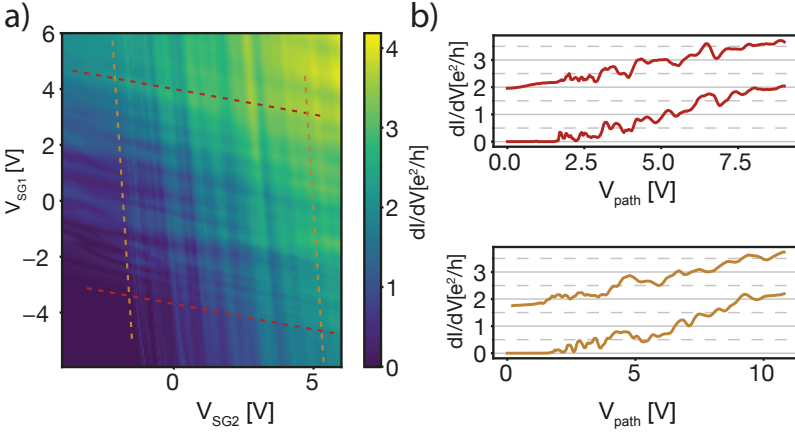


**Figure 5.2** a) Conductance in the normal state (out-of-plane magnetic field of 200 mT), measured on device A. b) Two cross-sections along paths chosen to keep one wire at constant chemical potential

high contact quality of the sulfur passivated wires enables us to see traces of quantized conductance, although the quality of the interface does not match the in-situ evaporated shell of the previous chapter.

## 5.2 A double InAs nanowire Josephson junction

Figure 5.3 a) shows the differential conductance as a function of source-drain bias. The  $\pm 2\Delta$  region exhibits enhanced conductance with dips at fractional values of  $2\Delta$ , which we identify as multiple Andreev reflections. Comparing these results to the modelling done in [92], these characteristics indicate a junction transparency greater than 0.5. In order to investigate the 0-bias conductance peak, we switch the electric setup to bias the junction in current and not in voltage.

Figure 5.3 b) shows the differential conductance in the superconducting state, as a function of bias current at 0 plunger gates. A characteristic drop at 0 bias indicates coherent tunneling of Cooper pairs, called a supercurrent, which breaks down at the critical current  $I_C$ . The residual resistance of  $\sim 1.5\text{ k}\Omega$  is larger than the expected fridge line resistance of  $550\ \Omega$  and is attributed to noise broadening the transport features. Another strong feature is a sharp increase in differential resistance, forming two peaks at symmetrical bias values. This is tentatively attributed to the heterogeneous nature of the superconducting film, namely the non-planarity of the evaporated film following the

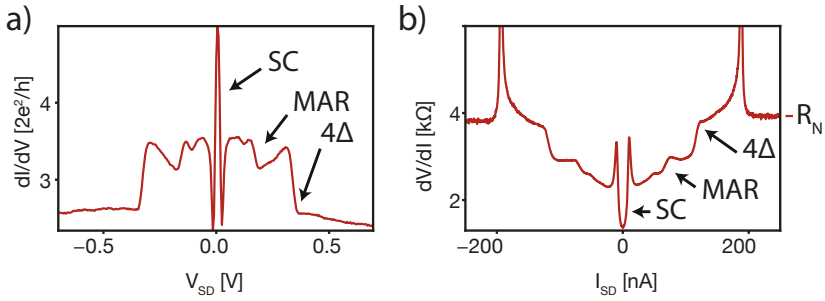


**Figure 5.3 Josephson junction features** on sample B. The labels denote the supercurrent SC, multiple Andreev reflections MAR and the  $4\Delta$  enhanced conductance. **a)** Differential conductance as a function of source drain voltage bias. **b)** Differential resistance as a function of current source drain bias.

nanowire geometry. More precisely, the peak occurs at the critical current of this parasitic junction.

A rough estimation allows a conversion from the voltage biased conductance values of fig 5.3 a) to the critical current, which can be evaluated by integrating the conductance in the 0 bias peak, yielding in this case a critical current  $I_C \sim 11.3$  nA. This number is consistent with values extracted from the current-biased measurements.

### 5.2.1 Magnetic field dependence

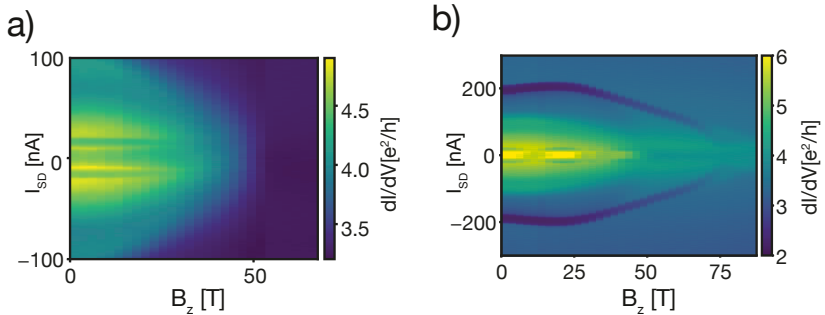


**Figure 5.4 Quenching the superconductor.** Conductance as a function of current bias and out-of-plane magnetic field strength for samples A (a) and B (b).

In order to further investigate the superconducting properties of the junction, we now consider the conductance as a function of current bias and of an out-of-plane magnetic field, shown in fig 5.4 a) for sample A and for sample B b), for zero plunger gates. We first note the expected closing of the superconducting gap at around 50 mT, a value in line with other measurements of thin-film aluminum deposited using the same evaporator. Interestingly, the critical current remains constant in both samples up to the superconducting-to-normal transition.

On the other hand, sample B presents a richer set of features: we first note weak ( $\sim 10\%$ ) oscillations reminiscent of a current-phase relation of a SQUID. The oscillation period of 20 mT would correspond to an area of  $0.1 \text{ } \mu\text{m}^2$ , a value exceeding the geometric area between the wires ( $40\text{nm} \times 230\text{nm} = 0.01 \text{ } \mu\text{m}^2$ ). The difference could be tentatively explained by a combination of the focusing of the magnetic field expelled from the superconductor, and the finite penetration length of the field into the superconductor. We also note that the dips in resistance at  $\pm 200 \text{ nA}$  quench at a larger critical field of  $\sim 90 \text{ mT}$ , compared to the 50 mT at which the supercurrent vanishes. This dip in the critical current could be explained by a weak link in a part of the superconductor with a different geometry, and thus a different critical current value.

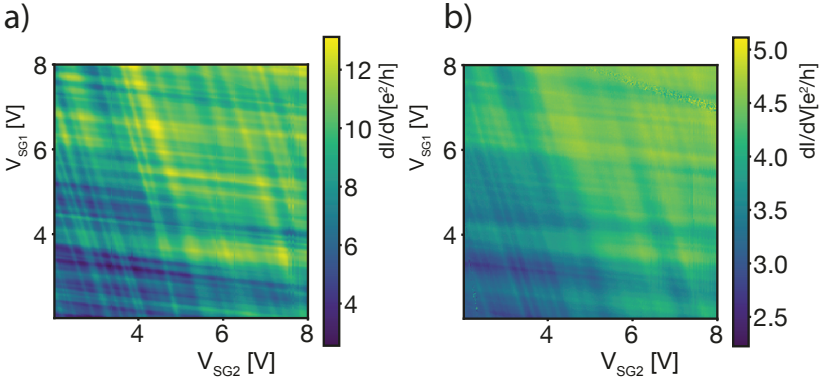


**Figure 5.5 Narrowing of features in the superconducting state in sample B. a)** Differential conductance as a function of sidegates in the superconducting state. **b)** Conductance map with the same parameters in the normal state when 200 mT are applied out of plane.

### 5.2.2 Comparing conductance in the N and S states

Fig 5.5 displays a comparison between 0-bias conductance in the normal (left, 200 mT applied out-of-plane) and superconducting states. We note a clear sharpening of features, and conductance enhancement. Although the broad features are strikingly similar, it is important to keep in mind the different nature of the transport processes. In the normal state, we recognize dot-like resonances. In the superconducting state, the 0-bias signal we see is actually the superconducting 0-bias peak of the supercurrent, i.e. direct tunnelling of Cooper pairs through the junction.

In the left figure, the metallic nature of the source and drain contacts causes the device layout to be identical to the normal state conductance maps of the last chapter, although a key difference is noteworthy: in the previous chapter, the *in-situ* grown shell offers a pristine epitaxial lattice-matched interface on one hand and an ex-situ evaporation on the other, which leads us to expect an asymmetric transparency of the contacts. In the device considered here, the source and drain contacts are fabricated in the same step and are expected to be identical.

### 5.3 Supercurrents

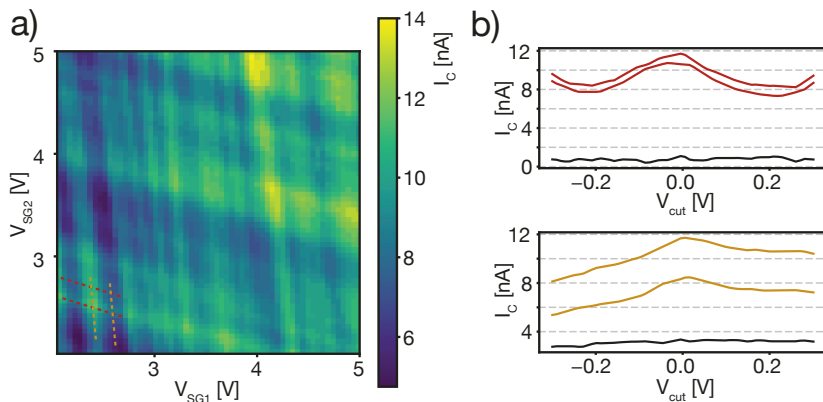


**Figure 5.6 Absence of non-local critical current** a) Critical current mapped as a function of plunger sidegates. b) Selected cuts, with the difference plotted in black, indicating no additional current when resonances attributed to the individual wires cross.

We now consider the critical current  $I_C$  of the Josephson junction. In a per-

fect experimental setting, extracting the critical current from a current-biased measurement and considering the 0-bias conductance in a voltage-biased measurement should yield similar results, assuming the broadening of the 0-bias peak is constant. However, the applied bias voltage slightly differs from the actual source-drain bias voltage, as evidenced by a superconducting peak slightly shifted from 0, typically by a few microvolts.

In order to record the critical supercurrent, traces of differential resistance versus bias current were recorded for every point, and the peak-to-peak distance divided by 2 is then plotted as a function of plunger gates, as can be seen in fig 5.6 a), with selected cuts displayed in b). Cuts were taken along resonances attributed to both wires, both on- and off resonance. The difference between the on and off-resonant cuts is plotted in black, showing no additional current when crossing a resonance from the other wire, indicating the absence of a non-local transport process.

### 5.3.1 Discussion

In contrast, a report from a similar experiment [126] shows a supercurrent enhancement of 57.3% when overlapping the first conduction channels. A key difference to the device investigated here is the junction length, which in our case is  $\sim 230$  nm compared to the much shorter  $\sim 30$  nm of the report. Interestingly, the supercurrent values reported for single-wire conductance are similar to the values we observe, indicating similar transparencies for both devices. We attribute the absence of coherent non-local transport in our work to the loss of coherence in the much longer Josephson junction. Indeed, the phase coherence length of electrons in InAs wires has been reported by [127] [128] to be in the  $\sim 50 - 150$  nm range. Our results are in agreement with the requirement that such non-local supercurrents demand coherent transport of the individual Cooper pairs through the junction; the presence of the supercurrent merely indicates an overlap between the superconducting macroscopic wave function of the proximitized wire's region. Furthermore, one requires coherence not only spanning the 230 nm junction, but also through the contact region where defects add an additional source of decoherence: the two electrons involved in the non-local Josephson process must not lose coherence to each other. Additionally, flux noise in the junction adds a source of decoherence. This is minimized in the device reported on in [126] by a junction-covering top gate.

In the next chapter, a device with a similar configuration but with *in-situ* epitaxial aluminum was measured. As it will be discussed, the analysis of the critical current did yield a similar absence of non-local transport.



## 6 Quasiparticle trapping in a S-N-S junction

---

*Lorsqu'une question soulève des opinions violemment contradictoires, on peut assurer qu'elle appartient au domaine de la croyance et non à celui de la connaissance.<sup>1</sup>*

- Voltaire

---

<sup>1</sup>If a question sparks violently contradicting opinions, one can be sure that it belongs to the realm of beliefs, and not that of knowledge.

## 6.1 Introduction

In the BCS picture of superconductivity, electrons form Cooper pairs which then condensate into a macroscopic wavefunction. The only allowed transport process through a semiconducting weak link and within the energy gap involves either the co-tunnelling of two electrons through a quantum dot state or an Andreev reflection. Tunnelling spectroscopy of the density of states reveals the superconducting gap as an absence of available states. As already discussed in chapter 3, unless the aluminum is evaporated *in-situ*, yielding a pristine interface between the superconductor and the nanowire, spectroscopy measurements usually reveal a *soft gap*, i.e. conduction in the forbidden energy range. The current in the gap arises from the excitation of quasiparticles. Theoretical modelling presented in [129] attributes the microscopic origin of these quasiparticles to impurity states resulting from the fabrication process, in our case most likely during oxide removal.

These quasiparticles enable single-electron tunnelling processes that break the coherence of the superconductor. In the case of a Coulomb island, a building block of the theorized Majorana modes, single electron processes change the parity and therefore poison the island and its hosted topological states [115]. This concern led to a quasiparticle filter device being designed and reported in [114].

Interest in quasiparticles and their control predates topological nanowire research. Indeed, quasiparticles are a major limiting factor on the performance of mesoscopic devices. In superconducting qubits, quasiparticles interact with the phase degree of freedom and provide a parasitic channel for the qubit relaxation [130, 131]. In Cooper pair pumps, quasiparticles lead to counting errors and limit the accuracy of the current-frequency relation [132]. While advanced processing techniques reduce quasiparticle generation, their excitation cannot be fully inhibited. Fortunately, the mobile nature of quasiparticles allows for another strategy, their trapping, confining them to a region of the superconductor far from the Josephson junction.

Although the samples presented in this chapter feature an *in-situ* evaporated shell, our data shows they do not present an ideal Josephson junction behaviour at 0 magnetic field. Strikingly, under the application of a magnetic field in the order of only  $\sim 30$  mT, a dramatic increase of the critical current is observed. In the more extreme cases the supercurrent is completely absent at 0 field and reaches a value of  $\sim 6nA$  at 15 mT. We tentatively attribute this enhancement to trapping of quasiparticles improving the coherence of the junction.

## 6.2 Device

The devices were fabricated from grown InAs double nanowires, with a 20nm *in-situ* evaporated aluminum shell. The shell was shadowed during *in-situ* alu-

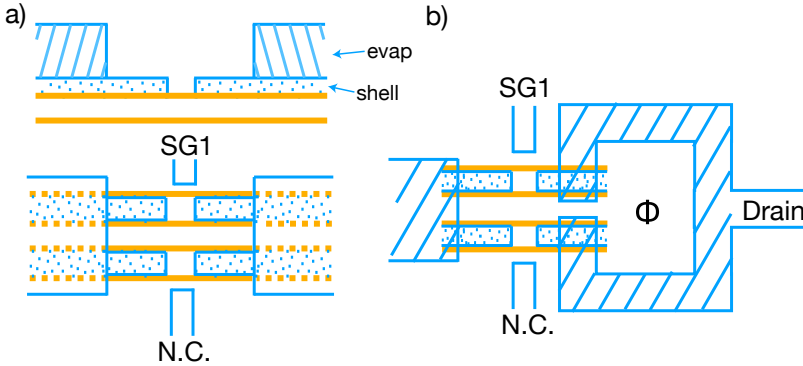


**Figure 6.1** Schematic representation of devices A (a) and B (b).

minimum evaporation by wires, such as to create a thin slit of  $\sim 100$  nm, thus creating a weak-link between two shell halves in which Josephson physics are expected. The fabricated devices are schematically shown in fig. 6.1. Additional aluminum was evaporated on the shell in order to insure good contact between the shells of both wires. Sample A follows a similar contact layout as the device presented in the previous chapter: common source and drain contacts for both wires and two sidegates. Unfortunately, an electrical leak shorts the backgate to the drain, and a single sidegate enables the control of the chemical potential of the junction, the other sidegate being inoperable. Sample B was designed to include a flux loop in the drain contact. Unfortunately the lift off of the metal enclosed by the loop was unsuccessful, effectively shorting the contact of both wires. Source and drain contacts, as well as the sidegates, were fabricated using a 100 nm thick evaporated aluminum in our UHV system following oxide removal by argon milling. Measurements will focus on sample B, owing to the better control offered by operating the plunger backgate. It is however important to note that since we observe qualitatively similar quasiparticle trapping behaviour in sample A, we can exclude impurities resulting from the unsuccessful lift-off in sample B as being the source of the observed phenomena.

### 6.3 Normal state characterization

Following the procedure used in the previous chapters, we first characterise our junction in the normal state, obtained by the application of a 200 mT out-of-plane magnetic field. A gate-gate map of the differential conductance

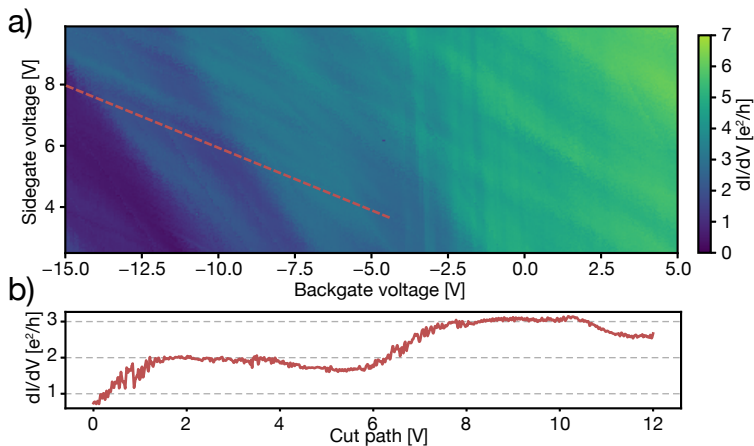


**Figure 6.2 Normal state conductance** a) Conductance as a function of plunger side- and backgate under an out-of-plane magnetic field of 200 mT. b) Cross-section of a) for SG at -6V

for sample B is provided in fig. 6.2 a). We recognise the characteristic double-wire pattern of resonances with two sets of slopes mirroring the lever arm ratio of the side- and backgate to both wires. The vertical lines are attributed to charging of defects, as the effect is fully controlled by the backgate and independent of the sidegate setting. As it can be seen in a cross-section of the gate-gate map at a sidegate voltage, shown in fig 6.2 b), we observe clear conductance plateaus at  $2e^2/h$  and  $3e^2/h$ .

### Gate-Gate map in the superconducting state

The gate-gate map of the same device in the same gate parameter range in the superconducting state is shown in fig. 6.3 a). As expected, we note the narrowing of features compared to the normal state. The plateaus are less pronounced, some regions of uniform conductance are suppressed. Interestingly, setting the field at 20 mT yields a marked enhancement in conductance, shown in fig. 6.3 b), which will be discussed below.

## 6.4 Josephson physics

We now consider a current-biased measurement of the junction as a function of plunger backgate, shown in figure 6.4 a). As we increase the backgate voltage, the normal state resistance decreases and a supercurrent appears, as shown by

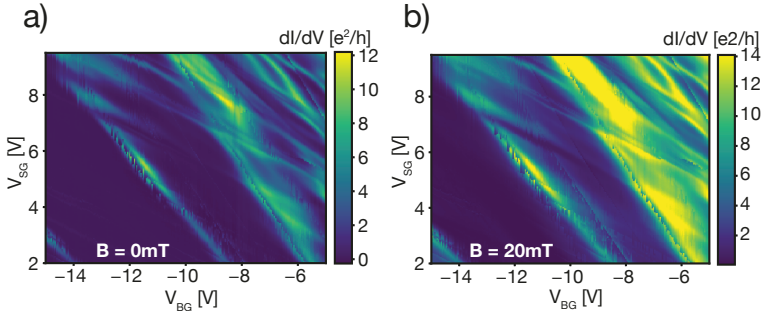


**Figure 6.3** Conductance map in the superconducting state a) Conductance as a function of plunger side- and backgate at 0 magnetic field. b) Conductance as a function of plunger side- and backgate for a magnetic field strength of 20 mT

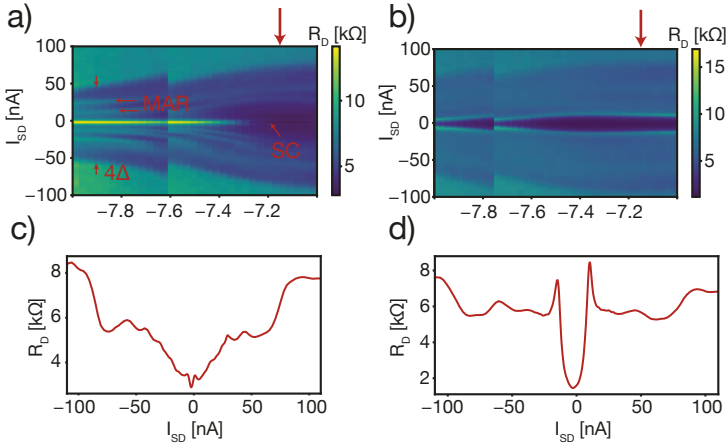


**Figure 6.4** a) Differential resistance as a function of current bias and plunger backgate at  $B = 0$  mT. b) Differential resistance as a function of current bias and plunger backgate at  $B = 20$  mT. c) and d) Cuts at an identical plunger backgate voltage of a) and b) respectively.

a cut in figure 6.4 c). Additionally, we recognize a  $\sim 25\%$  reduced resistance in the  $\pm 2\Delta$  region and traces of multiple Andreev reflection (MAR). Applying a 20 mT out-of-plane magnetic field enhances the supercurrent from  $\sim 1.25nA$  to  $\sim 9nA$  and features associated to the superconducting junction become more distinct. As an indicator of the junction quality we now evaluate the  $R_N I_C$  product of our junction, as was introduced in section 2.4. Using the data from fig 6.4, we obtain  $\eta_{0mT} \simeq 4.5\%$  and  $\eta_{20mT} \simeq 35.2\%$ . The microscopic origin of this improvement, which we attribute to magnetically-driven trapping of the quasiparticles, will be discussed at the end of this chapter.

## 6.5 Andreev bound states in the junction

Voltage-biased measurements, which present the advantage of proving a direct energy scale, are especially relevant for the analysis of Andreev bound states and multiple Andreev reflections.

In figure 6.5, the sidegate and bias were swept in the same sidegate range for magnetic fields of 0, 20, and 200 mT, with the junction respectively in the superconducting state, in superconducting state with quasiparticle filtering, and in the normal state. We first note the appearance of a 0 bias conductance anomaly, the super-current, at 20 mT, denoted by the abbreviation SC in the figure. We also observe Coulomb diamonds for low sidegate voltage values in the normal state (c) where  $B = 200$  mT), which result in Andreev bound states in the superconducting state, denoted by ABS in the figure. At higher sidegate voltages, where the junction is not purely in the dot regime, as evidenced by the presence of a conductance background and the washing out on resonances in the normal state, we see multiple Andreev Resonances (MAR), which can be distinguished from Andreev bound states by the fixed  $2\Delta/n$  bias value of the resonances. Arrows are shown at  $2\Delta/n$ ,  $n = 1, 2, 3, 4$  bias values for a  $\Delta = 205 \mu V$ , proving these resonances result from multiple Andreev reflections. As it can be seen in the conductance cross-sections shown in fig. 6.5, the  $n = 3, 4$  MAR resonances become indistinguishable as conductance is enhanced. A reference cross-section in yellow, taken at  $-8.55$  V, is used to determine  $\Delta_J \simeq 205 \mu V$ . Theoretical modelling reported in [92], which follows the finding that multiple Andreev reflections manifest as either dips or peaks in conductance, already reported in [89], leads us to estimate the transparency of the reference cross-section as being  $\tau < 0.3$ . This low transmissivity with the Coulomb diamonds observed in the normal state conductance indicates the formation of dots. In contrast, cross sections taken at  $-3.7$  V show multiple Andreev resonances consistent with a transmissivity  $\tau > 0.8$ . The applied voltage is plotted, the actual voltage drop over the junction is smaller owing to parasitic resistance in series with the junction.

Overlapping of Andreev bound states attributed to different wires were in-

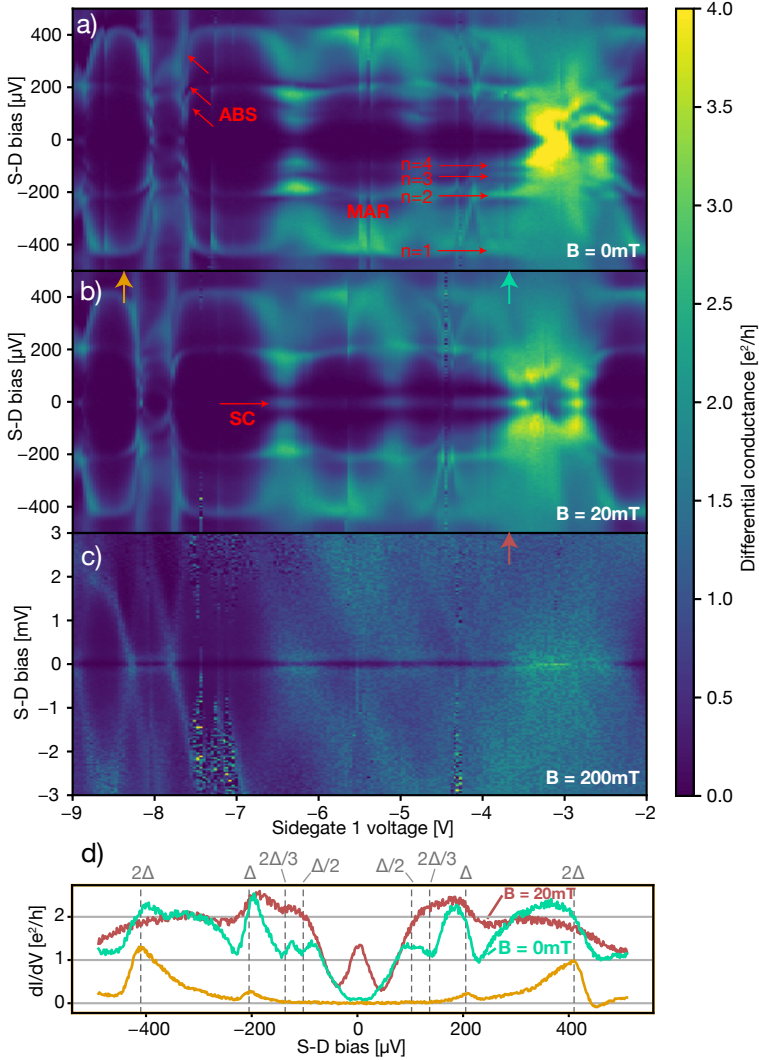


**Figure 6.5** Andreev bound states and multiple Andreev reflections in sample B at  $V_{\text{BG}} = -15\text{V}$ . Differential conductance as a function of bias for different values of the out-of-plane magnetic field:  $B = 0\text{ mT}$  in **a**),  $B = 20\text{ mT}$  in **b**),  $B = 200\text{ mT}$  in **c**). **d**) Selected cross-sections of **a**) and **b**) at  $V_{\text{SG}} = -3.7, -8.55$ .

vestigated following a similar method to section 4.7, but no anti-crossings could be found.

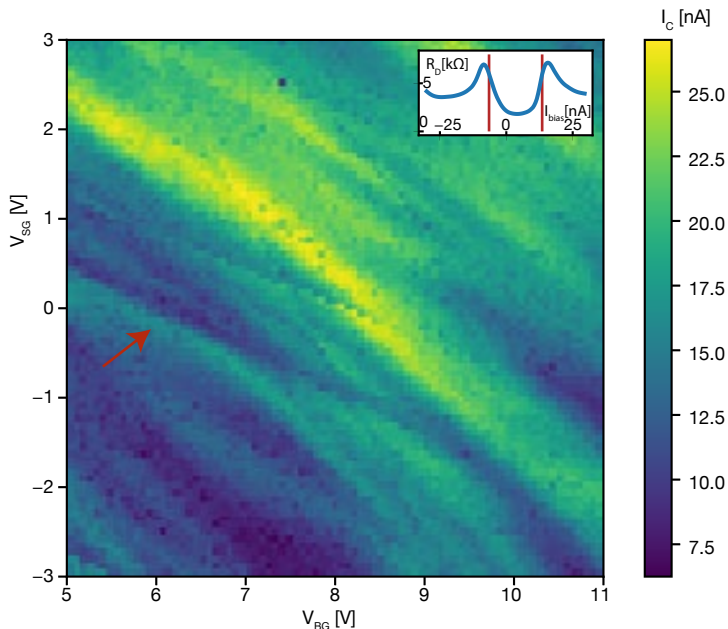


**Figure 6.6 Absence of non-local transport evidence in critical current** in sample B. Critical current as a function of sidegate and backgate voltages. Inset: the critical current is extracted from traces of differential resistance measurement in current bias, determining the inflection point of spline-interpolated data (spline shown), inflection points denoted by the red vertical lines.

## 6.6 Mapping the critical current

Repeating the procedure from chapter 5, we investigate the local nature of the Josephson current. Critical current as a function of plunger backgate and sidegate is plotted in fig. 6.6, with the critical current extraction procedure shown in the inset. Despite a shorter junction, *in-situ* contacts and conductance plateaus hinting at ballistic transport, we do not observe a non-local current. Five similar maps were measured around (backgate,sidegate) coordinates of

$(-18,0)$ ,  $(0,0)$ ,  $(-15,0)$ ,  $(8,0)$ , shown, and  $(-6,5)$ , covering a large parameter range. These points were selected for normal state conductance showing resonances attributed to both wires. Furthermore, the resonance denoted by an arrow inflects, following one slope then another, indicating a state with a wavefunction hybridising both wires, similar to the anti-crossing seen in sec. 4.9.

Our interpretation is the same as the one reached in chapter 5. Despite the ballistic nature of the transport process, the absence of a non-local transport process is attributed to loss of coherence through the junction. It is important to note that the measured junction length only reflects the gap between the source and drain metallisation, but the electrical contact interface possibly extends 100s of nanometers under the contact leads.

## 6.7 Quasiparticle trapping

As shown in the preceding data, applying a 20 mT magnetic field dramatically improves the critical field of the Josephson junction. Two recent reports from the groups of Giazotti and Tarucha [133] [134] show strikingly similar enhancements in the critical current of single InAs nanowire Josephson junctions. The former attributes the enhancement to "a magnetically driven zero-energy parity crossing of Andreev levels in the junction which is expected to occur for magnetic fields applied perpendicularly to the wire axis." Throughout our experiments with similar nanowires, evidence for a topological phase transition has remained elusive, which is consistent with the attribution of the infamous 0-bias peak to topologically trivial Andreev bound states [34]. We will thus not focus on an explanation involving a non-trivial topological state. Interestingly, the enhancement occurs at 20 mT, which is comparable to the 15 mT we observe.

The latter report attributes the enhancement to quasiparticle trapping in vortices of the source and drain leads, in the vortex cores, the superconducting pair potential is broken, allowing single-electron processes and acting as a trapping potential for quasiparticles.

Although vortices do not form in bulk type I superconductors [36], they have been reported in thin films made of type I superconductors, e.g. a 30 nm thick aluminum film [135, 136].

Both reports only observe trapping for out-of-plane magnetic fields. We investigated the dependence of the trapping transition field on the direction and strength of the magnetic field. In contrast to the reports, we observe trapping for all field directions, with the field at which the critical current is enhanced depending on the direction of the magnetic field. Fig. 6.7 a)-c) shows the differential resistance as a function of bias for all three magnetic field directions: out-of-plane, parallel to the wires and perpendicular to the wires. The features are identical, except for the field strength at which the

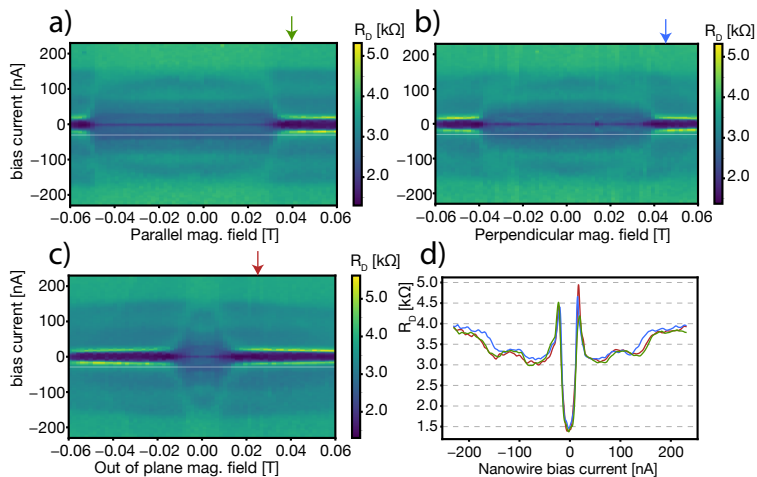


**Figure 6.7 Anisotropy of the critical current with trapped quasiparticles** in sample B. Differential resistance as a function of current bias and magnetic field strength for 3 different field angles: parallel to the wire shell in **a**), perpendicular in **b**) and out of plane in **c**). The angle of the shell was determined by scanning the magnetic field angle at 300 mT, where the superconducting shell quenches for non-parallel fields. **d**) cross-sections of a-c) after the trapping transition.

trapping occurs:  $\sim 45$  mT for parallel field,  $\sim 35$  mT for perpendicular field and  $\sim 15$  mT for out-of-plane field. This fundamental difference has a serious consequence: vortices have been shown to be expelled from the narrow superconducting lead or shell of width  $W$  for a magnetic field below  $B_0 = \phi_0/W^2$  [137] [136] [138], with  $\phi_0$  the magnetic flux quantum. In the report from Tarucha, this poses no issue, since a large source and drain contact geometry (estimated to be  $\sim 1 \mu\text{m}$  large from their micrograph) allows for hosting vortices in magnetic fields with a strength greater than 2 mT. In our devices however, when the magnetic field is oriented in the sample plane, the thickness of the evaporated leads is  $\sim 100\text{nm}$ , excluding the presence of vortices for magnetic field strengths under 200 mT. We thus consider the presence of quasiparticle-trapping vortices as being unlikely.

In the absence of normal metal in the vicinity of the junction (the nearest gold from the base structure is  $> 100 \mu\text{m}$  away), the remaining candidate is considered to explain the observed phenomenon: that regions of the superconductor with lower gap size traps quasiparticles.

### Gap size engineering

The Gap size  $\Delta$  is a property of the superconductor that can vary over distances beyond the coherence length: although its value is measured to be 390 meV for bulk aluminum, variations in material quality [139], film geometry [140] as well as experimental parameters (foremost temperature and magnetic field) all locally influence the gap size  $\Delta^*(r)$ . Gap size engineering by introduction of oxygen during the evaporation process has been reported in [139]. Used to stabilize a Cooper pair transistor, the authors observe that defects in aluminum *increase* the critical temperature of the superconductor and thus the gap size.

In our samples, the superconducting source and drain contacts are of heterogeneous nature: The evaporated aluminum is deposited at a higher pressure and temperature than the epitaxial aluminum of the nanowire shell, and thus it is to be expected that the gap size be slightly different: the presence of a background pressure of oxygen at  $5 \times 10^{-9}$  bar is likely, and, consistent with the report wherein oxygen is introduced in the evaporation chamber [139], we expect the gap size  $\Delta_{\text{evap}} > \Delta_{\text{in-situ}}$ . On the other hand, comparing data from chapters 4 and 5 shows an out-of-plane critical field difference,  $\sim 50$  mT for evaporated aluminum and  $\sim 200$  mT for the in-situ grown shell. The consequences of these different behaviours are sketched in fig. 6.8. In a) at 0 field, the gap of the shell is smaller than that of the evaporated aluminum. This has the consequence that the filter acts in *reverse*, actively trapping quasiparticles in the vicinity of the junction. This artificial deterioration of the junction is evidenced by the  $R_N I_C$  coefficient of 4.5% presented in section 6.4 and consistent with our observation of a critical current enhancement of 500%, compared

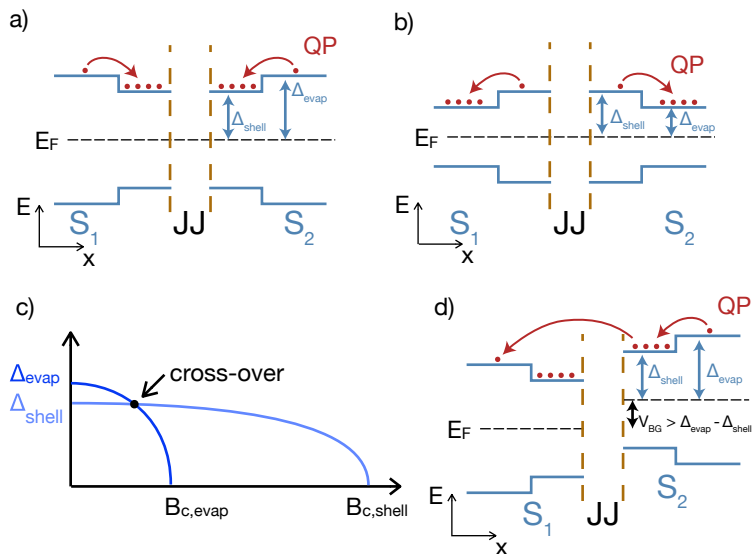


**Figure 6.8** Magnetically activated engineered gap quasiparticle filter in sample B. **a)** at  $B_{\text{out of plane}} = 0 \text{ mT}$ . **b)** at  $B_{\text{out of plane}} = 20 \text{ mT}$ . **c)** Gap sizes as a function of field. The critical field of the evaporated shell is lower than the *in-situ* shell due to the different geometry. The 0-field gap size difference can be explained by material quality. **d)** Junction under a bias  $V_{\text{SD}} > \Delta_{\text{evap}} - \Delta_{\text{shell}}$ , highlighting an issue with this interpretation.

to the 100% – 200% ratio roughly estimated based on the figures in [133] and [134].

When the magnetic field is applied, the evaporated aluminum quenches at lower critical field values than the shell, as sketched in c). When the field is greater than the cross-over point, as sketched in b), the smaller gap size of the region further from the junction actively traps quasiparticles, resulting in an enhanced critical current.

### Mixed state of the superconductor

Attributing the trapping of the quasiparticles to a local narrowing of the superconducting gap can be tested by considering the effect of a finite voltage biased on the trapping mechanism. As it can be seen in fig. 6.7 a-c), the transition to the trapped state does not occur at the same magnetic field value for a finite bias current. This bias induced transition appears even more clearly when considering voltage-biased differential conductance as a function of source-drain bias and out-of-plane magnetic field, shown in fig. 6.9. The quasiparticle trapping transition appears both as an enhancement of the critical current, and as a strong change in the multiple Andreev reflection resonances within the  $\pm 2\Delta$  range. The multiple Andreev reflections appear to be more distinct in the presence of quasiparticles near the junction, whereas the dips in conductance become weaker when those quasiparticles are trapped. The value of the differential conductance also changes, decreasing in the  $\pm 2\Delta$  range for trapped quasiparticles. Pertinent to the origin of the trapping, this transition does not occur at a fixed magnetic field value, but a roughly linear relation between the transition bias voltage and the magnetic field strength is observed.

Our gap size engineering hypothesis fails to convincingly explain this major feature: one would expect the necessary voltage bias to tunnel quasiparticles to the bigger gap to be  $\Delta_{\text{evap}} - \Delta_{\text{shell}}$  (possible mechanism is sketched in fig. 6.8), whereas the bias voltage applied in this case goes up to  $2\Delta$ .

Another hypothesis for the trapping mechanism considers the phenomenology of a Type I superconductor under the application of a magnetic field. As current flows to uphold the Meissner effect, regions of the superconductor transition to the normal state [141, 36], where unbound electrons are available to trap quasiparticles. Sharp features in the outline of a superconductor require a larger current density to uphold the Meissner effect and thus transition at lower fields.

For magnetic field strength values lower than but near the transition, when a finite bias is applied, a dissipative current flows. This is evidenced by multiple Andreev reflections, wherein each electron dissipate an energy of  $eV_{SD}$ . This heating of the superconductor near the junction with a power  $IV_{SD}$  then leads to regions of the superconductor transitioning to the normal state and trapping quasiparticles. This hypothesis qualitatively explains the quasi linear relation

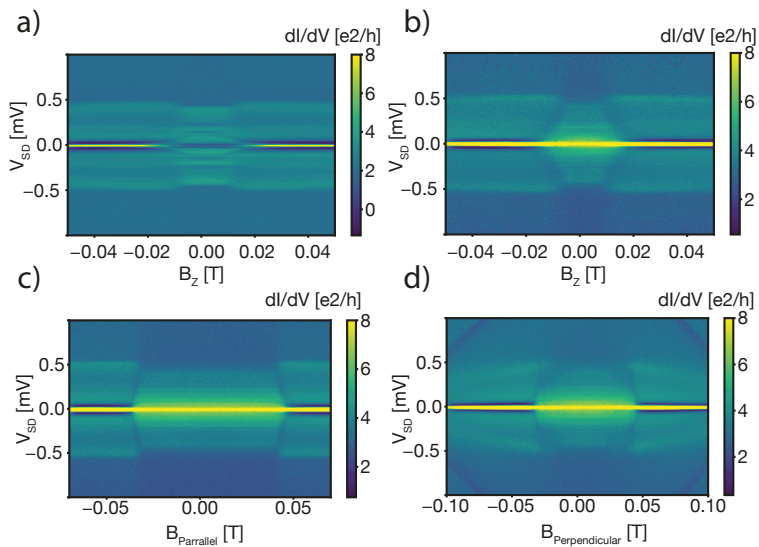


**Figure 6.9 Quasiparticle trapping in different field directions.** Conductance as a function of bias and out of plane magnetic field, for (backgate, sidegate) points **a**) (12,7) and **b**) (-7,8). At the latter point, for magnetic fields parallel to the wire **c**) and perpendicular **d**).

between bias and trapping transition field strength seen in 6.9, although the observed slope depends on gate voltage settings and field orientation.

By nature, a superconductor in the mixed state is an excellent quasiparticle trap, since the corners of the contact, due to their sharpness, are expected to transition to the normal state at the lowest magnetic field value, providing a quasiparticle trap in the direct vicinity of the junction.

## 6.8 Discussion

We observe a dramatic enhancement to the critical current, which we attribute to reversible quasiparticle trapping by magnetically controlled gap size engineering in our double nanowire junction. With our quasiparticle filter activated, we characterised our junction to be of high transparency, evidenced by both plateaus in conductance and conductance enhancement in the  $2\Delta$  region, with multiple Andreev reflections suggesting a near unity  $\tau > 0.8$ . Although no evidence for non-local transport could be found, as well as no anti-crossings of Andreev bound states were observed, the  $\eta = R_N I_C / e\Delta$  coefficient of 37.3% is in line with other experimental reports [87].

### Consequences for previous experiments

At this point, the "elephant in the room" is the following question: why do those quasiparticles not play a similar role in the experiments shown in chapters 4 and 5?

The devices probed in chapter 4 might have benefited from a coincidence: one of the goal of the experiments was the characterisation of the *in-situ* shells of the wires, and in order to do so, care was taken to not evaporate any additional superconductors. This had the consequence of providing the shell with a perfect quasiparticle trap: the evaporated Pd normal contact, a mere  $\sim 800nm$  from the N-S junction. Evidence of this trapping is provided by the *hard gap* observed in sec 4.4.

Chapter 5 presents a more perplexing puzzle: the device probed there is, functionally, identical to the one probed in this chapter. Two differences are especially relevant: the heterogeneous nature of the superconductor, and the different thickness of the shell closest to the junction. Both can explain the different behaviour of the devices: the thinner shell would transition to the mixed state at a much lower field than the thicker evaporated shell, and the heterogeneous superconductor acting as both a quasiparticle trap and multiplier.

The consequences of the inverse quasiparticle trapping (i.e. trapping quasiparticles near the junction instead of far away) also has an unfortunate consequence for regions of a semiconductor proximitized by a superconductor: they

have, per definition, a smaller gap size, and thus we would expect them to attract quasiparticles.

In our samples, a direct measurement of the  $\Delta_{\text{evap}}$  is not possible. Further work could design a separate N-S structure in order to do spectroscopy of the gap of our evaporated aluminum. The reverse operation of our trap has important consequences for the design of mesoscale superconducting hybrids: great care has to be taken that the superconducting gap not be smaller near the active part of any device: although in our case our design allows for an inversion of gap sizes by the magnetic field, other design geometries might not. Another possibility for future work would be to design a device in which vortices and gap size engineering compete for quasiparticle trapping: insight could be gained in the strength of such mechanisms.

# 7 Conclusion

---

*There is nothing like looking if you want to find something. You certainly usually find something, if you look, but it is not always quite the something you were after.*

- J.R.R Tolkien

We set out on this project with the ambitious goal of realising a parafermion-hosting double nanowire device. Working towards this goal led us to develop fabrication techniques and yielded measurements that allowed the investigation of multiple phenomena of a double wire semiconductor-superconductor hybrids, even if the final goal remained elusive.

We perfected the nanowire pair fabrication workflow, redesigning the base structure, coding and implementing a tool for faster nanowire location, reliably achieving  $\sim 2-3$  working devices per cooldown. We were fortunate to collaborate with the Nygard group working with their advanced nanowire pair growth technology. This allowed a substantial improvement in the semiconductor-superconductor interface for our double nanowire devices. Their shadowed aluminum evaporation technique permitted us to design N-S and S-N-S junctions with no required etching, yielding comparatively transparent pristine junctions, as demonstrated in our data by conduction plateaus and a gap of hardness  $> 100$ .

These devices enabled us to probe the fundamental physics at play in these heterostructures, starting by designing a double wire N-S junction. Surprisingly, even though our characterisations showed the good quality of our contacts, with coupling  $\Gamma_S$  fitted to be of the order of  $0.2E_C$  in our device, a gap hardness shown to be as high as  $> 100$ , evidence for Cooper pair splitting or crossed Andreev reflection remained elusive. The former contrasting with reports using similar InAs wires [104, 123]. The main difference being the individual contacting of the latter reports, resulting in the larger source and drain coupling rates in our devices. We characterised this difference in coupling by considering the height of resonance peaks, which reflects the ratio  $(\Gamma_S\Gamma_D)/(\Gamma_S^2 + \Gamma_D^2)$ : they are around  $\sim 0.25 - 1e^2/h$  in our case and  $< 1 \times 10^{-2}$  for the Cooper pair splitter reports. We also investigated the behaviour of

Andreev bound states, overlapping bound states attributed to separate wire segments, and found no indication of the hybridisation of the bound states on different wires.

Although further investigation is required to understand why the hybridisation of Andreev bound states remained elusive, one could speculate that the high transparency of the junctions reduces the lifetime of a particle in the wire segments to about 6 picoseconds, thus reducing the interaction energy scale below observable values.

Then, we moved on to investigating Josephson junctions, where we characterized the  $R_N I_C$  coefficient to be  $\sim 35\%e\Delta$ , compared to the theoretical maximum of  $205\%e\Delta$ . Our value is close to a value obtained by a rough estimate based on the data presented in [126]. However, the observation of a non-local current remained elusive in our case, which we attribute to decoherence in our 280 nm long wire segments. In addition to designing a significantly shorter (30 nm) junction, the experiment reported in [126] employed a metallic plunger gate electrode that covered their junction, screening the electromagnetic field in the proximity of the junction, reducing magnetic flux noise.

In a second series of measurements, we also analysed Andreev bound states and multiple Andreev reflections in our Josephson junctions. We found that applying a relatively small magnetic field of 20 mT dramatically increases the critical current by up to 500%. We attribute this phenomenon to quasiparticle trapping and propose two competing explanations, gap size engineering and a type I superconductor in the mixed state which could explain the observed phenomena.

The perplexing elusiveness in our experiments of any evidence for non-local currents, Cooper pair splitting, or any coupling between states in the wire segments by the superconductor remains an interesting mystery after these five years of research.

One naturally wants to ask why? In all the characterisations we did, we found we have excellent coupling to the source and drain with  $\Gamma_S \sim 2meV$ , hard gaps  $G_N/G_S > 100$ , quasi-ballistic transport evidenced by plateaus. It would then seem unlikely that a fabrication issue would be the cause behind the absence of evidence for the aforementioned effects. We also varied the parameters available to us: wire diameter (40 nm - 110 nm), ex-situ and in-situ aluminum deposition, sulfur passivation and argon milling oxide removal and junction length.

It is interesting to think how it is possible that dot states which we characterise as being strongly coupled to the superconductor do not seem to interact with each other: resonances clearly attributed to separate wires cross, and if they anti-cross, they also do so in the presence of a magnetic field. Maybe it is a mistake to think of these resonances as states living in the wire segments: we actually found that they are much more strongly coupled (by a 5-10:1 factor) to the superconductor than the normal lead. The issue then might not be

---

that our samples were of bad quality, but on the contrary the coupling to the superconducting leads was too strong.

Indeed, the need for a pristine defect free interface between the superconductor and the nanowire spurred the development of the *in-situ* evaporation technology, yielding epitaxially matched interfaces between the aluminum and InAs nanowire. This ultimately gave us the devices presented in chapters 4 and 6. The goal of having well-defined states in the wire segments motivated us to shorten the junctions, effectively increasing the separation of the dot states in the energy spectrum. Ultimately, we have resonances from which we can conclude that the dot has a larger coupling  $\Gamma_S$  than the  $\Delta$  superconducting gap, meaning that most assumptions which are made in the physics describing quantum dots coupled to superconductors do not hold true.

Also, the states of electrons in a wire segment have extremely short lifetime, which might negatively impact their interaction strength with states from the adjacent segment. Thus, it might not be so surprising we were unable to resolve the effects we were after: in the desire to improve our devices, we might have inadvertently made the effect we were after harder to observe.

In the case of the non-local Josephson effect, we tentatively conclude that the absence of a non-local current is due to the sensibility of a double nanowire junction to flux noise, as well as the need for coherent transport of the electrons from one superconducting lead to the other, requiring extremely short junctions.

In conclusion, we set out to design a platform hosting exotic topological states, parafermions, and while this goal remains elusive, we gained insight into the phenomena of a double wire semiconductor superconductor hybrid. The surprising absence of expected phenomena highlights the need to sometimes take a step back, and be sure to understand the physics of the underlying systems before pursuing more elegant and sophisticated goals.



## Bibliography

- [1] G. E. Moore, “Cramming more components onto integrated circuits,” vol. 38, no. 8, p. 6, 1965.
- [2] D. A. Wharam *et al.*, “One-dimensional transport and the quantization of the ballistic resistance,” *Journal of Physics C: Solid State Physics*, vol. 21, no. 8, pp. L209–L214, Mar. 20, 1988, ISSN: 0022-3719. DOI: 10.1088/0022-3719/21/8/002. [Online]. Available: <https://iopscience.iop.org/article/10.1088/0022-3719/21/8/002> (visited on 10/29/2022).
- [3] B. J. van Wees *et al.*, “Quantized conductance of point contacts in a two-dimensional electron gas,” *Physical Review Letters*, vol. 60, no. 9, pp. 848–850, Feb. 29, 1988, ISSN: 0031-9007. DOI: 10.1103/PhysRevLett.60.848. [Online]. Available: <https://link.aps.org/doi/10.1103/PhysRevLett.60.848> (visited on 10/29/2022).
- [4] L. P. Kouwenhoven, C. M. Marcus, P. L. McEuen, S. Tarucha, and N. S. Wingreen, “ELECTRON TRANSPORT IN QUANTUM DOTS.,” *QUANTUM DOTS*, p. 110,
- [5] P. L. McEuen *et al.*, “Transport spectroscopy of a Coulomb island in the quantum Hall regime,” *Physical Review Letters*, vol. 66, no. 14, pp. 1926–1929, Apr. 8, 1991. DOI: 10.1103/PhysRevLett.66.1926. [Online]. Available: <https://link.aps.org/doi/10.1103/PhysRevLett.66.1926> (visited on 10/29/2022).
- [6] W. Lu and C. M. Lieber, “Semiconductor nanowires,” *Journal of Physics D: Applied Physics*, vol. 39, no. 21, R387, Oct. 2006, ISSN: 0022-3727. DOI: 10.1088/0022-3727/39/21/R01. [Online]. Available: <https://dx.doi.org/10.1088/0022-3727/39/21/R01> (visited on 10/30/2022).
- [7] Y. Cui, Z. Zhong, D. Wang, W. U. Wang, and C. M. Lieber, “High Performance Silicon Nanowire Field Effect Transistors,” *Nano Letters*, vol. 3, no. 2, pp. 149–152, Feb. 1, 2003, ISSN: 1530-6984. DOI: 10.1021/nl10258751. [Online]. Available: <https://doi.org/10.1021/nl10258751> (visited on 10/30/2022).

- [8] J. Bao, M. A. Zimmler, F. Capasso, X. Wang, and Z. F. Ren, “Broadband ZnO Single-Nanowire Light-Emitting Diode,” *Nano Letters*, vol. 6, no. 8, pp. 1719–1722, Aug. 1, 2006, ISSN: 1530-6984. DOI: 10.1021/nl061080t. [Online]. Available: <https://doi.org/10.1021/nl061080t> (visited on 10/30/2022).
- [9] E. C. Garnett, M. L. Brongersma, Y. Cui, and M. D. McGehee, “Nanowire Solar Cells,” *Annual Review of Materials Research*, vol. 41, no. 1, pp. 269–295, Aug. 4, 2011, ISSN: 1531-7331, 1545-4118. DOI: 10.1146/annurev-matsci-062910-100434. [Online]. Available: <https://www.annualreviews.org/doi/10.1146/annurev-matsci-062910-100434> (visited on 10/30/2022).
- [10] P. Offermans, M. Crego-Calama, and S. H. Brongersma, “Gas Detection with Vertical InAs Nanowire Arrays,” *Nano Letters*, vol. 10, no. 7, pp. 2412–2415, Jul. 14, 2010, ISSN: 1530-6984. DOI: 10.1021/nl1005405. [Online]. Available: <https://doi.org/10.1021/nl1005405> (visited on 10/30/2022).
- [11] T. Xu *et al.*, “Recent progress on infrared photodetectors based on InAs and InAsSb nanowires,” *Nanotechnology*, vol. 31, no. 29, p. 294 004, May 2020, ISSN: 0957-4484. DOI: 10.1088/1361-6528/ab8591. [Online]. Available: <https://dx.doi.org/10.1088/1361-6528/ab8591> (visited on 10/30/2022).
- [12] S. De Franceschi, L. Kouwenhoven, C. Schönenberger, and W. Wernsdorfer, “Hybrid superconductor–quantum dot devices,” *Nature Nanotechnology*, vol. 5, no. 10, pp. 703–711, 10 Oct. 2010, ISSN: 1748-3395. DOI: 10.1038/nnano.2010.173. [Online]. Available: <https://www.nature.com/articles/nnano.2010.173> (visited on 10/30/2022).
- [13] H. Kosaka, A. A. Kiselev, F. A. Baron, K. W. Kim, and E. Yablonovitch, “Electron g factor engineering in III-V semiconductors for quantum communications,” *Electronics Letters*, vol. 37, no. 7, pp. 464–465, Mar. 29, 2001, ISSN: 1350-911X. DOI: 10.1049/e1:20010314. [Online]. Available: [https://digital-library.theiet.org/content/journals/10.1049/e1\\_20010314](https://digital-library.theiet.org/content/journals/10.1049/e1_20010314) (visited on 10/30/2022).
- [14] S. A. Dayeh, D. P. R. Aplin, X. Zhou, P. K. L. Yu, E. T. Yu, and D. Wang, “High Electron Mobility InAs Nanowire Field-Effect Transistors,” *Small*, vol. 3, no. 2, pp. 326–332, 2007, ISSN: 1613-6829. DOI: 10.1002/smll.200600379. [Online]. Available: <https://onlinelibrary.wiley.com/doi/abs/10.1002/smll.200600379> (visited on 10/30/2022).

- [15] H. Xu *et al.*, “Defect-Free  $\langle 110 \rangle$  Zinc-Blende Structured InAs Nanowires Catalyzed by Palladium,” *Nano Letters*, vol. 12, no. 11, pp. 5744–5749, Nov. 14, 2012, ISSN: 1530-6984. DOI: 10.1021/nl303028u. [Online]. Available: <https://doi.org/10.1021/nl303028u> (visited on 10/30/2022).
- [16] R. P. Feynman, “Simulating physics with computers,” *International Journal of Theoretical Physics*, vol. 21, no. 6-7, pp. 467–488, Jun. 1982, ISSN: 0020-7748. DOI: 10.1007/BF02650179.
- [17] P. Shor, “Algorithms for quantum computation: Discrete logarithms and factoring,” in *Proceedings 35th Annual Symposium on Foundations of Computer Science*, Nov. 1994, pp. 124–134. DOI: 10.1109/SFCS.1994.365700.
- [18] M. A. Nielsen and I. L. Chuang, *Quantum Computation and Quantum Information*. Cambridge University Press, 2000.
- [19] *IBM quantum roadmap*. [Online]. Available: <https://www.ibm.com/quantum/roadmap>.
- [20] *National quantum initiative*. [Online]. Available: <https://www.quantum.gov/>.
- [21] *European quantum flagship*. [Online]. Available: <https://qt.eu/>.
- [22] A. Y. Kitaev, “Quantum computations: Algorithms and error correction,” *Russian Mathematical Surveys*, vol. 52, no. 6, pp. 1191–1249, Dec. 1997, ISSN: 0036-0279. DOI: 10.1070/RM1997v052n06ABEH002155.
- [23] D. Gottesman, *Opportunities and challenges in fault-tolerant quantum computation*, Oct. 2022. DOI: 10.48550/arXiv.2210.15844. arXiv: 2210.15844 [quant-ph].
- [24] A. Y. Kitaev, “Unpaired Majorana fermions in quantum wires,” *Physics-Uspekhi*, vol. 44, p. 131, 10S Oct. 2001, ISSN: 1063-7869. DOI: 10.1070/1063-7869/44/10S/S29. [Online]. Available: <https://dx.doi.org/10.1070/1063-7869/44/10S/S29> (visited on 11/10/2022).
- [25] A. Y. Kitaev, “Fault-tolerant quantum computation by anyons,” *Annals of Physics*, vol. 303, no. 1, pp. 2–30, Jan. 1, 2003, ISSN: 0003-4916. DOI: 10.1016/S0003-4916(02)00018-0. [Online]. Available: <https://www.sciencedirect.com/science/article/pii/S0003491602000180> (visited on 11/10/2022).
- [26] E. Majorana, “Teoria simmetrica dell’elettrone e del positrone,” *Il Nuovo Cimento (1924-1942)*, vol. 14, no. 4, p. 171, Sep. 21, 2008, ISSN: 1827-6121. DOI: 10.1007/BF02961314. [Online]. Available: <https://doi.org/10.1007/BF02961314> (visited on 10/31/2022).

- [27] J. Alicea, “New directions in the pursuit of Majorana fermions in solid state systems,” *Reports on Progress in Physics*, vol. 75, no. 7, p. 076 501, Jun. 2012, ISSN: 0034-4885. DOI: 10.1088/0034-4885/75/7/076501. [Online]. Available: <https://dx.doi.org/10.1088/0034-4885/75/7/076501> (visited on 10/30/2022).
- [28] V. Mourik, K. Zuo, S. M. Frolov, S. R. Plissard, E. P. A. M. Bakkers, and L. P. Kouwenhoven, “Signatures of Majorana Fermions in Hybrid Superconductor-Semiconductor Nanowire Devices,” *Science*, vol. 336, no. 6084, pp. 1003–1007, May 25, 2012. DOI: 10.1126/science.1222360. [Online]. Available: <https://www.science.org/doi/10.1126/science.1222360> (visited on 10/31/2022).
- [29] J. Klinovaja and D. Loss, “Time-reversal invariant parafermions in interacting Rashba nanowires,” *Physical Review B*, vol. 90, no. 4, p. 045 118, Jul. 17, 2014, ISSN: 1098-0121, 1550-235X. DOI: 10.1103/PhysRevB.90.045118. [Online]. Available: <https://link.aps.org/doi/10.1103/PhysRevB.90.045118> (visited on 11/08/2022).
- [30] E. J. H. Lee, X. Jiang, M. Houzet, R. Aguado, C. M. Lieber, and S. De Franceschi, “Spin-resolved Andreev levels and parity crossings in hybrid superconductor–semiconductor nanostructures,” *Nature Nanotechnology*, vol. 9, no. 1, pp. 79–84, 1 Jan. 2014, ISSN: 1748-3395. DOI: 10.1038/nnano.2013.267. [Online]. Available: <https://www.nature.com/articles/nnano.2013.267> (visited on 11/10/2022).
- [31] H. Zhang *et al.*, “RETRACTED ARTICLE: Quantized Majorana conductance,” *Nature*, vol. 556, no. 7699, pp. 74–79, 7699 Apr. 2018, ISSN: 1476-4687. DOI: 10.1038/nature26142. [Online]. Available: <https://www.nature.com/articles/nature26142> (visited on 11/10/2022).
- [32] S. Vaitiekėnas *et al.*, “Flux-induced topological superconductivity in full-shell nanowires,” *Science*, vol. 367, no. 6485, eaav3392, Mar. 27, 2020. DOI: 10.1126/science.aav3392. [Online]. Available: <https://www.science.org/doi/10.1126/science.aav3392> (visited on 11/10/2022).
- [33] H. H. Thorp, “Editorial Expression of Concern,” *Science*, vol. 373, no. 6554, pp. 500–500, Jul. 30, 2021. DOI: 10.1126/science.ab15286. [Online]. Available: <https://www.science.org/doi/10.1126/science.ab15286> (visited on 11/10/2022).
- [34] J. Chen *et al.*, “Ubiquitous Non-Majorana Zero-Bias Conductance Peaks in Nanowire Devices,” *Physical Review Letters*, vol. 123, no. 10, p. 107 703, Sep. 6, 2019. DOI: 10.1103/PhysRevLett.123.107703. [Online]. Available: <https://link.aps.org/doi/10.1103/PhysRevLett.123.107703> (visited on 11/06/2022).

- [35] T. Ihn, *Electronic Quantum Transport in Mesoscopic Semiconductor Structures* (Springer Tracts in Modern Physics), red. by G. Höhler *et al.* New York, NY: Springer New York, 2004, vol. 192, ISBN: 978-1-4419-2309-7 978-0-387-21828-1. DOI: 10.1007/b97630. [Online]. Available: <http://link.springer.com/10.1007/b97630> (visited on 07/08/2022).
- [36] M. Tinkham, *Introduction to Superconductivity*, 2nd ed. McGraw-Hill Book CO., 1996. DOI: 10.1063/1.2807811.
- [37] S. Iijima, “Helical microtubules of graphitic carbon,” *Nature*, vol. 354, no. 6348, pp. 56–58, 6348 Nov. 1991, ISSN: 1476-4687. DOI: 10.1038/354056a0. [Online]. Available: <https://www.nature.com/articles/354056a0> (visited on 11/03/2022).
- [38] S. Tarucha, T. Saku, Y. Tokura, and Y. Hirayama, “Sharvin resistance and its breakdown observed in long ballistic channels,” *Physical Review B*, vol. 47, no. 7, pp. 4064–4067, Feb. 15, 1993. DOI: 10.1103/PhysRevB.47.4064. [Online]. Available: <https://link.aps.org/doi/10.1103/PhysRevB.47.4064> (visited on 11/12/2022).
- [39] C. H. Jünger, “Transport spectroscopy of semiconductor superconductor nanowire hybrid devices,” Thesis, University\_of\_Basel, 2019, 1 Online-Ressource (ix, 139 Seiten). DOI: 10.5451/unibas-007214844. [Online]. Available: [http://edoc.unibas.ch/diss/DissB\\_13682](http://edoc.unibas.ch/diss/DissB_13682) (visited on 11/07/2022).
- [40] V. Ranjan, “Admittance and noise detection in mesoscopic systems via GHz impedance matching,” Thesis, University\_of\_Basel, 2017, 1 Online-Ressource (134 Seiten). DOI: 10.5451/unibas-006699807. [Online]. Available: [http://edoc.unibas.ch/diss/DissB\\_12129](http://edoc.unibas.ch/diss/DissB_12129) (visited on 11/07/2022).
- [41] J. Ridderbos, “Quantum dots and superconductivity in ge-si nanowires,” University of Twente / University of Twente, Netherlands, Feb. 28, 2018, ISBN: 978-90-365-4473-3. DOI: 10.3990/1.9789036544733.
- [42] L. P. Kouwenhoven, D. G. Austing, and S. Tarucha, “Few-electron quantum dots,” *Reports on Progress in Physics*, vol. 64, no. 6, p. 701, Jun. 2001, ISSN: 0034-4885. DOI: 10.1088/0034-4885/64/6/201. [Online]. Available: <https://dx.doi.org/10.1088/0034-4885/64/6/201> (visited on 11/07/2022).
- [43] S. Hollosy, “Locally tunable inAs nanowire quantum dots for cooper pair splitting,” Thesis, University\_of\_Basel, 2014, 1 Online-Ressource (xiii, 148 Seiten). DOI: 10.5451/unibas-006651785. [Online]. Available: [http://edoc.unibas.ch/diss/DissB\\_11899](http://edoc.unibas.ch/diss/DissB_11899) (visited on 11/07/2022).

- [44] L. A. Ponomarenko *et al.*, “Chaotic Dirac Billiard in Graphene Quantum Dots,” *Science*, vol. 320, no. 5874, pp. 356–358, Apr. 18, 2008. DOI: 10.1126/science.1154663. [Online]. Available: <https://www.science.org/doi/10.1126/science.1154663> (visited on 11/07/2022).
- [45] M. Ciorga *et al.*, “Addition spectrum of a lateral dot from Coulomb and spin-blockade spectroscopy,” *Physical Review B*, vol. 61, no. 24, R16315–R16318, Jun. 15, 2000. DOI: 10.1103/PhysRevB.61.R16315. [Online]. Available: <https://link.aps.org/doi/10.1103/PhysRevB.61.R16315> (visited on 11/07/2022).
- [46] F. Kuemmeth, S. Ilani, D. C. Ralph, and P. L. McEuen, “Coupling of spin and orbital motion of electrons in carbon nanotubes,” *Nature*, vol. 452, no. 7186, pp. 448–452, 7186 Mar. 2008, ISSN: 1476-4687. DOI: 10.1038/nature06822. [Online]. Available: <https://www.nature.com/articles/nature06822/> (visited on 11/07/2022).
- [47] F. A. Zwanenburg, C. E. W. M. van Rijmenam, Y. Fang, C. M. Lieber, and L. P. Kouwenhoven, “Spin States of the First Four Holes in a Silicon Nanowire Quantum Dot,” *Nano Letters*, vol. 9, no. 3, pp. 1071–1079, Mar. 11, 2009, ISSN: 1530-6984. DOI: 10.1021/nl803440s. [Online]. Available: <https://doi.org/10.1021/nl803440s> (visited on 11/07/2022).
- [48] T. Ihn and T. Ihn, *Semiconductor Nanostructures: Quantum States and Electronic Transport*. Oxford, New York: Oxford University Press, Dec. 3, 2009, 568 pp., ISBN: 978-0-19-953442-5.
- [49] J. Gramich, “Andreev and spin transport in carbon nanotube quantum dot hybrid devices,” Thesis, University\_of\_Basel, 2016, 1 Online-Ressource (230 Seiten). DOI: 10.5451/unibas-006623792. [Online]. Available: [http://edoc.unibas.ch/diss/DissB\\_11794](http://edoc.unibas.ch/diss/DissB_11794) (visited on 10/19/2022).
- [50] G. Fábíán, “Engineered magnetoconductance in InAs nanowire quantum dots,” Thesis, University\_of\_Basel, 2015, 1 Online-Ressource (129 Seiten). DOI: 10.5451/unibas-006514450. [Online]. Available: [http://edoc.unibas.ch/diss/DissB\\_11716](http://edoc.unibas.ch/diss/DissB_11716) (visited on 11/07/2022).
- [51] C. W. J. Beenakker, “Quantum transport in semiconductor-superconductor microjunctions,” *Physical Review B*, vol. 46, no. 19, pp. 12841–12844, Nov. 15, 1992, ISSN: 0163-1829, 1095-3795. DOI: 10.1103/PhysRevB.46.12841. [Online]. Available: <https://link.aps.org/doi/10.1103/PhysRevB.46.12841> (visited on 10/24/2022).

- [52] C. W. J. Beenakker, “Theory of Coulomb-blockade oscillations in the conductance of a quantum dot,” *Physical Review B*, vol. 44, no. 4, pp. 1646–1656, Jul. 15, 1991. DOI: 10.1103/PhysRevB.44.1646. [Online]. Available: <https://link.aps.org/doi/10.1103/PhysRevB.44.1646> (visited on 11/12/2022).
- [53] F. S. Thomas *et al.*, “Spectroscopy of the local density of states in nanowires using integrated quantum dots,” *Physical Review B*, vol. 104, no. 11, p. 115415, Sep. 15, 2021. DOI: 10.1103/PhysRevB.104.115415. [Online]. Available: <https://link.aps.org/doi/10.1103/PhysRevB.104.115415> (visited on 11/07/2022).
- [54] n. Field *et al.*, “Measurements of Coulomb blockade with a noninvasive voltage probe,” *Physical Review Letters*, vol. 70, no. 9, pp. 1311–1314, Mar. 1, 1993, ISSN: 1079-7114. DOI: 10.1103/PhysRevLett.70.1311. pmid: 10054344.
- [55] R. Schleser, E. Ruh, T. Ihn, K. Ensslin, D. C. Driscoll, and A. C. Gossard, “Time-resolved detection of individual electrons in a quantum dot,” *Applied Physics Letters*, vol. 85, no. 11, pp. 2005–2007, Sep. 13, 2004, ISSN: 0003-6951. DOI: 10.1063/1.1784875. [Online]. Available: <https://aip.scitation.org/doi/10.1063/1.1784875> (visited on 11/12/2022).
- [56] H. Kiyama *et al.*, “Single-electron charge sensing in self-assembled quantum dots,” *Scientific Reports*, vol. 8, no. 1, p. 13188, 1 Sep. 18, 2018, ISSN: 2045-2322. DOI: 10.1038/s41598-018-31268-x. [Online]. Available: <https://www.nature.com/articles/s41598-018-31268-x> (visited on 11/12/2022).
- [57] P. A. Oliveira and L. Sanz, “Bell states and entanglement dynamics on two coupled quantum molecules,” *Annals of Physics*, vol. 356, pp. 244–254, May 1, 2015, ISSN: 0003-4916. DOI: 10.1016/j.aop.2015.02.036. [Online]. Available: <https://www.sciencedirect.com/science/article/pii/S0003491615000950> (visited on 11/12/2022).
- [58] H. Ibach and H. Lüth, *Solid-State Physics: An Introduction to Principles of Materials Science ; with 100 Problems*. Springer Science & Business Media, 2003, 520 pp., ISBN: 978-3-540-43870-0. Google Books: PIEfweakKyK8C.
- [59] H. K. Onnes, “The Superconductivity of Mercury,” *Comm. Phys. Lab. Univ. Leiden*, vol. 120b, pp. 261–271, 1911.
- [60] W. Meissner and R. Ochsenfeld, “Ein neuer Effekt bei Eintritt der Supraleitfähigkeit,” *Naturwissenschaften*, vol. 21, no. 44, pp. 787–788, Nov. 1, 1933, ISSN: 1432-1904. DOI: 10.1007/BF01504252. [Online]. Available: <https://doi.org/10.1007/BF01504252> (visited on 10/19/2022).

- [61] J. Bardeen, L. N. Cooper, and J. R. Schrieffer, “Theory of Superconductivity,” *Physical Review*, vol. 108, no. 5, pp. 1175–1204, Dec. 1, 1957. DOI: 10.1103/PhysRev.108.1175. [Online]. Available: <https://link.aps.org/doi/10.1103/PhysRev.108.1175> (visited on 07/08/2022).
- [62] A. A.F., “Thermal Conductivity of the Intermediate State of Superconductors,” *JETP Letters*, vol. 28, pp. 1823–1828, 1964.
- [63] G. E. Blonder, M. Tinkham, and T. M. Klapwijk, “Transition from metallic to tunneling regimes in superconducting microconstrictions: Excess current, charge imbalance, and supercurrent conversion,” *Physical Review B*, vol. 25, no. 7, pp. 4515–4532, Apr. 1, 1982, ISSN: 0163-1829. DOI: 10.1103/PhysRevB.25.4515. [Online]. Available: <https://link.aps.org/doi/10.1103/PhysRevB.25.4515> (visited on 07/13/2022).
- [64] J.-D. Pillet, C. H. L. Quay, P. Morfin, C. Bena, A. L. Yeyati, and P. Joyez, “Andreev bound states in supercurrent-carrying carbon nanotubes revealed,” *Nature Physics*, vol. 6, no. 12, pp. 965–969, 12 Dec. 2010, ISSN: 1745-2481. DOI: 10.1038/nphys1811. [Online]. Available: <https://www.nature.com/articles/nphys1811> (visited on 11/12/2022).
- [65] C. Janvier *et al.*, “Coherent manipulation of Andreev states in superconducting atomic contacts,” *Science*, vol. 349, no. 6253, pp. 1199–1202, Sep. 11, 2015. DOI: 10.1126/science.aab2179. [Online]. Available: <https://www.science.org/doi/10.1126/science.aab2179> (visited on 11/12/2022).
- [66] A. Zazunov, V. S. Shumeiko, E. N. Bratus’, J. Lantz, and G. Wendin, “Andreev Level Qubit,” *Physical Review Letters*, vol. 90, no. 8, p. 087003, Feb. 26, 2003. DOI: 10.1103/PhysRevLett.90.087003. [Online]. Available: <https://link.aps.org/doi/10.1103/PhysRevLett.90.087003> (visited on 11/12/2022).
- [67] P. Trocha and I. Weymann, “Spin-resolved Andreev transport through double-quantum-dot Cooper pair splitters,” *Physical Review B*, vol. 91, no. 23, p. 235424, Jun. 15, 2015. DOI: 10.1103/PhysRevB.91.235424. [Online]. Available: <https://link.aps.org/doi/10.1103/PhysRevB.91.235424> (visited on 11/12/2022).
- [68] A. Martín-Rodero and A. Levy Yeyati, “Josephson and Andreev transport through quantum dots,” *Advances in Physics*, vol. 60, no. 6, pp. 899–958, Dec. 1, 2011, ISSN: 0001-8732. DOI: 10.1080/00018732.2011.624266. [Online]. Available: <https://doi.org/10.1080/00018732.2011.624266> (visited on 11/12/2022).

- [69] E. Vecino, A. Martín-Rodero, and A. L. Yeyati, “Josephson current through a correlated quantum level: Andreev states and pi junction behavior,” *Physical Review B*, vol. 68, no. 3, p. 035105, Jul. 10, 2003. DOI: 10.1103/PhysRevB.68.035105. [Online]. Available: <https://link.aps.org/doi/10.1103/PhysRevB.68.035105> (visited on 11/12/2022).
- [70] C. Janvier *et al.*, “Coherent manipulation of Andreev states in superconducting atomic contacts,” *Science*, vol. 349, no. 6253, pp. 1199–1202, Sep. 11, 2015. DOI: 10.1126/science.aab2179. [Online]. Available: <https://www.science.org/doi/10.1126/science.aab2179> (visited on 11/12/2022).
- [71] R. S. Deacon *et al.*, “Tunneling Spectroscopy of Andreev Energy Levels in a Quantum Dot Coupled to a Superconductor,” *Physical Review Letters*, vol. 104, no. 7, p. 076805, Feb. 19, 2010. DOI: 10.1103/PhysRevLett.104.076805. [Online]. Available: <https://link.aps.org/doi/10.1103/PhysRevLett.104.076805> (visited on 11/12/2022).
- [72] T. Dirks *et al.*, “Transport through Andreev bound states in a graphene quantum dot,” *Nature Physics*, vol. 7, no. 5, pp. 386–390, 5 May 2011, ISSN: 1745-2481. DOI: 10.1038/nphys1911. [Online]. Available: <https://www.nature.com/articles/nphys1911> (visited on 11/12/2022).
- [73] L. Bretheau, Ç. Ö. Girit, H. Pothier, D. Esteve, and C. Urbina, “Exciting Andreev pairs in a superconducting atomic contact,” *Nature*, vol. 499, no. 7458, pp. 312–315, 7458 Jul. 2013, ISSN: 1476-4687. DOI: 10.1038/nature12315. [Online]. Available: <https://www.nature.com/articles/nature12315> (visited on 11/12/2022).
- [74] B.-K. Kim *et al.*, “Transport Measurement of Andreev Bound States in a Kondo-Correlated Quantum Dot,” *Physical Review Letters*, vol. 110, no. 7, p. 076803, Feb. 13, 2013. DOI: 10.1103/PhysRevLett.110.076803. [Online]. Available: <https://link.aps.org/doi/10.1103/PhysRevLett.110.076803> (visited on 11/12/2022).
- [75] K. Grove-Rasmussen *et al.*, “Superconductivity-enhanced bias spectroscopy in carbon nanotube quantum dots,” *Physical Review B*, vol. 79, no. 13, p. 134518, Apr. 21, 2009. DOI: 10.1103/PhysRevB.79.134518. [Online]. Available: <https://link.aps.org/doi/10.1103/PhysRevB.79.134518> (visited on 11/12/2022).
- [76] Z. Su *et al.*, “Andreev molecules in semiconductor nanowire double quantum dots,” *Nature Communications*, vol. 8, no. 1, p. 585, 1 Sep. 19, 2017, ISSN: 2041-1723. DOI: 10.1038/s41467-017-00665-7. [Online]. Available: <https://www.nature.com/articles/s41467-017-00665-7> (visited on 10/24/2022).

- [77] C. Jünger *et al.*, “Spectroscopy of the superconducting proximity effect in nanowires using integrated quantum dots,” *Communications Physics*, vol. 2, no. 1, pp. 1–8, 1 Jul. 3, 2019, ISSN: 2399-3650. DOI: 10.1038/s42005-019-0162-4. [Online]. Available: <https://www.nature.com/articles/s42005-019-0162-4> (visited on 11/12/2022).
- [78] O. Kürtössy *et al.*, “Andreev Molecule in Parallel InAs Nanowires,” *Nano Letters*, vol. 21, no. 19, pp. 7929–7937, Oct. 13, 2021, ISSN: 1530-6984. DOI: 10.1021/acs.nanolett.1c01956. pmid: 34538054. [Online]. Available: <https://www.ncbi.nlm.nih.gov/pmc/articles/PMC8517978/> (visited on 08/26/2022).
- [79] J.-D. Pillet, P. Joyez, R. Žitko, and M. F. Goffman, “Tunneling spectroscopy of a single quantum dot coupled to a superconductor: From Kondo ridge to Andreev bound states,” *Physical Review B*, vol. 88, no. 4, p. 045101, Jul. 1, 2013. DOI: 10.1103/PhysRevB.88.045101. [Online]. Available: <https://link.aps.org/doi/10.1103/PhysRevB.88.045101> (visited on 11/12/2022).
- [80] T. Meng, S. Florens, and P. Simon, “Self-consistent description of Andreev bound states in Josephson quantum dot devices,” *Physical Review B*, vol. 79, no. 22, p. 224521, Jun. 19, 2009. DOI: 10.1103/PhysRevB.79.224521. [Online]. Available: <https://link.aps.org/doi/10.1103/PhysRevB.79.224521> (visited on 11/12/2022).
- [81] A. Braggio, M. Governale, M. G. Pala, and J. König, “Superconducting proximity effect in interacting quantum dots revealed by shot noise,” *Solid State Communications*, vol. 151, no. 2, pp. 155–158, Jan. 1, 2011, ISSN: 0038-1098. DOI: 10.1016/j.ssc.2010.10.043. [Online]. Available: <https://www.sciencedirect.com/science/article/pii/S0038109810006575> (visited on 11/12/2022).
- [82] J. O. Schindele, “Observation of cooper pair splitting and andreev bound states in carbon nanotubes,” Thesis, University\_of\_Basel, 2014, 142 S. DOI: 10.5451/unibas-006262459. [Online]. Available: [http://edoc.unibas.ch/diss/DissB\\_10805](http://edoc.unibas.ch/diss/DissB_10805) (visited on 10/19/2022).
- [83] B. D. Josephson, “Possible new effects in superconductive tunnelling,” *Physics Letters*, vol. 1, no. 7, pp. 251–253, Jul. 1, 1962, ISSN: 0031-9163. DOI: 10.1016/0031-9163(62)91369-0. [Online]. Available: <https://www.sciencedirect.com/science/article/pii/0031916362913690> (visited on 11/04/2022).
- [84] K. K. Likharev, “Superconducting weak links,” *Reviews of Modern Physics*, vol. 51, no. 1, pp. 101–159, Jan. 1, 1979. DOI: 10.1103/RevModPhys.51.101. [Online]. Available: <https://link.aps.org/doi/10.1103/RevModPhys.51.101> (visited on 11/04/2022).

- [85] V. Ambegaokar and A. Baratoff, “Tunneling Between Superconductors,” *Physical Review Letters*, vol. 10, no. 11, pp. 486–489, Jun. 1, 1963. DOI: 10.1103/PhysRevLett.10.486. [Online]. Available: <https://link.aps.org/doi/10.1103/PhysRevLett.10.486> (visited on 11/04/2022).
- [86] I. O. Kulik and A. N. Omel’yanchuk, “Contribution to the microscopic theory of the Josephson effect in superconducting bridges,” *JETP Lett. (USSR) (Engl. Transl.)*, v. 21, no. 4, pp. 96–97, Feb. 20, 1975. [Online]. Available: <https://www.osti.gov/biblio/4209268> (visited on 11/04/2022).
- [87] C. Li, S. Guéron, A. Chepelianskii, and H. Bouchiat, “Full range of proximity effect probed with superconductor/graphene/superconductor junctions,” *Physical Review B*, vol. 94, no. 11, p. 115405, Sep. 2, 2016, ISSN: 2469-9950, 2469-9969. DOI: 10.1103/PhysRevB.94.115405. [Online]. Available: <https://link.aps.org/doi/10.1103/PhysRevB.94.115405> (visited on 11/04/2022).
- [88] P. Dubos, H. Courtois, B. Pannetier, F. K. Wilhelm, A. D. Zaikin, and G. Schön, “Josephson critical current in a long mesoscopic S-N-S junction,” *Physical Review B*, vol. 63, no. 6, p. 064502, Jan. 18, 2001. DOI: 10.1103/PhysRevB.63.064502. [Online]. Available: <https://link.aps.org/doi/10.1103/PhysRevB.63.064502> (visited on 11/04/2022).
- [89] D. Averin and A. Bardas, “Ac Josephson Effect in a Single Quantum Channel,” *Physical Review Letters*, vol. 75, no. 9, pp. 1831–1834, Aug. 28, 1995, ISSN: 0031-9007, 1079-7114. DOI: 10.1103/PhysRevLett.75.1831. [Online]. Available: <https://link.aps.org/doi/10.1103/PhysRevLett.75.1831> (visited on 11/06/2022).
- [90] B. Ludoph *et al.*, “Multiple Andreev reflection in single-atom niobium junctions,” *Physical Review B*, vol. 61, no. 12, pp. 8561–8569, Mar. 15, 2000, ISSN: 0163-1829, 1095-3795. DOI: 10.1103/PhysRevB.61.8561. [Online]. Available: <https://link.aps.org/doi/10.1103/PhysRevB.61.8561> (visited on 11/09/2022).
- [91] A. Levy Yeyati, J. C. Cuevas, and A. Martín-Rodero, “Dynamical Coulomb Blockade of Multiple Andreev Reflections,” *Physical Review Letters*, vol. 95, no. 5, p. 056804, Jul. 28, 2005, ISSN: 0031-9007, 1079-7114. DOI: 10.1103/PhysRevLett.95.056804. [Online]. Available: <https://link.aps.org/doi/10.1103/PhysRevLett.95.056804> (visited on 11/09/2022).

- [92] M. Kjaergaard *et al.*, “Transparent Semiconductor-Superconductor Interface and Induced Gap in an Epitaxial Heterostructure Josephson Junction,” *Physical Review Applied*, vol. 7, no. 3, p. 034029, Mar. 28, 2017, ISSN: 2331-7019. DOI: 10.1103/PhysRevApplied.7.034029. [Online]. Available: <http://link.aps.org/doi/10.1103/PhysRevApplied.7.034029> (visited on 10/23/2022).
- [93] X. Duan and C. M. Lieber, “General Synthesis of Compound Semiconductor Nanowires,” *Advanced Materials*, vol. 12, no. 4, pp. 298–302, 2000, ISSN: 1521-4095. DOI: 10.1002/(SICI)1521-4095(200002)12:4<298::AID-ADMA298>3.0.CO;2-Y. [Online]. Available: <https://onlinelibrary.wiley.com/doi/abs/10.1002/%28SICI%291521-4095%28200002%2912%3A4%3C298%3A%3AAID-ADMA298%3E3.0.CO%3B2-Y> (visited on 07/13/2022).
- [94] A. M. Burke *et al.*, “InAs Nanowire Transistors with Multiple, Independent Wrap-Gate Segments,” *Nano Letters*, vol. 15, no. 5, pp. 2836–2843, May 13, 2015, ISSN: 1530-6984. DOI: 10.1021/nl5043243. [Online]. Available: <https://doi.org/10.1021/nl5043243> (visited on 11/11/2022).
- [95] R. S. Wagner and W. C. Ellis, “Vapor-liquid-solid mechanism of single crystal growth,” *Applied Physics Letters*, vol. 4, no. 5, pp. 89–90, Mar. 1964, ISSN: 0003-6951. DOI: 10.1063/1.1753975. [Online]. Available: <https://aip.scitation.org/doi/10.1063/1.1753975> (visited on 11/11/2022).
- [96] C. Thelander, P. Caroff, S. Plissard, A. W. Dey, and K. A. Dick, “Effects of Crystal Phase Mixing on the Electrical Properties of InAs Nanowires,” *Nano Letters*, vol. 11, no. 6, pp. 2424–2429, Jun. 8, 2011, ISSN: 1530-6984. DOI: 10.1021/nl2008339. [Online]. Available: <https://doi.org/10.1021/nl2008339> (visited on 11/11/2022).
- [97] K. A. Dick, C. Thelander, L. Samuelson, and P. Caroff, “Crystal Phase Engineering in Single InAs Nanowires,” *Nano Letters*, vol. 10, no. 9, pp. 3494–3499, Sep. 8, 2010, ISSN: 1530-6984. DOI: 10.1021/nl101632a. [Online]. Available: <https://doi.org/10.1021/nl101632a> (visited on 11/11/2022).
- [98] S. Lehmann, J. Wallentin, D. Jacobsson, K. Deppert, and K. A. Dick, “A General Approach for Sharp Crystal Phase Switching in InAs, GaAs, InP, and GaP Nanowires Using Only Group V Flow,” *Nano Letters*, vol. 13, no. 9, pp. 4099–4105, Sep. 11, 2013, ISSN: 1530-6984. DOI: 10.1021/nl401554w. [Online]. Available: <https://doi.org/10.1021/nl401554w> (visited on 11/11/2022).

- [99] M. Nilsson, L. Namazi, S. Lehmann, M. Leijnse, K. A. Dick, and C. Thelander, “Single-electron transport in InAs nanowire quantum dots formed by crystal phase engineering,” *Physical Review B*, vol. 93, no. 19, p. 195422, May 17, 2016. DOI: 10.1103/PhysRevB.93.195422. [Online]. Available: <https://link.aps.org/doi/10.1103/PhysRevB.93.195422> (visited on 11/11/2022).
- [100] L. Romeo, S. Roddaro, A. Pitanti, D. Ercolani, L. Sorba, and F. Beltram, “Electrostatic Spin Control in InAs/InP Nanowire Quantum Dots,” *Nano Letters*, vol. 12, no. 9, pp. 4490–4494, Sep. 12, 2012, ISSN: 1530-6984. DOI: 10.1021/nl301497j. [Online]. Available: <https://doi.org/10.1021/nl301497j> (visited on 11/11/2022).
- [101] P. Krogstrup *et al.*, “Epitaxy of semiconductor-superconductor nanowires,” *Nature Materials*, vol. 14, no. 4, pp. 400–406, Apr. 2015, ISSN: 1476-1122. DOI: 10.1038/nmat4176. pmid: 25581626.
- [102] S. Gazibegovic *et al.*, “Epitaxy of advanced nanowire quantum devices,” *Nature*, vol. 548, no. 7668, pp. 434–438, Aug. 23, 2017, ISSN: 1476-4687. DOI: 10.1038/nature23468. pmid: 28836603.
- [103] S. Baba *et al.*, “Superconducting transport in single and parallel double InAs quantum dot Josephson junctions with Nb-based superconducting electrodes,” *Applied Physics Letters*, vol. 107, no. 22, p. 222602, Nov. 30, 2015, ISSN: 0003-6951. DOI: 10.1063/1.4936888. [Online]. Available: <https://aip.scitation.org/doi/full/10.1063/1.4936888> (visited on 11/11/2022).
- [104] S. Baba *et al.*, “Cooper-pair splitting in two parallel InAs nanowires,” *New Journal of Physics*, vol. 20, no. 6, p. 063021, Jun. 15, 2018, ISSN: 1367-2630. DOI: 10.1088/1367-2630/aac74e. [Online]. Available: <https://iopscience.iop.org/article/10.1088/1367-2630/aac74e> (visited on 10/19/2022).
- [105] T. Kanne *et al.*, “Double Nanowires for Hybrid Quantum Devices,” *Advanced Functional Materials*, vol. 32, no. 9, p. 2107926, 2022, ISSN: 1616-3028. DOI: 10.1002/adfm.202107926. [Online]. Available: <https://onlinelibrary.wiley.com/doi/abs/10.1002/adfm.202107926> (visited on 07/08/2022).
- [106] A. E. Hansen, M. T. Björk, C. Fasth, C. Thelander, and L. Samuelson, “Spin relaxation in InAs nanowires studied by tunable weak antilocalization,” *Physical Review B*, vol. 71, no. 20, p. 205328, May 31, 2005. DOI: 10.1103/PhysRevB.71.205328. [Online]. Available: <https://link.aps.org/doi/10.1103/PhysRevB.71.205328> (visited on 11/12/2022).

- [107] L. Ö. Olsson, C. B. M. Andersson, M. C. Håkansson, J. Kanski, L. Ilver, and U. O. Karlsson, “Charge Accumulation at InAs Surfaces,” *Physical Review Letters*, vol. 76, no. 19, pp. 3626–3629, May 6, 1996. DOI: 10.1103/PhysRevLett.76.3626. [Online]. Available: <https://link.aps.org/doi/10.1103/PhysRevLett.76.3626> (visited on 11/12/2022).
- [108] J. Gooth *et al.*, “Ballistic One-Dimensional InAs Nanowire Cross-Junction Interconnects,” *Nano Letters*, vol. 17, no. 4, pp. 2596–2602, Apr. 12, 2017, ISSN: 1530-6984. DOI: 10.1021/acs.nanolett.7b00400. [Online]. Available: <https://doi.org/10.1021/acs.nanolett.7b00400> (visited on 11/12/2022).
- [109] A. C. Ford, S. B. Kumar, R. Kapadia, J. Guo, and A. Javey, “Observation of Degenerate One-Dimensional Sub-Bands in Cylindrical InAs Nanowires,” *Nano Letters*, vol. 12, no. 3, pp. 1340–1343, Mar. 14, 2012, ISSN: 1530-6984. DOI: 10.1021/nl203895x. [Online]. Available: <https://doi.org/10.1021/nl203895x> (visited on 11/12/2022).
- [110] S. Chuang, Q. Gao, R. Kapadia, A. C. Ford, J. Guo, and A. Javey, “Ballistic InAs Nanowire Transistors,” *Nano Letters*, vol. 13, no. 2, pp. 555–558, Feb. 13, 2013, ISSN: 1530-6984. DOI: 10.1021/nl3040674. [Online]. Available: <https://doi.org/10.1021/nl3040674> (visited on 11/12/2022).
- [111] M. Scheffler, S. Nadj-Perge, L. P. Kouwenhoven, M. T. Borgström, and E. P. A. M. Bakkers, “Diameter-dependent conductance of InAs nanowires,” *Journal of Applied Physics*, vol. 106, no. 12, p. 124303, Dec. 15, 2009, ISSN: 0021-8979. DOI: 10.1063/1.3270259. [Online]. Available: <https://aip.scitation.org/doi/10.1063/1.3270259> (visited on 11/12/2022).
- [112] J. Gooth *et al.*, “Ballistic one-dimensional transport in InAs nanowires monolithically integrated on silicon,” *Applied Physics Letters*, vol. 110, no. 8, p. 083105, Feb. 20, 2017, ISSN: 0003-6951, 1077-3118. DOI: 10.1063/1.4977031. [Online]. Available: <http://aip.scitation.org/doi/10.1063/1.4977031> (visited on 10/16/2022).
- [113] J. C. Estrada Saldaña *et al.*, “Split-Channel Ballistic Transport in an InSb Nanowire,” *Nano Letters*, vol. 18, no. 4, pp. 2282–2287, Apr. 11, 2018, ISSN: 1530-6984, 1530-6992. DOI: 10.1021/acs.nanolett.7b03854. [Online]. Available: <https://pubs.acs.org/doi/10.1021/acs.nanolett.7b03854> (visited on 10/16/2022).
- [114] G. C. Ménard *et al.*, “Suppressing quasiparticle poisoning with a voltage-controlled filter,” *Physical Review B*, vol. 100, no. 16, p. 165307, Oct. 29, 2019, ISSN: 2469-9950, 2469-9969. DOI: 10.1103/PhysRevB.100.165307. [Online]. Available: <https://link.aps.org/doi/10.1103/PhysRevB.100.165307> (visited on 11/03/2022).

- [115] D. Rainis and D. Loss, “Majorana qubit decoherence by quasiparticle poisoning,” *Physical Review B*, vol. 85, no. 17, p. 174533, May 30, 2012, ISSN: 1098-0121, 1550-235X. DOI: 10.1103/PhysRevB.85.174533. [Online]. Available: <https://link.aps.org/doi/10.1103/PhysRevB.85.174533> (visited on 11/03/2022).
- [116] S. J. Pilkington and M. Missous, “The growth of epitaxial aluminium on As containing compound semiconductors,” *Journal of Crystal Growth*, vol. 196, no. 1, pp. 1–12, Jan. 1, 1999, ISSN: 0022-0248. DOI: 10.1016/S0022-0248(98)00784-2. [Online]. Available: <https://www.sciencedirect.com/science/article/pii/S0022024898007842> (visited on 11/08/2022).
- [117] J. E. Sestoft *et al.*, “Engineering hybrid epitaxial InAsSb/Al nanowires for stronger topological protection,” *Physical Review Materials*, vol. 2, no. 4, p. 044202, Apr. 12, 2018. DOI: 10.1103/PhysRevMaterials.2.044202. [Online]. Available: <https://link.aps.org/doi/10.1103/PhysRevMaterials.2.044202> (visited on 07/28/2022).
- [118] W. Chang *et al.*, “Hard gap in epitaxial semiconductor–superconductor nanowires,” *Nature Nanotechnology*, vol. 10, no. 3, pp. 232–236, Mar. 2015, ISSN: 1748-3387, 1748-3395. DOI: 10.1038/nnano.2014.306. [Online]. Available: <http://www.nature.com/articles/nnano.2014.306> (visited on 07/13/2022).
- [119] Ö. Gül *et al.*, “Hard Superconducting Gap in InSb Nanowires,” *Nano Letters*, vol. 17, no. 4, pp. 2690–2696, Apr. 12, 2017, ISSN: 1530-6984, 1530-6992. DOI: 10.1021/acs.nanolett.7b00540. [Online]. Available: <https://pubs.acs.org/doi/10.1021/acs.nanolett.7b00540> (visited on 10/16/2022).
- [120] J. L. Webb *et al.*, “Electrical and Surface Properties of InAs/InSb Nanowires Cleaned by Atomic Hydrogen,” *Nano Letters*, vol. 15, no. 8, pp. 4865–4875, Aug. 12, 2015, ISSN: 1530-6984, 1530-6992. DOI: 10.1021/acs.nanolett.5b00282. [Online]. Available: <https://pubs.acs.org/doi/10.1021/acs.nanolett.5b00282> (visited on 10/19/2022).
- [121] Z. Scherübl, A. Pályi, and S. Csonka, “Transport signatures of an Andreev molecule in a quantum dot–superconductor–quantum dot setup,” *Beilstein Journal of Nanotechnology*, vol. 10, pp. 363–378, Feb. 6, 2019, ISSN: 2190-4286. DOI: 10.3762/bjnano.10.36. [Online]. Available: <https://www.beilstein-journals.org/bjnano/articles/10/36> (visited on 10/24/2022).
- [122] S. Matsuo *et al.*, “Observation of nonlocal Josephson effect on double InAs nanowires,” *Communications Physics*, vol. 5, no. 1, pp. 1–6, 1 Sep. 13, 2022, ISSN: 2399-3650. DOI: 10.1038/s42005-022-00994-0. [Online]. Available: <https://www.nature.com/articles/s42005-022-00994-0> (visited on 09/29/2022).

- [123] O. Kürtössy *et al.*, “Parallel InAs nanowires for Cooper pair splitters with Coulomb repulsion,” *npj Quantum Materials*, vol. 7, no. 1, pp. 1–6, 1 Sep. 9, 2022, ISSN: 2397-4648. DOI: 10.1038/s41535-022-00497-9. [Online]. Available: <https://www.nature.com/articles/s41535-022-00497-9> (visited on 11/11/2022).
- [124] P. Perla *et al.*, “Fully *in situ* Nb/InAs-nanowire Josephson junctions by selective-area growth and shadow evaporation,” *Nanoscale Advances*, vol. 3, no. 5, pp. 1413–1421, 2021, ISSN: 2516-0230. DOI: 10.1039/D0NA00999G. [Online]. Available: <http://xlink.rsc.org/?DOI=D0NA00999G> (visited on 10/30/2022).
- [125] H. Y. Günel *et al.*, “Supercurrent in Nb/InAs-nanowire/Nb Josephson junctions,” *Journal of Applied Physics*, vol. 112, no. 3, p. 034316, Aug. 2012, ISSN: 0021-8979. DOI: 10.1063/1.4745024. [Online]. Available: <https://aip.scitation.org/doi/full/10.1063/1.4745024> (visited on 10/30/2022).
- [126] K. Ueda *et al.*, “Dominant nonlocal superconducting proximity effect due to electron-electron interaction in a ballistic double nanowire,” *Science Advances*, vol. 5, no. 10, eaaw2194, Oct. 4, 2019. DOI: 10.1126/sciadv.aaw2194. [Online]. Available: <https://www.science.org/doi/10.1126/sciadv.aaw2194> (visited on 10/25/2022).
- [127] L. B. Wang *et al.*, “Phase-coherent transport and spin relaxation in InAs nanowires grown by molecule beam epitaxy,” *Applied Physics Letters*, vol. 106, no. 17, p. 173105, Apr. 27, 2015, ISSN: 0003-6951, 1077-3118. DOI: 10.1063/1.4919390. [Online]. Available: <http://aip.scitation.org/doi/10.1063/1.4919390> (visited on 10/25/2022).
- [128] F. Haas *et al.*, “Anisotropic phase coherence in GaAs/InAs core/shell nanowires,” *Nanotechnology*, vol. 28, no. 44, p. 445202, Oct. 2017, ISSN: 0957-4484. DOI: 10.1088/1361-6528/aa887d. [Online]. Available: <https://dx.doi.org/10.1088/1361-6528/aa887d> (visited on 10/25/2022).
- [129] S. Takei, B. M. Fregoso, H.-Y. Hui, A. M. Lobos, and S. Das Sarma, “Soft Superconducting Gap in Semiconductor Majorana Nanowires,” *Physical Review Letters*, vol. 110, no. 18, p. 186803, Apr. 30, 2013, ISSN: 0031-9007, 1079-7114. DOI: 10.1103/PhysRevLett.110.186803. [Online]. Available: <https://link.aps.org/doi/10.1103/PhysRevLett.110.186803> (visited on 10/26/2022).
- [130] G. Catelani, J. Koch, L. Frunzio, R. J. Schoelkopf, M. H. Devoret, and L. I. Glazman, “Quasiparticle relaxation of superconducting qubits in the presence of flux,” *Physical Review Letters*, vol. 106, no. 7, Feb. 16, 2011, ISSN: 0031-9007. DOI: 10.1103/PhysRevLett.106.077002. [On-

- line]. Available: <http://www.scopus.com/inward/record.url?scp=79951633269&partnerID=8YFLogxK> (visited on 11/04/2022).
- [131] H. Paik *et al.*, “Observation of High Coherence in Josephson Junction Qubits Measured in a Three-Dimensional Circuit QED Architecture,” *Physical Review Letters*, vol. 107, no. 24, p. 240 501, Dec. 5, 2011. DOI: 10.1103/PhysRevLett.107.240501. [Online]. Available: <https://link.aps.org/doi/10.1103/PhysRevLett.107.240501> (visited on 11/04/2022).
- [132] L. J. Geerligs *et al.*, “Single Cooper pair pump,” *Zeitschrift für Physik B Condensed Matter*, vol. 85, no. 3, pp. 349–355, Oct. 1, 1991, ISSN: 1431-584X. DOI: 10.1007/BF01307630. [Online]. Available: <https://doi.org/10.1007/BF01307630> (visited on 11/04/2022).
- [133] J. Tiira *et al.*, “Magnetically-driven colossal supercurrent enhancement in InAs nanowire Josephson junctions,” *Nature Communications*, vol. 8, no. 1, p. 14984, 1 Apr. 12, 2017, ISSN: 2041-1723. DOI: 10.1038/ncomms14984. [Online]. Available: <https://www.nature.com/articles/ncomms14984> (visited on 09/09/2022).
- [134] Y. Sato *et al.*, “Quasiparticle Trapping at Vortices Producing Josephson Supercurrent Enhancement,” *Physical Review Letters*, vol. 128, no. 20, p. 207 001, May 19, 2022. DOI: 10.1103/PhysRevLett.128.207001. [Online]. Available: <https://link.aps.org/doi/10.1103/PhysRevLett.128.207001> (visited on 10/26/2022).
- [135] M. Taupin, I. M. Khaymovich, M. Meschke, A. S. Mel’nikov, and J. P. Pekola, “Tunable quasiparticle trapping in Meissner and vortex states of mesoscopic superconductors,” *Nature Communications*, vol. 7, no. 1, p. 10 977, 1 Mar. 16, 2016, ISSN: 2041-1723. DOI: 10.1038/ncomms10977. [Online]. Available: <https://www.nature.com/articles/ncomms10977> (visited on 10/31/2022).
- [136] G. Stan, S. B. Field, and J. M. Martinis, “Critical Field for Complete Vortex Expulsion from Narrow Superconducting Strips,” *Physical Review Letters*, vol. 92, no. 9, p. 097 003, Mar. 5, 2004. DOI: 10.1103/PhysRevLett.92.097003. [Online]. Available: <https://link.aps.org/doi/10.1103/PhysRevLett.92.097003> (visited on 11/04/2022).
- [137] A. A. Abrikosov, “Magnetic properties of superconductors of the second group,” *Sov. Phys. - JETP (Engl. Transl.); (United States)*, vol. 5:6, Jan. 1, 1957. [Online]. Available: <https://www.osti.gov/biblio/7155233> (visited on 11/04/2022).

- [138] J. T. Peltonen, J. T. Muhonen, M. Meschke, N. B. Kopnin, and J. P. Pekola, “Magnetic-field-induced stabilization of nonequilibrium superconductivity in a normal-metal/insulator/superconductor junction,” *Physical Review B*, vol. 84, no. 22, p. 220 502, Dec. 14, 2011. DOI: 10.1103/PhysRevB.84.220502. [Online]. Available: <https://link.aps.org/doi/10.1103/PhysRevB.84.220502> (visited on 10/31/2022).
- [139] J. Aumentado, M. W. Keller, J. M. Martinis, and M. H. Devoret, “Nonequilibrium Quasiparticles and  $2e$  Periodicity in Single-Cooper-Pair Transistors,” *Physical Review Letters*, vol. 92, no. 6, p. 066 802, Feb. 13, 2004, ISSN: 0031-9007, 1079-7114. DOI: 10.1103/PhysRevLett.92.066802. [Online]. Available: <https://link.aps.org/doi/10.1103/PhysRevLett.92.066802> (visited on 11/05/2022).
- [140] N. A. Court, A. J. Ferguson, and R. G. Clark, “Energy gap measurement of nanostructured thin aluminium films for use in single Cooper-pair devices,” *Superconductor Science and Technology*, vol. 21, no. 1, p. 015 013, Jan. 1, 2008, ISSN: 0953-2048, 1361-6668. DOI: 10.1088/0953-2048/21/01/015013. arXiv: 0706.4150 [cond-mat]. [Online]. Available: <http://arxiv.org/abs/0706.4150> (visited on 11/05/2022).
- [141] L. Landau, “The Intermediate State of Supraconductors,” *Nature*, vol. 141, no. 3572, pp. 688–688, 3572 Apr. 1938, ISSN: 1476-4687. DOI: 10.1038/141688a0. [Online]. Available: <https://www.nature.com/articles/141688a0> (visited on 11/13/2022).

# Curriculum Vitae

Olivier Faist

Born on the 5<sup>th</sup> of May 1991 in Lausanne (Switzerland)

## Education

8/2018–now

**PhD in experimental physics at the University of Basel**

- Dissertation in the group of Prof. Dr. C. Schönenberger  
*“Andreev bound states in semiconducting double nanowires”*

2015–2018

**Masters of Science in Physics** at the ETH Zürich

- Master thesis in the group of Prof. Dr. Atac Imomoglu (ETH Zürich)  
*“Photon statistics of a Gaussian squeezed state in exciton-polariton microcavities”*
- Project work in the group of Prof. Dr. Lukas Novotny (ETH Zürich)  
*“Building a high-finesse cavity”*
- Project work in the group of Prof. Dr. Lukas Emmenegger (EMPA Dübendorf)  
*“Design of a fast data acquisition system using field-programmable gate arrays”*

2009–2014

**Bachelors of Science in Physics** at ETH Zürich

2009

**Maturité fédérale** Lycée Denis-de-Rougemont, Neuchâtel

- Travail de maturité  
*“Conception et réalisation d’un télémètre à ultrasons”*

## Positions

8/2018–now

*Teaching assistant for physics at the University of Basel*



## Acknowledgements

Looking back on five years of PhD, I will remember with nostalgia on a great time. What made this experience great comes mostly down to the people involved, without whom this thesis would no even have been possible.

First, I owe an immense debt of gratitude to Prof. Dr. Christian Schöenberger, who not only gave me the opportunity to join his group and do the research project summarized in this thesis, but was also always available for meetings, always sharing his insights into my results, motivating me by assuring there was interesting stuff there, being extraordinarily patient with me when my activity reports were late, and always taking great care of us as a group - organizing yearly summer *and* winter retreats, crystallizing the group social cohesion.

Second, I would like to thank Dr. Kasper Grove-Rasmussen and Dr. Szabolcs Csonka, for taking the time to read my manuscript. I could not have wished for more adequate experts, both having worked on similar projects to mine. I am looking forward to a nice discussion.

Third, I would like to thank Andreas Baumgartner, who supervised me in my research, and was always available for meetings.

I feel blessed to have been part of such a great group, and although being in the office doubling as an inofficial coffee break room sometimes slightly impacted productivity, the energy and motivation given by discussions - be it about physics, politics, history, philosophy or any subject - more than compensated the time invested. All those good times were shared with colleagues, some of which became really good friends, with whom I hope the friendship will last well beyond my time in this group. In no particular order, I would like to thank: Ian Sampaio, whose empathy helped me overcome the frustrating times which come naturally with any research project. Carlo Ciaccia, who not only introduced me to Italian music but made sure the coffee machine - our most critical piece of equipment - was always fine-tuned and producing the best coffee north of the Alps, and whose Italian cooking made for great evenings. Martin Endres, who patiently tolerated my bumbling riding along on bike tours. I would like to thank the whole physics department cycling team: Martin Endres, Matthys Hermanns, Hinrich Mattiat, Giulio Romagnoli, Carlo Ciaccia amongst others, the evening rides were a perfect way to refresh the mind after a day of work. Mehdi Ramezani, who always had motivating words

and a positive spirit in the numerous coffee breaks we shared. Artem Kononov, whose dry humour and great physical knowledge - and 0-tolerance policy for... statements unsupported by undeniable evidence, the usage of the exact word not being adequate for a printed publication - was a great help, as well as always promptly and expertly helping me with any cryostat issues. Paritosh Karnatak, who was always ready to lend a helping hand with my cryostat as well, and excellent Indium-seal making talent made sure the IVC never leaked an atom of  $^3\text{He}$ . Frederick Thomas, whose dry humour made the time spent in our common office quite enjoyable. Christian Jünger and Arunav Bordoloi, who taught me the art of fabrication. Alessia Pally, with whom I had a great time sharing the office, and who is always ready to help. Simon Zihlman and David Indolese, with whom I shared the commitment to a weekly group meeting in the bar. From the theory group, Denis Chevallier and Ferdinand, who made sure the collaboration between experiment and theory was extended to social gatherings and BBQs. Roy Haller, who was always ready to help, although not involved in my research project, and whose kind words of encouragement in times of frustration were of great help. Luk-Yi Cheung, whose pearls of wisdom punctuated the group life. Lujun Wang, Deepankar Sarmah, Blesson Varghese, Zarina Mingazheva, Jann Ungerer, with whom we had fun organizing a nice conference in Flumsberg, Gulibustan Abulizi, and recently Rhounak Jha, whose positive attitude is second to none, and Master students Tom Jenniskens, Giorgio Fabris, who led me to the best *prosciutteria* in Milan, and Sangwan Nikun.

I am also immensely grateful to my friends, who played no small part in helping to deal with the stresses and frustrations of the research life. I would also like to thank my brother, Philippe, and sister, Daphné, who took the time to help root out spelling mistakes from this thesis. My parents, who not only are always supportive of my activities, my path in life, and the pace at which I walk it, but also helped with the proof reading of this thesis.

Finally, I am eternally grateful to Valentina, who helped me carry the load of the final phase of my phd, providing me with stability and unwavering support. Although in the final push of this project, the going did occasionally get a bit strenuous, having you at my side made it not only bearable, but actually quite enjoyable.

Thank you